



Large Eddy Simulation of Coastal Structures-Induced Large Scale Coherent Eddy and Sediment Transport

Thesis submitted in accordance with the requirements of
the University of Liverpool for the degree of Master of
Philosophy

by

GUGUM GUMBIRA

December 2019

Abstract

The existence of structures, such as groynes, breakwaters and dykes as the coastal protection system can produce continuous disturbance in the vertical shear flow. As a consequence, large-predominantly 2D coherent structures are introduced to the main flow. The structures, that can grow due to energy transfer from shear stress and dissipate due to bottom friction, have lateral dimension larger than water depth. One of the primary objectives in this study is to take into account of these structures in the numerical models. To resolve the large-scale, high containing energy and modelled the small eddies, Large Eddy Simulation that moves beyond spatial filtering procedure rather than time averaging is adopted in this study. By using this approach, the existence of coherent eddy induced by coastal structures can be preserved in the numerical modelling. To overcome the anisotropy issue caused by the mesh size differences between horizontal and vertical layers, Anisotropy Smagorinsky Model (ASM) is used as the SGS closure system.

The applied model is tested to simulate an obstacle induced coherent structures such as flow over a cylinder, flow over single and series of groyne. The simulations cover various dimensions from laboratory-scale experiments to real-scale example. Large scale coherent structure components are studied to review the characteristic and temporal evolution in the main flow dynamics.

The flow over the cylinder case is a common test in the turbulent flow study due to its simple geometry, but offers complex flow structures. The model has similar condition with Roulund et al. [1] rough case experiment with 50 m long and 4 m wide. Model validation shows well result when compared with the experimental data from Roulund et al. [1] for both stream-wise and vertical velocities except at the downstream part, which model under-predicted the velocity magnitude. Overall, the complex structures such as horseshoe vortex at the upstream side of the cylinder, flow separation and lee-wake vortices are properly resolved by the adopted model.

The second test, flow over single groyne is conducted to evaluate model implementation in typical real-field case and to provide a deep understanding of the flow physics and dynamics of the large coherent structures. The domain covers about 300 m long and 60 m wide open channel with 5 m constant water depth. Model results describe the generation of

vortex tubes near the tip of groyne caused velocity amplification. This process is captured by using 1 m mesh size while coarser mesh with size 2.5 and 5 m, do not resolve these structures. Important finding in this case is that the existence of new emerge vortex tubes significantly alter the orientation of detached eddy. The later structure interacts with the side wall to form the main circulation in the recirculation region. The primary eddy has an oblique shape in which it is sharper near the bed and grows gradually as reach the surface layer. Spectrum analysis explains the role of vortical structure interaction resulted high turbulent energy level. The result is confirmed by analysing the TKE close to the groyne tip and inside the recirculation area. Pairs of low and high TKE are found around the core of vortical structures. The HV structures reproduced by the model have similar dimension with the experiment. The interaction with the WAV at the bottom layer provides additional momentum in the horizontal direction.

The third test is applied to study the sediment exchange process between the main channel and the groyne field. The developed model is then coupled with the FVCOM sediment module. The domain is made with the same configuration as a physical model of Yossef and de Vriend [2] for the emerge groyne condition. The transverse roll-up of the incoming flow at the upstream side of first groyne forms a primary necklace and elongated vortex. It is identified as the formation of complex HV that induce large aperiodic oscillation at the bottom corner of groyne. An important finding from this study confirms that the HV system is not single structure but formed by multiple-like necklace vortexes. The existence of primary, secondary and dynamic eddies and their interaction were captured inside the groyne field. The velocity magnitude of the primary eddy that occupies more than two third of the space is agree with the theoretical finding. Sediment simulation shows that particles are imported from the main channel following the primary circulation pattern. It entrances the embayment through main eddy at the downstream part of the groyne. Suspended sediment distributions are strongly affected by large coherent structures. Mean value analysis showed that the formation of high deposited region closely related to the primary eddy inside the embayments. Temporal development of morphology presents an erosion area close to the tip of groyne.

Contents

Abstract	i
Contents	iii
List of Figures	vi
List of Tables	ix
Nomenclature	x
Acknowledgement	xiv
1 Introduction	1
1.1 Research background	1
1.2 Research questions	4
1.3 Research Outline	4
2 Coastal Processes and Numerical Modelling	6
2.1 Turbulence modelling	6
2.2 Method of investigation	6
2.3 Basic Nearshore processes	8
2.3.1 Nearshore Circulation	8
2.3.2 Coastal Sediment Transport	9
2.4 Coastal Models	10
2.4.1 Wave Models	11
2.4.2 Circulation Models	11
2.4.3 Sediment Transport Models	12
2.5 Turbulence in coastal processes and LES modelling	13
2.5.1 Generation of the large scale coherent structure	14
2.5.2 Vortex identification	16
2.5.3 Predicting Turbulent Flows	16

2.6	Summary	19
3	Numerical Model	21
3.1	System of existing model: Zheng et al. [18] model	21
3.1.1	Introduction	21
3.1.2	Circulation Model	22
3.1.3	Sediment Transport Module	23
3.1.4	Bottom Boundary Layer Model	26
3.2	New LES Concept	27
3.2.1	LES filtered governing equations	27
3.2.2	Subgrid viscosity	29
3.3	Numerical schemes	33
3.3.1	Numerical algorithm	33
3.4	Summary	34
4	Model validation	36
4.1	Flow pass a cylinder	36
4.2	Roulund experiment	38
4.3	Model domain	38
4.3.1	Model boundary	39
4.3.2	Computational mesh	39
4.3.3	Numerical parameter	40
4.4	Model results	41
4.4.1	Flow structures	41
4.5	Summary	48
5	Flow over single groyne	49
5.1	Introduction	49
5.2	Numerical simulation	50
5.3	Result and discussion	52
5.3.1	Mesh sensitivity	52
5.3.2	The vortical structures interaction	54
5.3.3	The shear layer and recirculation region eddies	57
5.3.4	The transfers of turbulence energy	59
5.3.5	The vortical structures roles in the mean flow	61
5.3.6	The HV system	63
5.4	Summary	66

6	Flow over a series of groyne	68
6.1	Introduction	68
6.2	Numerical Simulation	68
6.3	Result and discussions	70
6.3.1	Mean flow data analysis	70
6.3.2	The HV system	73
6.3.3	The role of large coherent structures in groyne field	74
6.3.4	Turbulent energy	76
6.3.5	Sediment Transport	78
6.4	Summary	83
7	Conclusions and recommendations for future research	85
7.1	Conclusions	85
7.2	Suggestion for future research	87
	Bibliography	88

List of Figures

1.1	Vortex street wake at island with diameter 160 m. Figure is obtained from Ingram and Chu [5].	2
2.1	Turbulent energy spectrum (Galea [66]).	17
3.1	Illustration of σ -coordinate system in the model. Figure is reproduced from Morales Marín [71].	22
3.2	Optimal value variation for C_h and C_v (Petronio et al. [99])	32
3.3	The flowchart of ASM-LES in the model.	34
4.1	Representation of flow regimes around circular cylinder (Sumer et al. [59, p. 2])	37
4.2	Model domain (a) three-dimension and (b) two-dimension.	39
4.3	Triangular meshes around cylinder.	40
4.4	The mean streamwise velocity for eight depths from the model (solid line) and Roulund et al. [1] experiment (circle).	41
4.5	The mean vertical velocity for eight depths from the model (solid line) and Roulund et al. [1] experiment (circle).	42
4.6	The vertical velocity profile from Roulund et al. [1] experiment.	43
4.7	The vertical velocity profile at at $-2 \ll x/D \ll 2$ and $y/D = 0$	44
4.8	The horizontal velocity vectors and streamlines plot for $t = 0$ s at $\sigma/D = -0.50$	45
4.9	The horizontal velocity vectors and streamlines plot for $t = 7$ s at $\sigma/D = -0.50$	45
4.10	The horizontal velocity vectors and streamlines plot for $t = 16$ s at $\sigma/D = -0.50$	46
4.11	The horizontal velocity vectors and streamlines plot for $t = 0$ s at $\sigma/D = -0.50$	46
4.12	Horizontal velocity magnitudes for $\sigma = -0.05$, $\sigma = -0.25$, $\sigma = -0.50$ and $\sigma = -1.0$ layers.	47

4.13	Instantaneous streamwise velocity in 120 s period obtained by the model.	48
5.1	Schematic view of the flow over single groyne with both upstream (denoted by index S1 and A1) and downstream separation and reattachment points (S2 and A2). The figure is modified from Paik and Sotiropoulos [104].	50
5.2	Triangular mesh of 5 m, 2.5 m and 1 m for the test-cases	51
5.3	The instantaneous velocity magnitudes of 5 m, 2.5 m and 1 m triangular mesh size	53
5.4	Location of the observation points	53
5.5	The simulated current magnitude of ASM model (line) and Liek et al. [11] model (circle) at the region close to the inlet (a) and downstream side of the groyne (b)	54
5.6	The evolution of vortical structures at $t = 01:23:10$ to $t = 01:23:40$	56
5.7	The evolution of vortical structures at $t = 01:23:55$ to $t = 01:24:25$	57
5.8	Mean flow features at three vertical layers, top) $H = -0.05$ m, middle) $H = -2.60$ m and top) $H = -4.90$ m	59
5.9	The instantaneous 2-D streamlines and resolved TKE for 5, 10 and 14 seconds.	60
5.10	The monitoring points (top) in which colour indicating flow magnitude and energy spectrum of streamwise velocity fluctuations (bottom).	61
5.11	Mean flow velocity at three vertical layers, top) $H = -0.05$ m, middle) $H = -2.60$ m and top) $H = -4.90$ m	62
5.12	Mean current magnitude along the horizontal line at (a) $Y/D = 1.0$ and (b) $Y/D = 0.5$	63
5.13	Mean flow velocity at the free surface in the upstream groyne region	64
5.14	The instantaneous velocity and 2D streamlines at three sigma layers, $\sigma = -0.05$, $\sigma = -0.26$ and $\sigma = -0.99$	65
5.15	Mean 2D streamlines and resolved TKE at three sigma layers, $\sigma = -0.05$, $\sigma = -0.26$ and $\sigma = -0.99$	66
6.1	Schematic illustration of numerical simulation: # indicated four cross-section measurement points of laboratory test (modified from Yossef [19, p. 31])	69
6.2	Visualization of flow structure using 2-D mean velocity streamlines near free surface $h/D = 0.03$	71
6.3	Visualization of flow structure using 2-D mean velocity streamlines at $h/D = 0.06$	71
6.4	Visualization of flow structure using 2-D mean velocity streamlines at $h/D = 0.10$	72
6.5	Visualization of flow structure using 2-D mean velocity streamlines at $h/D = 0.125$	72

6.6	The mean velocity streamlines (left) and velocity magnitude (right) of $h/D = -0.05$, $h/D = -0.26$ and $h/D = -0.9$	74
6.7	Flow pattern in the fourth groyne field	75
6.8	Stream-wise and span-wise velocities from the model (dashed blue line) and experiment (black line) at point A2 (see Figure 6.1)	76
6.9	Autocorrelation functions of stream-wise velocity fluctuations at sections A and D. Point 1 and 2 are located inside the groyne field.	77
6.10	Energy density spectra of stream-wise velocity fluctuations at sections A and D. Point 1 and 2 inside the groyne field	78
6.11	Mean distribution value of suspended sediment concentration in $\sigma = -0.05$, $\sigma = -0.50$ and $\sigma = -0.99$	79
6.12	Bedload transport rate	80
6.13	a Cross-section lines, b The bedload transport rate in the transverse direction of A, B, C and D sections	81
6.14	a Cross-section lines, b The suspended transport rate in the transverse direction of A, B, C and D sections	82
6.15	Bed levels change after 50 hours simulation	83

List of Tables

4.1	Test condition for the rough-bed experiment (modified from Roulund et al. [1])	38
5.1	The input parameters for the flow over single groyne test	51
6.1	Conditions for flow over a series of groyne	70

Nomenclature

Symbols

\bar{S}_h	The horizontal strain rate tensor of ASM model	-
\bar{S}_{ij}	The strain rate tensor	-
\bar{S}_v	The vertical strain rate tensor of ASM model	-
\bar{u}	The resolved flow velocity in x -direction	ms^{-1}
-	The filtered properties or quantities in the resolved scale	-
Δ_h	The grid size in horizontal direction	m
Δ_v	The grid size in vertical direction	m
κ	von Karman constant	-
\mathbf{V}	Horizontal velocity in Cartesian-coordinate	ms^{-1}
ν	Molecular diffusivity	
ν_h	The horizontal eddy viscosity of ASM model	-
ν_v	The vertical eddy viscosity of ASM model	-
Φ	Non-dimensional bedload transport rates	-
ϕ	The dynamic pressure	Pa
ρ	The total density	Kgm^{-3}
ρ_0	The reference density	Kgm^{-3}
σ	Vertical layer in σ -coordinate	
τ_{ce}	The critical erosion stress for the i -th sediment class	-
τ_{sf}	The bottom shear stress	-
$\tau_{SGS,ij}$	The SGS stress in SM	-

τ_{ij}	SGS shear stress	
τ_{bot}	Bottom stress	m^2s^2
τ_{surf}	Surface wind stress	m^2s^2
\mathbf{F}	The horizontal diffusion term	
θ_{sf}	Non-dimensional Shields parameter for skin stress	-
∇_{\perp}	The divergence symbol	
ζ	Surface elevation	m
C, C_{source}	Tracer quantity	
C^i, C_{source}^i	Sediment concentration and source of i -th sediment class	-
C_d	Drag coefficient	-
C_h	The horizontal eddy viscosity coefficient of ASM model	-
C_{ij}	The Cross-SGS term	-
C_s	Smagorinsky constant	-
C_v	The vertical eddy viscosity coefficient of ASM model	-
D	The length of the structure	-
D_w	Total water depth	m
E_s^i	The surface erosion mass flux	$kgm^{-2}s^{-1}$
f_p	Wave spectrum frequency	Hz
H_s	Significant Wave Height	m
K_h	The coefficient of thermal vertical eddy viscosity	
K_m	The coefficient of vertical eddy viscosity	
l_h	The horizontal length scale of ASM model	-
L_{ij}	The Leonard's-SGS term	-
l_v	The vertical length scale of ASM model	-
P_{bs}	The porosity of the top bed layer	-
q_{blx}	The bedload transport vector in x -direction	$Kgm^{-2}s^{-2}$
q_{bly}	The bedload transport vector in y -direction	$Kgm^{-2}s^{-2}$

q_{bl}	The bedload transport rates	$\text{Kgm}^{-2}\text{s}^{-2}$
R_{ij}	The Reynold's-SGS term	-
u'	The unresolved flow velocity in x -direction	ms^{-1}
w	vertical velocity in Cartesian-coordinate	ms^{-1}
w_s^i	sediment settling velocity of i -th sediment class	-
X	The normalised x-coordinate	-
x, z	Horizontal units in Cartesian-coordinate	m
Y	The normalised y-coordinate	-
z	Vertical layer in Cartesian-coordinate	m
z_0	Bottom roughness parameter	m
z_{ab}	Half of the first grid distance	m
Zb	The injection layer	m
$H(x, z)$	Bottom topography	m

Abbreviations

2D-HLES	The two-dimensional Horizontal Large Eddy Simulation	-
2DCS	Two-dimensional coherent structure	-
ADM	Approximate Deconvolution Models	-
ASM	Anisotropy Smagorinsky [3] Model	-
DNS	Direct Numerical Simulation	-
DSM	The Dynamic Smagorinsky Model	-
HV	The Horseshoe Vortex System	-
LES	Large Eddy Simulation	-
RANS	Reynold's Averaging Navier Stokes	-
SFS	Sub-Filter Scale Model	-
SM	The SGS- Smagorinsky [3] model	-
SSL	The separated shear layer	-
SSM	The Scale-Similarity Model	-

WAV The wall attached vortex

-

Acknowledgements

I would like to express my gratitude to Dr. Ming Li of School of Engineering, University of Liverpool as my primary supervisor, for his attention, guidance, advice and continuous support throughout this research. I would also like to thank my secondary supervisor Prof. Yan Zhou for her valuable advice and guidance.

I would like to thank all engineering staffs of BTIPDP-BPPT in Yogyakarta and The Research and Innovation in Science and Technology (RISET) Project scholarship program for all discussions and providing financial funding during my study in University of Liverpool.

I would like to thank my family, my wife Rindu, for her valuable support when I have been stressed, depressed and being amazingly supportive, loving and caring. I would also like to thank my friends, roommates and colleagues for their support and for all the great times.

At last, I would like to thank Prof. C.S. Chen of the University of Massachusetts-Dartmouth for providing the source code of FVCOM. Furthermore, This research is aided by the computational support from the Barkla High Performance Computer at University of Liverpool.

Chapter 1

Introduction

1.1 Research background

Coastal zone offers multiple services for the community, from protecting the hinterland against flood to paving the way for local economic activities through load/unload goods in the harbour. For most nations, coastal areas are valuable resources and a lot of effort has been made to protect it's presence. Unfortunately, any kind of protection influences the coastal environment by modifying its equilibrium that sometimes can lead to several issues. In order to optimise the functions without further affected the coastal dynamics, a coastal manager must understand the processes, interaction each element, and the interference to the neighbour system.

Due to increasing demand on coastal preservation, the impacts of the structures have to be investigated. From a hydrodynamic viewpoint, as the flows pass structures large scale coherent eddy is introduced into the main flow. Hsu et al. [4] explained that the vortex have faster velocity magnitude compared with the surrounding flow fields and caused larger scouring impact on the structure that lead to many failure cases.

To understand the nature of vortex eddy structure, it is important to examine the vortex existence in the larger area. The shallow wake is revealed by the airphoto or satellite when the flow past islands, headlands or other large obstacles in shallow coastal or estuary as shown by Figure 1.1. Sometime this structure is observed as turbidity concentrations, temperature distributions, or pollution sources. Ingram and Chu [5] found that the island wake depends on the stability of transverse shear layer developed along the two sides of the island. When the transverse shear is large, a vortex street is formed while in opposite condition a clear water wake of low turbulence and sediment concentration are observed.

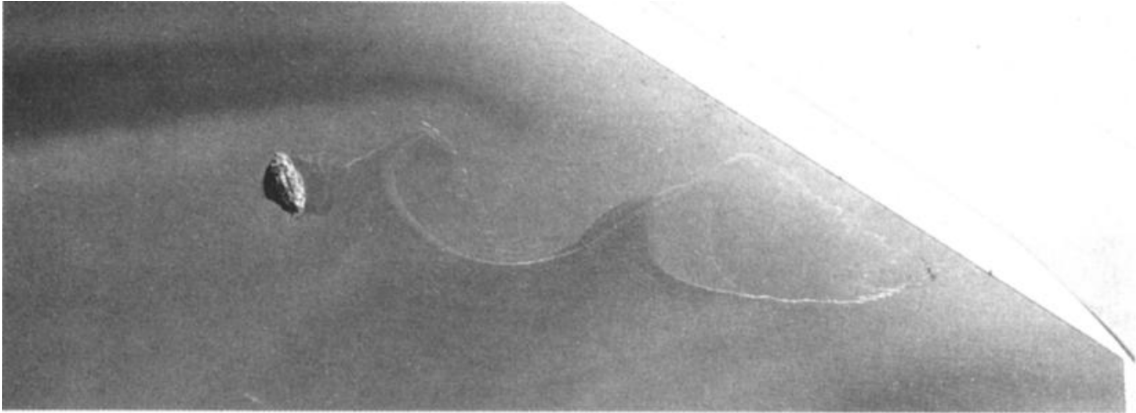


Figure 1.1: Vortex street wake at island with diameter 160 m. Figure is obtained from Ingram and Chu [5].

An improved understanding of the detailed behaviour of eddy structure is required for a number of reasons, for instance, the tendency of pollution trapping in the lee side of island and pattern of sedimentation (Chen and Jirka [6]). A comprehensive physical experiments from Carmer et al. [7] has shown the role of vortex structure in trapping tracer mass and increasing a significant mass exchange between eddy of opposite rotation. Due to its significant role in the transport process, it is important to accurately define the flow fields as vortex structure or random turbulence motions. Venditti et al. [8] highlighted a crucial characteristic of the large coherent structures. They must have temporal and spatial coherence in addition to the fact that they generate Reynold stress and turbulence intensity, and posses vorticity which implied rotational aspect to the structure. It takes form as hairpin, horseshoe, or cane vortices in the flow fields.

The role of coherent structures in controlling the sediment dynamics has been examined for flow within bottom boundary layer above bed forms. For instance, Leftheriotis et al. [9] presented a numerical study for oscillatory flows with fixed ripple bed for different steepness values. They concluded that the suspended sediment rise over ripple bed is parallel to the level reached by the resolved structures in the active layer. Meanwhile, Kostaschuk and Church [10] observations of macro-turbulence from acoustic soundings of the water column in the Fraser Estuary showed structures lifting off the bed in the lee of large-scale dunes. Furthermore, the structure-induced flow separation and vortex shedding is well known in the literature. However, the inability to resolve eddy structure lead to under-predicted local scour around structures. Such a finding has been reported by Liek et al. [11] when simulated flow over single groin. The later study highlighted that the morphological results showed better performance when the resolved eddy is accounted in the model. Recent works of Vouriot et al. [12] described that the generation and evolution of vortex structure can influence sedimentary processes. This finding is supported by Kim et al. [13] that identified a pattern between the occurrence of recirculation region and the

local suspended sediment transport regime inside artificial lake.

To include the large coherent structures in the coastal models requires a proper approach for dealing with the shallow turbulent flow. The present coastal models adopt Reynold Averaging Navier-Stokes (RANS) concept which is based on time-averaging procedure over certain periods. However, such time-averaged approximation has one principle difficulty with respect to the fact that the turbulence model should represent all range of spectrum. Hinterberger et al. [14] describes the coexistence of 3D, small-scale, mainly generated bottom turbulence and large-scale 2D eddy leads to two range spectrum. Moreover, the complex situation with 2D and 3D turbulent structures is difficult to handle in RANS with respect to the implementation of statistical turbulent model. In other word, the time averaging procedure in the RANS based models will diminish the large-scale, 2D coherent structures. As a result, the RANS models often not perform well where large scale coherent eddy exist, for instance in the flow pass single groyne or breakwater. This condition is more critical to modelling sediment transport process, as many large scale coherent eddy induced sediment motion will not be accounted by the RANS model causing large error in the present morphodynamics predictions.

From this point of view, an alternative technique is required to properly account, for the coherent structures. It is worth to note that the technique should be able to resolve and maintain the existence of eddy structure in the mean flow. More importantly, it can produce turbulence generations near coastal structures. In this research Large Eddy Simulation (LES) is adopted as a basis for solving the shallow turbulent flows induced by coastal structures. The LES procedure separates the small local scale processes from the large scale coherent structures and resolve the latter terms directly. Through this way, the inconsistency in the RANS can be avoided. At the same time, as the large scale turbulence contains most energy, LES is therefore expected to be able to describe the energy generation and dissipation more accurately. LES application in coastal modelling mostly can be found in the wave breaking study, where flow mixing, sediment entrainment and sediment transport all affected by the presence of coherent structures and their interaction with boundaries and other flow structures. In this study, we extend the LES application to solve shallow turbulence flow induced sediment transport near coastal structures and applied it in the real-scale engineering problems.

By adopting the LES approach into coastal models delivers both great advantages and challenges in coastal sediment study. On one hand it gives opportunity to observe the role of coherent structures in the coastal sediment transport of certain Reynold's number. On the other hand, due to the complex geometry in the coastal zone, it is required to account anisotropic turbulence in the models. As a consequence, the different filter size for horizontal and vertical directions is needed. Carati and Cabot [15] described the possible approach to account the anisotropy effect induced by an axial vector by using

Germano et al. [16] dynamic procedure to calculate eddy viscosity. However, this technique is highly demanding and more suitable to be used for near-field modelling. Therefore, less demanding approach, Anisotropy Smagorinsky Model (ASM) introduced by Roman et al. [17] is used as procedure to calculate eddy viscosity.

It should be noted that the time span in which has been focussed on in the present study is longer than typical coastal wave period. Therefore, the wave dynamics is still considered in the wave-phase-averaging approach rather than a CFD type of simulation.

1.2 Research questions

Based on the aforementioned discussion, the emphasis of this research is to investigate the effect of the coherent structures in the mean flow with respect to the presence of coastal structures, by adopting LES approach into a 3D hydrodynamic model. Moreover, this objective is addressed by answering the following research questions:

- **RQ1:** To what extends the existence of 2-D eddy influenced the mean flow dynamics around groyne structure?
- **RQ2:** How far is the eddy interaction affected the turbulent kinetic energy?

To answer the aforementioned questions, the coastal morphodynamics modelling suite developed by Zheng et al. [18] is adopted as basis. A new LES model is then developed and coupled with the Zheng et al. [18] model to reveal the influence of coherent turbulence structure on flow hydrodynamics. The model is further tested for flow coastal structure-induced large scale eddy.

1.3 Research Outline

The outline of this thesis is presented as follows:

- **Chapter 1** describes the context of the present study through briefly discussed the importances and challenges of corresponding subjects and addressed research questions
- **Chapter 2** introduces the basic theory of shallow turbulence flows, hydrodynamic and sediment models.
- **Chapter 3** explains the state of the art of LES concept in FVCOM, the implementation of ASM-LES in FVCOM and adopted numerical procedures
- **Chapter 4** presents the validation of the model for flow over a cylinder. Model results is compared with the Roulund et al. [1] physical experiment.

- **Chapter 5** shows model performance for simulating typical real-scale problem of flow over single groyne.
- **Chapter 6** describes the application of the developed model into laboratory scale experiment conducted by Yossef [19] to fully test the model performance in resolving large scale coherent structures, it affects in the sediment transport and relatively short time morphology evolution.
- **Chapter 7** summarises the main findings and recommendations for future study.

Chapter 2

Coastal Processes and Numerical Modelling

This chapter describes coastal processes, shallow turbulent flows, coastal modelling, turbulence in coastal flows and technique to include a turbulence term in numerical models.

2.1 Turbulence modelling

It is important to describe coastal hydrodynamics in general in order to focus the study in the specific application range. Similar to other environmental flows which are ubiquitous in nature, coastal flow is categorised as shallow turbulent flows due to its larger lateral dimension in comparison with the water depth. Moreover, man-made structures such as breakwaters, groins, and abutments introduce a disturbance in the shallow near-equilibrium vertical shear flow and create mixing region regarding flow velocity differences. Large, two dimensional coherent structure, then shed off from the base flow. Following Jirka [20] terminology,

"2-D coherent structures (2DCS) are defined herein as connected, large-scale turbulent fluid masses that extend uniformly over the full water depth and contain a phase-correlated vorticity (with the exception of a thin near-bottom boundary layer)".

As the structures easily to be found and have a clear influence in the coastal flow transport mechanism, it is relevant to have insight into the method of investigation, physical behaviour and forcing mechanism of these features.

2.2 Method of investigation

Despite airborne and satellite images produced a well qualitative impression to uncover shallow turbulent flow dynamics as well as their general behaviour, quantitative ap-

proach is required to gain better understanding of the underlying physical mechanism of stabilise/de-stabilise factor of shear flows in more precise. Therefore, a collective work consists of field measurements, laboratory experiments and numerical simulations has been reported in the literature.

Field measurement. In the coastal region the momentum and energy balance are influenced by various parameters among others two significant terms are the bottom shear stress and dissipation rate. The former parameter directly affects coastal circulation and also generates turbulence into the main flow while the dissipation rate controls the entire energy budget. Field measurement is used to collect field data and study the real turbulence characteristic. For instance, Doron et al. [21] collected 20 x 20 cm² instantaneous velocity for various elevations from 10 cm to about 1.4 m above the sea floor by using a submersible Particle Image Velocimetry (PIV) system at the New York Bight. Data processing at each elevation showed the presence of large-scale shear even at the highest measurement level while spectral analysis of the energy and dissipation spectrum revealed anisotropy feature from flow fluctuations. The study had significant finding for describing real velocity fluctuation dynamics for both vertical and horizontal components. It revealed that the velocity fluctuations from the vertical component significantly damped as reached the bottom contrast to the horizontal component which able to maintain its energy level. Such technique is very demanding from a cost point of view and it is almost impossible to obtain long data series by using this technique, therefore alternative procedures such as a laboratory experiment and numerical simulation gain more attention.

Laboratory experiment. The emphasis of this approach is to scale down the shallow turbulent flow into a laboratory dimension without further affected the underlying physical mechanism. Particular attention for installing appropriate instruments is required to establish a horizontally uniform and homogeneous shallow flow. Moreover, high accuracy measurement at the bottom bathymetry is essential to investigate a disturbance in the vertical shear flow. Non-intrusive optical techniques which involved Laser Doppler Velocimetry (LDV), Laser Induced Fluorescence (LIF), and Planar Concentration Analysis (PCA) are recommended.

Numerical simulation. Parallel with the advancement of computational power, numerical approach greatly benefits from this improvement. Despite its implementation remain limited for engineering tasks, Direct Numerical Simulation (DNS) has shown important contribution to study turbulent flows at certain Reynold numbers. DNS is highly demanding and only suitable for simple case with low Reynold numbers. More suitable approach to solve large-scale coherent structures is by adopting LES procedure. This approach solves spatially-filtered Navier-Stokes equations which described as the large, high containing energy turbulent eddies. Despite being relatively new field for coastal modelling, LES models provide a powerful tool for investigating turbulent dynamics and

small scale processes (Burchard et al. [22]).

2.3 Basic Nearshore processes

2.3.1 Nearshore Circulation

The generation of coastal cell circulation is discussed following the radiation stress concept introduced by Longuet-Higgins and Stewart [23]. It is defined as the excess of stress in the momentum due to the presence of the waves. Moreover, it is highlighted that the shoreward component of the radiation stress imposes a set-down in the offshore of the breaking zone and set-up within the surf zone. From 3D point of views, the coastal circulation takes place which is constituted by the long-shore and cross-shore currents. The long-shore currents are parallel to the shoreline and carry sediment along the shoreline. It is a product of the shoreward component of the radiation stress and waves breaking for the obliquely incoming waves. On the other hand the cross-shore currents are generated to compensate the onshore mass flux which occurs due to the difference of wave trough and crest mass flux.

Cross-shore currents: It is constituted by the shoreward flows at the surface and offshore directed flows above the bed known as the undertow currents. These flows typically exist during high energy wave conditions (Svendsen [24]) and the effects are relatively large for the breaking waves. In addition, wave height decreases produced a horizontal momentum gradient that's balanced by the pressure gradient. As a consequence, the offshore directed undertow velocities increase in the breaking region and it may contribute to carry out more sediment to the sea.

Long-shore currents: It can be induced by obliquely incoming waves or due to the tidal induced long-shore gradient in the mean water level. The waves are constituted by cross- and long-shore components in which the long-shore component produces a mass flux (caused by wave crests and trough differences). Feeding by the breaking waves to add more mass flux along the shoreline with no boundary condition as in the cross-shore direction, the currents are in the same direction for the whole water column.

The coastal circulation, which now consists of the feeder long-shore currents, offshore directed undertow currents and a shoreward return flows, greatly depends on the wave height variations along the shoreline. In addition, the presence of breakwater and jetties can affect the incident waves by partial sheltering of the shore and creates the significant variation of the wave height and the set-up. Particularly for single groin case, the interruption of the littoral transport produces deposition along the up-drift side and erosion at the down-drift side.

2.3.2 Coastal Sediment Transport

The wave motions play an essential role in disturbing the sediment on the seabed. Within the inner surf to the more deeper region, waves induced currents produce mega-ripples or almost flat bed due to the very shallow water depth and the energetic oscillations. Close to the breaking region, the sediment fractions are transported in the very thin, high sediment concentration layer close to the bed termed as the sheet flow region. In addition, large amounts of sediments is transported from the water surface to the whole water column due to the wave-breaking induced vortex structure at the breaking point.

Generally speaking, the sediment transport mechanism is divided into two categories; (1) the bed-load and (2) suspended transports. Despite no precise definition regarding these mechanisms, bed-load transport is determined as moving sediment grains below a particular reference elevation near the bed (Van Rijn [25]) with more/less contact with the bed (Deigaard et al. [26]) while the suspended transport is described as sediment movement driven by turbulence induced fluid drag around near-bed reference level (van Rijn [27]).

Bed-load sediment transport : The bed shear stress induced by waves and currents acts as driving mechanism in the bed-load sediment transport. The sediment starts to move when the shear stress exceeds the critical value. For sandy particles, commonly ripples start to form and as the bed shear stress increases, the ripples successively reach the equilibrium. Moreover, the ripple height and length are increased until the ripple steepness and roughness reach the maximum level. The ripple formations can be washed out leaving only the plane bed if the bed shear stress continues to elevate. Such condition produces two different regimes, the ripple and flat-sheet bed. The former regime usually develops in the the inner surf zone and deeper water where mildly energy conditions are found. In contrast, flat-sheet regime is commonly observed at the breaking and swash zones under large orbital velocities and energetic waves.

Due to its importances in the sediment transport mechanism, ripple hydrodynamics have been studied by using both experimental and numerical techniques. For instance, Fredsøe et al. [28] observed that the turbulence near the bottom increases markedly parallel with the lee-wake vortices are washed over the ripple and convected in the direction opposite to the flow. Furthermore, Grigoriadis et al. [29] highlighted the dominant effect of ripple height and the oscillatory part of the flow. Steeper ripples are strongly associated with larger recirculation zones, stronger turbulence and higher forces exerted on the bed. On the contrary, the effect of current strength is relatively weak on the forces and the flow pattern developed over the ripples.

Other aspects of hydrodynamics, the boundary layer streaming related with the progressive waves and wave asymmetry, influence the bed load direction in offshore and shoaling regions. When the sheet flows occur, sediment moves within a thick layer and

the direction is affected by the wave asymmetry. Moreover, physical factors that affected the movement of sediment is the bed slope. It will either be increased or decreased the sediment transport rate depending the slope angle. The presence of a breaking bar will dominate the transport around the steep side and even caused to avalanche.

Suspended sediment transport : The bed shear stress can lift the sediment grains and set it into suspension. Forced by an upward-directed pressure gradient which is attached to the bed shear stress induced vortices (Van Der Zanden et al. [30]), gravitational settling and vertical advective and diffusive mixing lead to the equilibrium concentration profile in the vertical direction. This profile follows an exponential or power-spectral distribution depending on the mixing length. Higher entrainment and mixing rates under breaking waves lead to an increase in concentrations at outer flow elevations compared to shoaling locations (Nielsen [31]; Nadaoka et al. [32]; and Aagaard and Jensen [33]). Due to the massive amount of turbulent kinetic energy transported under breaking waves, a strong, non-uniformity pick-up rates are set up. Such a finding confirms that the high instantaneous bed shear stress (Cox et al. [34]) and upward pressure gradient (Sumer et al. [35]) are generated due to the non-local effect of the turbulence.

The vertical distribution of suspended sediment can be determined by using classical mixing length concept where settling and diffusion term is integrated over water depth (Deigaard et al. [26]). For current related sediment transport, the direction can be offshore or onshore depending on the vertical distribution of time average concentrations and undertow-streaming velocities. In the breaking zone, the magnitude of undertow currents increase and produce offshore directed sediment transport. Such condition generates non-uniform net suspended transport rate and alter sediment balance at a particular cross-shore locations. The net suspended transport rate is not only controlled by local vertical processes, but also by the net influx from the adjacent points (van der Zanden [36]).

The breaking waves in the surf zone introduce an extra force into sediment transport. Driven by breaking-induced vortices, a significant amount of turbulent kinetic energy is ejected into the water column (Rijn et al. [37]) leading to increased bed shear stress and bed-load transport, pick-up and turbulent mixing of suspended sediments.

2.4 Coastal Models

The coastal models are used as interactive tools to study coastal dynamics. It consists of several models such as, waves, circulation and sediment models. Brief reviews associated with the existing coastal models are discussed in the following sections.

2.4.1 Wave Models

The wave models are required to produce wave characteristics at a particular location which cover local wind-waves and swell. There are two types of wave models, the phase-resolving and phase-averaged models. For a small scale region, the phase-resolving models are recommended while the phase-averaging models more suitable for simulating waves in the large area. The former models obtain wave characteristic by tracing the instantaneous water surface and predicting the amplitude and phase for each wave. Despite the ability to represent many important wave processes such as wave-wave interactions, wave nonlinearities and wave structure interactions, adopting these models for large scale is almost impossible from a computational point of views. In contrast, wave phase-averaged models solve a wave spectrum and its integral parts such as ($H_s, f_p, etc.$) based on the assumption that the wave phase slowly changes.

This technique consumes less computational power so that suitable for regional wave modelling. It should be noted that almost all present wave models are phase-averaged which belong to the third generations (WAM, SWAN, WAVEWATCHIII, etc.). Among of them, The Simulating WAVes near-shore (SWAN) is designed to simulate wave propagation from the deep water to the surf zone (Booij et al. [38]). This model has produced satisfactory results for simulating wave condition in the near-shore area (Strauss et al. [39]) includes many important wave dynamics, such as shoaling, refraction, wave-wind interaction and wave breaking. Recently, the unstructured version of SWAN has been developed to accommodate the complex geometry such as coastal structures or headlands. Many works have been carried out to extend the model capability for simulating important wave dynamics around structures. More recent work by Zheng et al. [18] has successfully coupled SWAN with the FVCOM to resolve the critical wave current interactions. All of these development enables SWAN to be used for coastal application around structures.

2.4.2 Circulation Models

Coastal models typically adopts a set of primitive equations including hydrostatic and Boussinesq approximation, which is based on the RANS equations. It is very common to derive the governing equations on the rotating Earth by using the Boussinesq assumption. The reference density (ρ_0) is thus applied instead of density in the all terms except the gravitational term leading to a consequence where the mass conservation is succeeded by the conservation. To accommodate the turbulent effects, a parametrised way is introduced rather than to numerically solve them. An assumption is applied in these procedures that the ensemble averaging of the RANS equations resulting the Reynold stresses. The hydrostatic approximation neglecting the horizontal force of Earth rotation in the horizontal momentum equations is imposed for the Coriolis terms (Klingbeil et al. [40]).

In a vertical direction, a constant number of levels to normalise the water depth is introduced by Phillips [41] as a procedure for better description of the bottom. The vertical coordinate system known as terrain-following coordinate has been adopted in the numerous coastal models, for example Princeton Ocean Model (POM) (Blumberg and Mellor [42]). Over the last years, this concept has been modified with generalized topography following coordinate system as a procedure to keep high resolution in a wide range of water depth (Chen et al. [43]). It is common in a coastal model to adopt the time splitting schemes. The reason is to solve free surface wave propagation (barotropic mode) and internal mode separately, with distinct time step. Parameters are solved in each mode and transferred to solve the model equations (Lazure and Dumas [44]).

External mode is classified into two parts: explicit and semi-implicit or implicit models. Popular models such as POM (Blumberg and Mellor [45]) and Regional Ocean Modelling System (ROMS) (Shchepetkin and McWilliams [46]) are used explicit schemes, in which the ratio between internal and external time steps is around 10-50. In contrast, the implicit or semi-implicit scheme of external mode give opportunity to use larger time step. The CFL (Courant-Friedrichs-Levy) criteria is no longer used in this scheme lead to equal time step for external and internal mode.

The small scale process in the vertical direction is very difficult to resolve. Therefore, a turbulence closure system based on a statistical approach is traditionally used. In the recent years, two-equations turbulence models, such as $k - k\epsilon$ and $k - k\omega$ have been improved to better parametrise the unresolved processes such as horizontal mixing, Langmuir circulation (Lc) and internal waves (Burchard and Petersen [47]). Nevertheless, the present of structures which shed off the vortexes from the main flow is still neglected with respect to the implementation of averaging procedure in the RANS based turbulence models. As a consequence, it underestimates the magnitude of the flow around the structure and fails to account vortexes induced sediment transport. Typical example of such model includes FVCOM (Chen et al. [48]). In comparison with other existing models, FVCOM has the advantage when dealing with the complex geometry in the coastal area. Following works by Zheng et al. [18] the model presents capability to fully represent the wave-current interaction based on vortex force scheme. Therefore in the present study, new version of FVCOM updated by Zheng et al. [18] is used as the modelling suite.

To gain better performance for resolving the flow around structures, LES is adopted in the present study in which the large scale turbulent is directly solved through spatial filtering and the small scale effect is parametrised by the subgrid closure system.

2.4.3 Sediment Transport Models

Suspended Sediment Transport Models

The suspended sediment transport model is generally developed based on the advection-

diffusion equations. Each term is solved independently commenced by vertical settling, source/sink, horizontal advection, vertical advection, vertical diffusion and the horizontal diffusion. A parabolic method to integrate depositional flux over multiple grid cells is proposed in the vertical advection algorithm (Warner et al. [49]). The diffusion term which determined sediment fluxes in the horizontal and vertical directions is obtained by either integrating the turbulent viscosities into sediment model or purely empirical.

A bottom boundary condition is used to describe the exchange mechanism between the bed and sediment in the suspension. Moreover, it takes a form of a reference concentration at an elevation above the bed, or a pick-up function of non-breaking waves where the bed shear stress from waves and current act as driving force. Parametrisation procedures, then developed to account the wave breaking effects at the near bed flow and turbulence induced bed shear stress through, adding TKE as additional sources for both bed shear stress and sediment concentrations (Hsu and Liu [50]; Okayasu et al. [51]), or using local wave breaking parameters, for example the wave height at breaking (Jayaratne and Shibayama [52]) and the wave roller dissipation (Kobayashi and Johnson [53]).

Bed-load Sediment Transport Models

To solve bed load transport predictions in the engineering projects, an empirical formula is mostly used rather than process-based numerical models due to its simplicity. Different model concept can be used in order to predict coastal sediment transport. These range from empirical or theoretical transport formula (quasi-steady and semi-unsteady) to more advance concept such as bottom boundary layer.

Quasi-steady models assume that sand transport reacts directly to changes in flow condition. Sediment transport is calculated as function of bottom shear stress and near bed velocity. In addition, the unsteadiness of flow processes are not accounted (da Silva et al. [54]).

Over the last years, semi-unsteady formulas are developed to account the phase-lag effect in the particular cases, e.g. sheet-flow condition (Camenen and Larson [55]), ripple bed conditions (van der Werf et al. [56]), and for both sheet-flows and ripple bed conditions (da Silva et al. [54]; van Rijn [57]; Van Rijn [25]; van Rijn [27]). The presence of unsteady effects in sediment transport is considered in this concept.

2.5 Turbulence in coastal processes and LES modelling

One of the emphasis in the present study is to resolve large scale coherent structures that shed off when the flow pass obstacles. This condition leads to unbalance of vertical shear flow and changing the whole distribution of the momentum at the bottom boundary layer. To take into account the existence of this event, a proper turbulence model is required to

extract the high containing energy from the main flows. However, the Reynolds decomposition in the RANS based turbulence models removes the eddy structures and lead to the under-predicted velocity magnitude. Furthermore, the present of 2DCS has significant influence in the transport mechanism of passive materials. Move beyond approximate procedures by resolving the largest scales of turbulent using filtered Navier-Stokes equations, LES has the capability to obtain vortex structures without consuming too much computational power. Burchard et al. [22] stressed LES ability as a powerful tool for examining the formation of turbulence and other small scale processes in the coastal flow.

2.5.1 Generation of the large scale coherent structure

A turbulent flow has a unique character as it is irregular, random and chaotic, unsteady, and the motion of eddy is unpredictable (Pope and Pope [58]). Transfer energy in turbulent flows is done from large to small eddies known as the cascade of energy.

Turbulence is generated by winds, waves, tides in coastal through the development of mean shear flow. On the contrary, the destruction is done by dissipation or converting into potential energy for instance in breaking waves process. Following Burchard et al. [22], turbulent study in coastal is divided into three subjects as surface, bottom boundary layer, and stratification. At the water surface, the presence of thin skin layer disturbed by waves breaking. This mechanism leads to TKE injection near the surface and affects the vertical transport of substances near the surface.

For wind-induced current three layers are formed following breaking wave process. The first layer is the injection layer (Z_b) which has the highest value of dissipation rate. Below this layer, TKE directly transferred downwards and dissipated. At Z_b where the distance is far enough from surface thin skin layer, the effect of turbulent is small compared to local shear production. There are two possibilities for the lower boundary of the surface layer. The first one is directly as seabed as a consequence of shallow water condition and another one is pycnocline layer which enhances by the vertical gradient of salinity and temperature. The interaction of current and wave boundary layer together with sediment movement produces turbulent near the bed. Hence, a bottom boundary layer spans from no-slip motion region next to the bed until the free stream velocity area. While current and wave-boundary layers are developed, non-linear interactions occur between these layers. An intermediate layer is detected between surface and bottom boundary layer. While this layer is not permanent, vertical stratification support the internal wave development. Regarding to this classification, the focus of turbulence layer is in surface and bottom boundary layer.

With the presence of coastal structure, large scale turbulent is generated due to the shear instability in the flow around the structure. The most common and complete example is the flow around vertical cylinder as discussed by Sumer et al. [59, p. 2]. In his study,

different vortex shedding can be generated over certain Reynold's number and structure configurations. This phenomena can also be found for flow structures, such as breakwaters, groynes, harbours and more often in the present day offshore wind farm foundations. Unlike those coherent structures generated at the surface or bottom boundary layer region, the large coherent eddy tends to remain in 2D and once it generated, they grow in size detached from the structure surface, e.g. free-shear flows. However, these large eddy also dissipate into smaller forms through energy cascade process.

The fact that coastal flows are characterised as predominantly horizontal flows and interrupted by structures, triggers the development of two-dimensional coherent structures. These features highly correlated with the vortical motion and play essential in transport of mass and momentum (Von Carmer [60]). The large structure eddy contains vorticity which has been imparted from the initial transverse shear during the generation stage. Moreover, three type generations of large structure eddy are introduced by Jirka [20] namely as:

Type A (Topographical forcing)

Being known as the most severe generation mechanism which introduced disturbance due to the presence of topographic features such as islands, headlands, breakwaters, groins and jetties), it leads to the development of local flow separation, intensified transverse shear layer and returned flows at the lee side of the structure.

Type B (Internal transverse shear instabilities)

The growth of large two-dimensional structure is triggered by velocity variations in the transverse direction due to excess or deficit of momentum in the base flow, gradual topography changes and roughness distribution.

Type C (Secondary instabilities of base flow)

This mechanism is the weakest type of generation and the evidence is very limited. Distortion from vortex lines induce two-dimensional coherent structure.

It has been reported by Carmer et al. [61] that due to the immense transverse shear at the obstacle during the generation of vortical structure a considerable amount of TKE is extracted from the main flow and transferred to the fluctuating motion of the wake flow. Interestingly, this TKE plays significant role in the prediction of suspended sediment transport. A simulation of Zheng et al. [18] revealed that the suspended sediment concentration shows an overall best agreement with the measured data when accurate near-bed TKE is imposed as a bed boundary condition. Despite the experimental findings of vortical structure producing additional value to the TKE have been highlighted, few

numerical simulations are found in the literature (see for example Liek et al. [11] and Yossef [19]). This is because the statistical turbulence model in recent coastal models unable to handle the complex interaction of 2D and 3D turbulent structures when the vortical structure exist. This study contributes to take into account the existence of eddy structure in a coastal model as an attempt to accurately calculate the TKE.

2.5.2 Vortex identification

To identify the large scale vortex structure, different indicators have been proposed in the literature. For instance, Jeong et al. [62] investigated coherent structures using a conditional sampling technique involving alignment of vorticity patches of largest size and strength. In addition, pressure minimum technique is used in their study to educed coherent vorticity and production. Another technique covers the vortex identification from sectional velocity data, for instance, the contemporary $\nabla u(Q)$ -based criteria from Chong et al. [63]. In their procedure the eigenvalue of velocity gradient tensor is used to derive local classification of the flow pattern. Subsequently, the large positive invariant of $\nabla u(Q)$ and negative second largest eigenvalue of λ_2 are used. More common procedure, such as the streamline (e.g. Tuck and Soria [64]) and vorticity strength are also have been proposed to be used for the vortex identification.

2.5.3 Predicting Turbulent Flows

The major task in turbulent modelling is capturing the turbulent motions at all scales across the whole energy spectrum. A typical energy spectrum is commonly plotted with the wave number term in logarithmic scale as shown in the Figure (2.1). Kolmogorov [65] explains the different region of the turbulence energy generation, transfer and dissipation. In the theory, Kolmogorov [65] assumed that turbulence energy depends on the rate of dissipation, ϵ , at which the smallest turbulence converted into heat, and wave number k is proportional to inverse eddy length scale. Broadly, there are three different regions as shown in the Figure 2.1.

- A low wave number region where unsteady motions permanently exist. These large eddy contains most turbulent kinetic energy.
- Transitive region where the turbulent motion scale is independent of forcing scale, and dominated by the inertial force rather than the viscous force. These eddies are responsible for transferring energy from large scale to the small scale.
- The large wave number region. In this region, the energy dissipation is dominant. These are scale of motion smaller than Kolmogorov's scale in which the viscous force starts to dominate over the inertial force.

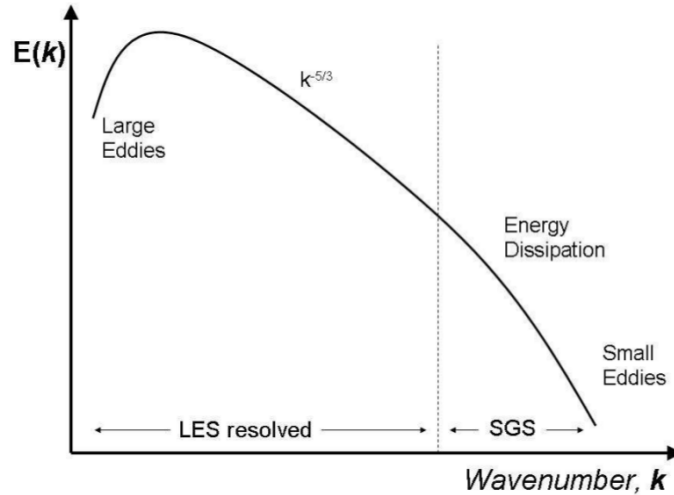


Figure 2.1: Turbulent energy spectrum (Galea [66]).

An explanation of proper methods to solve the turbulent energy spectrum has risen up in 1950's. The first attempt is with Direct Numerical Simulation (DNS). In this method all turbulent energy spectrum is solved directly without applying a model. However, the capability of this technique is limited due to the high computational cost and only possibly applied into low Reynold numbers. On the contrary, a method with low computational cost severely implemented in engineering projects known as Reynolds-Averaging Navier-Stokes (RANS) procedure. Its an averaging technique for solving Navier-Stoke equations. RANS which regularly coupling with turbulence model is based on statistical procedures. While RANS has the ability to overcome the high computational cost issue, turbulent structure is parametrised through turbulence closure scheme. As a consequence, it removes the unsteadiness and random motion of turbulent. Taking place in intermediate level of computational cost, Large Eddy Simulation (LES) solves large scale (resolved) motions explicitly by solving 3D time dependent governing equation and to model the motion of small scales. The large scales extract energy from mean flow and transfer it to smaller scales.

The basic idea of LES based on the theory of Kolmogorov's where the small scale of motion can be approximated due to the its uniform behaviour while the larger scale of motion that contains most energy is directly resolved. To separate these different scale of motions, a filter is applied to the flow momentum and continuity equations, which typically is the characteristic length scale, Δ . The scale longer than Δ will be retained in the filtered flow field, while any motion has smaller scale will be approximated by the sub-grid scale modelling.

For any flow characteristics, f , the LES solves the resolved motions \bar{f} and parametrised

the small scale motion f' as

$$f = \bar{f} + f' \quad (2.1)$$

To extend the resolved \bar{f} , the filter operation is conducted

$$\bar{f}(\mathbf{r}, t) = \oint G(\mathbf{r}, \mathbf{r}', \Delta) f(\mathbf{r}') dV' \quad (2.2)$$

Here \mathbf{r} is the location where \bar{f} is to be determined and \mathbf{r}' is the location where f is considered in the spatial integration. Δ is the filter size proportional to smallest retained motion wave length and G is the filter kernel that satisfy

$$\oint G(\mathbf{r}, \mathbf{r}', \Delta) dV' = 1 \quad (2.3)$$

There are many different LES model proposed in the literature. Following Rodi et al. [67, p. 23] classification, we divide the LES model as LES that is based on the eddy-viscosity concept such as algebraic Smagorinsky [3] model, scale similarity model, Approximate Deconvolution Model (ADM) and Sub-Filter Scale Model (SFS).

Eddy viscosity model

The majority eddy viscosity models stand behind the separation concept between the isotropic stress from the anisotropic part. It then employs the model relating τ_{ij} to the gradients of the resolved velocity through an eddy viscosity. The modelling effort corresponds to this type model is in the determination of the eddy viscosity. In the SM model, the anisotropic stress tensor is approximated by relating it to the resolved rate of strain, \bar{S}_{ij} , which involves velocity gradients through a turbulent viscosity. The eddy viscosity is not a fluid property, but characterises the unresolved sub-grid scale. Furthermore, the selection of the characteristic length-scale in this model is more straightforward than in RANS modelling. It is approximated as the property of the SM constant, C_s , and filter size Δ which proportional to the grid or mesh size in the explicit LES modelling. Up-graded version of the SM model typically deals with the idea that the C_s value should not be constant. Germano et al. [16] introduced the dynamic model to calculate the model parameters by using information from the smallest resolved scales. The test filter is then introduced with size larger than the original filter.

Scale similarity model

The Scale-Similarity Model (SSM) is proposed by Bardina et al. [68]. The idea is to assume that the smallest resolved scales are similar to the largest unresolved scales. By

using the information from both parts, an expression of the sgs stress can be obtained. The expression is then defined,

$$\tau_{ij} = \overline{u_i u_j} - \bar{u}_i \bar{u}_j = C_B (\overline{\bar{u}_i \bar{u}_j} - \bar{\bar{u}_i} \bar{\bar{u}_j}) \quad (2.4)$$

where C_B is the Bardina constant with a value of $C_B = 1.0$. The results produced by this model show an improvement in the predicting sgs stresses due to its ability to account backscatter energy transfer in the physical way. However, the SSM model does not dissipate enough energy from the large scales and in most cases it is combined with a dissipate model such as SM.

Approximate Deconvolution Models (ADM) and Sub-Filter Scale Models (SFS)

The concept of the ADM or SFS model is by using an inverse filtering procedure, also called deconvolution, in order to reconstruct the unresolved and unfiltered quantities. It should be noted that the reconstruction can only be approximated. Stolz and Adams [69] use a truncated series expansion of the inverse filter to approximate the unfiltered velocity field and then used it to compute the non-linear terms in the filtered Navier-Stokes equation. By combining the reconstruction and eddy-viscosity model higher order versions of Bardina's mixed model are obtained. The advantages of the ADM or SFS models is that they can account for backscatter and contain no parameters to be tuned. Furthermore the model does not need wall-damping functions to correctly predict the viscous sublayer.

In this study the eddy-viscosity model is adopted due to its simplicity from the numerical point of views. A modification in the Smagorinsky constant parameter is made to accommodate different filter length scale in the vertical and horizontal directions. This concept is similar with the common two-eddy viscosity coefficients in the coastal models.

2.6 Summary

This chapter describes the definition of 2DCS in coastal flows, comprehensive investigation method of turbulence structure and basic nearshore processes. Moreover, existing coastal models consist of wave, hydrodynamics and sediment modules are briefly discussed together with the LES concept as turbulent model.

The wave models are used to produce wave properties, such as significant wave height and wave period. The well established spectral wave model, SWAN, is coupled with FV-COM in Zheng et al. [18] modelling suite to solve many important wave dynamics. A 3D, hydrodynamic model based on RANS concept is widely used to solve the shallow water

equations. This model uses hydrostatic approximation neglecting the horizontal force of Earth rotation. In the vertical directions, terrain-following coordinate is introduced as procedure to describe the bottom condition. A sediment module consists of advection-diffusion based suspended transport model and a bed load formula. Each term in the suspended model is solved independently commenced by vertical settling, source/sink, horizontal advection, vertical advection and vertical and horizontal diffusions. An empirical formula is commonly used to solve the bed load transport predictions in the engineering projects.

To take into account the existence of 2DCS in coastal flows, a modification in sub-grid modelling is required. It is because in the RANS based coastal model, the time averaging procedure may remove the vortical eddy structures. Therefore, LES concept is discussed as new turbulent model.

Chapter 3

Numerical Model

This section describes the development of LES based on Zheng et al. [18] model, where a spatial filter is applied to the governing equations. This filter is considered as a convolution procedure in which similar to the Reynold decomposition, the non-linear convection term introduces an unclosed term. It is denoted, τ_{ij} , as the impact of the sub-filter scales on the resolved motion. It is worth to note that filtering in the LES is sort of a concept than explicitly applied procedure (Fröhlich and Von Terzi [70]).

3.1 System of existing model: Zheng et al. [18] model

3.1.1 Introduction

A coastal modelling system composes of several modules for representing specific coastal processes, namely wave propagation, coastal circulation, sediment transport and coastal morphology. Each model is used to reproduce physical phenomena with different spatial and/or time scales which sometimes almost possible to resolve with just one model. Parallel with the advancement of computational power, a large number of coastal modelling packages, both two- or three-dimensional models, have been developed for different scientific reasons. Many of these models have been validated and showed reasonable results for reproducing coastal hydrodynamics and sediment transport.

As a basis for investigating large scale turbulent eddy, a prognostic, three dimension, coastal morphodynamics model of Zheng et al. [18] is used in this study. Brief discussion regarding these models is presented in this section. The model system is based on the RANS filtered ocean model, FVCOM developed by Chen et al. [43] coupling with the unstructured SWAN model.

3.1.2 Circulation Model

The circulation model of Zheng et al. [18] is based on the prognostic, unstructured-grid, finite volume based ocean model. By using non-overlapped, triangular grid in the horizontal dimension, the model has good ability when dealing with complex geometry in the coastal zone. Coastal structures such as breakwaters, groynes and jetties are well represented in the domain without affecting numerical accuracy. In order to solve the governing equations which involved surface gravity waves, time splitting technique is adopted to accommodate different time step. In this scheme, the solution is decomposed into external and internal modes which responsible to calculate current in two- and three-dimension, respectively (Chen et al. [43]).

The governing equations for the hydrodynamic circulation are based on a σ -coordinate system which has been discussed in detail by Blumberg and Mellor [45]. This system gives smooth representation of bathymetry as the transformation of Cartesian coordinate z , bottom topography $H(x, z)$ and surface elevation ζ which illustrated in Figure 3.1. Total water depth is described as $D_w = H + \zeta$.

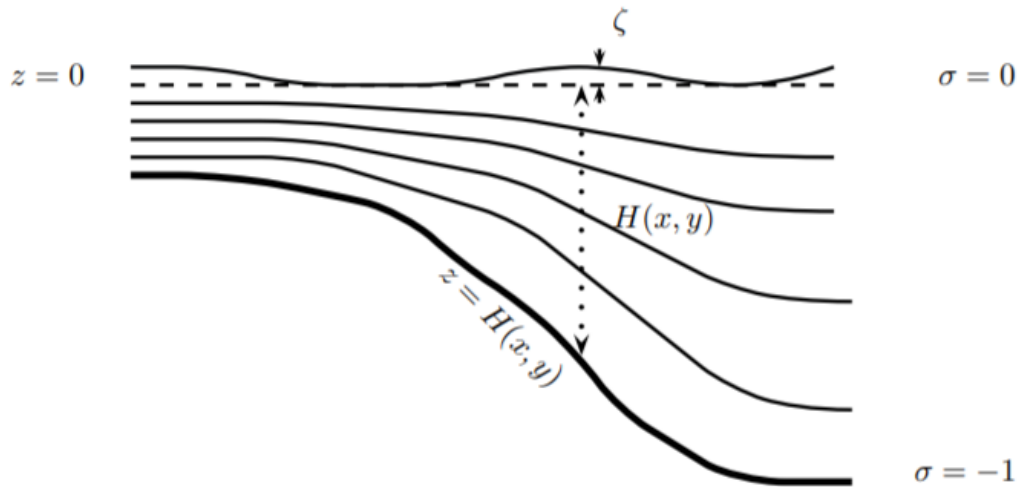


Figure 3.1: Illustration of σ -coordinate system in the model. Figure is reproduced from Morales Marín [71].

By adopting the vector form for the sake of simplicity and neglecting Coriolis, snow and ice terms, the governing equations are defined in Cartesian coordinate as continuity (Equation 3.1), pressure (Equation 3.2), momentum (Equation 3.3) and scalar transport equations (Equation 3.4):

$$\nabla_{\perp} \cdot \mathbf{V} + \frac{\partial w}{\partial z} = 0 \quad (3.1)$$

$$\frac{\partial \phi}{\partial z} + \frac{g\rho}{\rho_0} = 0 \quad (3.2)$$

$$\frac{\partial \mathbf{V}}{\partial t} + (\mathbf{V} \cdot \nabla_{\perp}) \mathbf{V} + w \frac{\partial \mathbf{V}}{\partial z} + \nabla_{\perp} \phi = \mathbf{F} + \frac{\partial}{\partial z} \left(K_m \frac{\partial \mathbf{V}}{\partial z} + \nu \frac{\partial \mathbf{V}}{\partial z} \right) \quad (3.3)$$

$$\frac{\partial C}{\partial t} + (\mathbf{V} \cdot \nabla_{\perp}) C + w \frac{\partial C}{\partial z} - \frac{\partial}{\partial z} \left(K_h \frac{\partial C}{\partial z} \right) - F_C = C_{source} \quad (3.4)$$

Boldface typeset represents vectors in horizontal space (x, y) while normal typeset is used for vertical component (w) . 3D vectors take form of (**horizontal**, vertical). (\mathbf{V}, w) is velocity components in Cartesian coordinate; ϕ is the dynamic pressure which normalised by density (ρ_0) ; ν is molecular diffusivity and \mathbf{F} is horizontal diffusion term; ρ and ρ_0 are total and reference sea water densities; C and C_{source} represent tracer quantity (e.g. salinity, temperature) and tracer source/sink term, respectively; K_m and K_h are defined as vertical eddy viscosity coefficient and thermal vertical eddy diffusion coefficient.

The surface and boundary conditions for (\mathbf{V}, w) are represented by:

$$\underbrace{K_m \left(\frac{\partial \mathbf{V}}{\partial z} \right)}_{z=\zeta(x,y,t)} = \frac{1}{\rho_0} \tau_{surf}, \quad w = \underbrace{\frac{\partial \zeta}{\partial t} + \mathbf{V} \cdot \nabla_{\perp} \zeta + \frac{E - P}{\rho}}_{z=\zeta(x,y,t)} \quad (3.5)$$

$$\underbrace{K_m \left(\frac{\partial \mathbf{V}}{\partial z} \right)}_{z=-H(x,y)} = \frac{1}{\rho_0} \tau_{bot}, \quad w = \underbrace{-\mathbf{V} \cdot \nabla_{\perp} H}_{z=-H(x,y)} \quad (3.6)$$

τ_{surf} and τ_{bot} are surface wind and bottom stresses, respectively, which defined as $\tau_{surf}, \tau_{bot} = \rho_0 C_d |\mathbf{V}| \mathbf{V}$; The drag coefficient C_d is obtained by determining a logarithmic the bottom boundary layer to the model at z_{ab} height above the bottom.

$$C_d = \max \left(\frac{\kappa}{\ln^2 \left(\frac{z_{ab}}{z_0} \right)}, 0.0025 \right) \quad (3.7)$$

where $\kappa = 0.4$ is von Karman constant, z_0 is the bottom roughness parameter. z_{ab} is equivalent to the half of the first grid above the bottom.

3.1.3 Sediment Transport Module

A sediment module in FVCOM is based on the Community Model for Coastal Sediment Transport (CMCST) which included suspended and bedload transport, layered bed dynamic based on the active layer concept, flux-limited solution of sediment setting, unlimited number of sediment classes and bed layers and cohesive sediment erosion/deposition

algorithms. A similar implementation to the CMCST in the Regional Ocean Modelling Systems (ROMS) is adopted with the major effort was to convert the structured-grid ROMS code to the unstructured FVCOM code by using mass conservative finite-volume approach.

Suspended Sediment Transport Module

The suspended module is developed by solving advection-diffusion equation with an additional source/sink term is added to the vertical settling and exchange with the bed (Warner et al. [49]).

$$\frac{\partial C^i}{\partial t} + (\mathbf{V} \cdot \nabla_{\perp})C^i + w \frac{\partial C^i}{\partial z} - \frac{\partial}{\partial z} (K_h \frac{\partial C^i}{\partial z}) - F_{C^i} = C_{source}^i \quad (3.8)$$

i is an index for sediment class; C^i represents sediment concentration of the i -th sediment class; K_h is the vertical eddy viscosity; F_{C^i} represents horizontal diffusion of sediment concentration; C_{source}^i is sediment source of i -th sediment class. It contains the settling process and sediment exchange between sediment at the bed and at the water column.

$$C_{source}^i = -\frac{\partial w_s^i C^i}{\partial z} + E_s^i \quad (3.9)$$

where w_s^i represents sediment settling velocity of i -th sediment class. The erosion source, E_s^i is parametrised following Ariathurai and Arulanandan [72] erosion rate.

$$E_s^i = E_0^i (1 - P_{bs}) F_{bs}^i \left(\frac{\tau_{sf}}{\tau_{ce}^i} - 1 \right), \tau_{sf} > \tau_{ce}^i \quad (3.10)$$

where E_s^i is the surface erosion mass flux ($kgm^{-2}s^{-1}$); P_{bs} represents the porosity of the top bed layer, E_0^i is the bed erodibility constant ($kgm^{-2}s^{-1}$); F_{bs}^i is the fraction of i -th sediment class in the bottom; τ_{sf} is the bottom shear stress and τ_{ce} is defined as the critical erosion stress for the i -th sediment class. Sediment mass transport from the top layer of the bed is limited to the mass available in the top layer. At the erosion phase, the top layer thickness is increased to meet the active layer thickness. In contrast, new layer is resulted at the deposition stage if the timing and thickness criteria are met. Despite these processes, the total layers are maintained to be constant so that both merge and split of bottom cells are required.

Sediment entrainment exists when the local shear stress at the bottom reaches a critical user defined value and it is removed at a rate defined by user. According to Chen et al. [48], the simulated concentration profile depends on the net balance between advection, vertical diffusion, introduction of new material through erosion and the loss of material from the water column through the settling process. The settling term requires particular treatment due to the steep profile gradient near the bottom. Therefore, a piecewise parabolic method

(Colella and Woodward [73]) and a Weighted Essentially Non-Oscillatory (WENO) approach (Liu et al. [74]) are used in FVCOM.

To close the sediment module equation, zero-flux boundary conditions are imposed both on the surface ($z = \zeta$) and bottom ($z = -h$) in the vertical diffusion equation for sediment concentration.

$$K_h \frac{\partial C_i}{\partial z} = 0 \quad (3.11)$$

The sediment bed is initialised with a thickness, sediment-class distribution, porosity and age for each horizontal cell which represented by three-dimensional arrays with a user-specified, constant number of layers beneath each horizontal model cell(see Figure ??). Sediment mass of each class is obtained from the sediment bed properties and the grain density. Moreover, the sediment age property can be used to track the time that the deposition last occurred in that layer (Warner et al. [49]).

Bedload Sediment Transport Module

The model implements two methods for computing bedload transport: Meyer-Peter and Müller [75] formulation for unidirectional flows and Soulsby and Damgaard [76] that account for combined wave and current. The formula depends on its individual characteristic of each class, such as size D , density ρ_s , specific density in water $s = \rho/\rho_s$, and critical shear stress τ_c . In this section only the first method is described briefly, full discussion for both formulae can be found in Warner et al. [49].

Meyer-Peter and Muller bedload formulae Non-dimensional transport rates Φ for each sediment class are calculated by using

$$\Phi = \max [8(\theta_{sf} - \theta_c)^{1.5}, 0] \quad (3.12)$$

where $\theta_c = 0.047$ is the critical Shield parameter; θ_{sf} is the non-dimensional Shields parameter for skin stress and formulated as

$$\theta_{sf} = \frac{\tau_{sf}}{(s-1)gD_{50}} \quad (3.13)$$

in which τ_{sf} is the magnitude of total skin-friction component of bottom stress computed from

$$\tau_{sf} = \sqrt{\tau_{bx}^2 + \tau_{by}^2} \quad (3.14)$$

The skin-friction components of the bed stress, τ_{bx} and τ_{by} , are obtained from current itself or the maximum wave-current combined bed stress in the x and y directions. The bedload transport vector are divided as x and y components based on the magnitude of

the bed shear stress.

$$q_{blx} = q_{bl} \frac{\tau_{bx}}{\tau_{sf}}, \quad q_{bly} = q_{bl} \frac{\tau_{by}}{\tau_{sf}} \quad (3.15)$$

where q_{bl} represents bedload transport rates which calculated as

$$q_{bl} = \Phi \sqrt{(s-1)gD_{50}^3 \rho_s} \quad (3.16)$$

3.1.4 Bottom Boundary Layer Model

The subgrid-scale processes such as Reynold stresses, production and dissipation of turbulent kinetic energy, velocity and suspended sediment gradient vary in the vertical direction, especially near the bed. Moreover, resolving these features are difficult in the large scale models due to the massive computational cost issue. Therefore, an algorithm to parametrise some of these processes in the water column and bottom-boundary layer (**BBL**) is implemented in FVCOM.

The treatment for BBL is important for both circulation and sediment models in terms of:

- It determines the shear stress exerted from the bed into the flow. This stress denoted as τ_{tot} is used in the circulation model as a bottom boundary condition in the momentum equation.
- It calculates the bottom stress defined as (τ_{sed}). This stress is used in the sediment transport module to calculate both the bedload transport and pick-up function for sediment in suspension.

The above mentioned bottom stresses are different where τ_{tot} represents total bed shear stress due to the overall resistance from the flow (Soulsby [77]) while τ_{sed} is only the part of τ_{tot} related to skin-friction.

FVCOM offers two different approaches for representing BBL processes, namely, simple drag-coefficient based on pure current influence on the flow and more complex formulation included wave-current interaction and movable bed. The first approach adopts equation 3.7 with constant (or possibly vary in space) bottom friction. Despite its simplicity, this approach unable to reproduce the effects of waves and sediment in the flow. Moreover, the presence of short oscillatory waves, introduced turbulence and generates large instantaneous shear stress. Therefore, more complex formulas adopted from Warner et al. [49] in ROMS are added and modified to match with FVCOM unstructured grid. Similar with ROMS, FVCOM offers three methods to accommodate wave-current interaction and movable sediment into bed dynamics. In this study the wave-current BBL model of Madsen [78] or that Styles and Glenn [79] together with Wiberg and Harris [80] movable bed

(ssw_{bbl}) formulas is used. Input parameters such as Eulerian velocities (u, v) at reference elevation z_r , wave orbital velocity magnitude u_b , wave propagation direction θ , wave period T , and bottom sediment characteristic are required in BBL module. These parameters are obtained from circulation and sediment model. More detailed information regarding other approaches are referred to Warner et al. [49].

3.2 New LES Concept

In this part a SGS model for coastal hydrodynamics application is developed. One of the most important aspects in coastal models is the existence of typically two length scales, namely horizontal and vertical scales. The horizontal dimension of order of kilometres and one for the vertical direction of orders of ten meters. This condition creates problem when a characteristic length scale is required. In addition, anisotropic cells with an aspect ratio between the horizontal and the vertical direction of 10:1 occur, in which produce inaccuracy when using classical sub-grid stresses. It is common to use the Deardroff equivalent length scale in LES, $\Delta_{eq} = (\Delta_1\Delta_2\Delta_3)^{1/3}$ where $\Delta_{1,2,3}$ represents the cell sides. Despite this concept is good for weakly anisotropic cell, Kaltenbach [81] explained that the implementation of this technique in coastal flow produced inaccuracy in the evaluation of turbulence statistics.

The anisotropic issue has been investigated by Scotti et al. [82] on the features of the Smagorinsky model with anisotropic grid in the inhomogeneous flow by using a single length scale model. However, the requirement of a single length scale in strongly anisotropy grid results a problem. Zahrai et al. [83] proposed a model with different length-scale to face the anisotropy problem. To take into account the anisotropy issue in coastal models, Roman et al. [17] modified Zahrai's concept to justify only highly anisotropic filter cells where the use of an unique characteristic length scale is no longer pertinent (Sagaut [84]). In their formulation, the LES explicit filtering procedure is divided for horizontal and vertical directions to give a freedom used different scale. We extends Roman's concept by combining the ASM with mode-splitting procedure in Zheng et al. [18] model as a way to implement the model to the large scale simulation.

3.2.1 LES filtered governing equations

Following Rodi et al. [67] velocities and scalars in the governing equations are decomposed as resolved and unresolved parts. The former term represents high-containing energy and directly resolved by mesh size. It extracts the energy from mean flow and transfer it to smaller scales. Quantities with size bigger than the mesh are modelled and classified as the unresolved turbulent. For the sake of completeness we have rewritten Equation. 2.1

in the form of velocity.

$$u = \bar{u} + u' \quad (3.17)$$

Applying Equation 3.17 into continuity, momentum and scalar equations obtains filtered form of LES governing equations: filtered continuity equation

$$\frac{\partial \bar{u}_i}{\partial x_i} = 0 \quad (3.18)$$

filtered Navier-Stokes equations

$$\frac{\partial \bar{u}_i}{\partial t} + \frac{\partial \bar{u}_i \bar{u}_j}{\partial x_j} = -\frac{1}{\rho_r} \frac{\partial \bar{p}}{\partial x_i} + \nu \frac{\partial^2 \bar{u}_i}{\partial x_j \partial x_j} - \frac{\partial \tau_{ij}}{\partial x_j} + g \frac{\bar{\rho} - \rho_r}{\rho_r} \quad (3.19)$$

filtered scalars transport equation:

$$\frac{\partial \bar{\phi}}{\partial t} + \frac{\partial \bar{u}_i \bar{\phi}}{\partial x_i} = \Gamma \frac{\partial^2 \bar{\phi}}{\partial x_i \partial x_i} + \frac{\partial q_i}{\partial x_i} + \bar{S}_\phi \quad (3.20)$$

The "-" notation denotes the filtered properties or quantities in the resolved scale. Rodi et al. [67] explained that the non-linear effect $u_i u_j$ in convective term contributes to the development of τ_{ij} in the Equation. 3.19. This term identified as Subgrid-scale (SGS) stress tensor is similar to Reynold stress in RANS. Despite the mathematical structure of the equations is identical with RANS, the physical meaning is slightly different. τ_{ij} in LES represents the effects of the unresolved, small-scale turbulence on the resolved velocity while it represents all turbulent fluctuations in RANS. The SGS stress tensor takes form of:

$$\tau_{ij} = \overline{u_i u_j} - \bar{u}_i \bar{u}_j \quad (3.21)$$

Clark et al. [85] introduced three physical terminologies in which arise from SGS stress tensor known as Leonard L_{ij} , Cross C_{ij} , and Reynold R_{ij} terms. Based on this study, the SGS stress tensor can be written as:

$$\tau_{ij} = \overline{u_i u_j} - \bar{u}_i \bar{u}_j = \underbrace{\overline{u_i u_j} - \bar{u}_i \bar{u}_j}_{L_{ij}} + \underbrace{\overline{u_i u'_j} + \overline{u'_i u_j}}_{C_{ij}} + \underbrace{\overline{u'_i u'_j}}_{R_{ij}} \quad (3.22)$$

L_{ij} represents the interaction in resolving scale. Moreover, this term can be solved directly from the filtered flow field without modelling because the properties in this term are obtained from resolved part. In contrast to the Leonard stress term, the Reynold stress term, R_{ij} , expresses the interaction between unresolved scale. Modelling approach is needed to calculate this term. The interaction between resolved and unresolved scale is obtained by calculating Cross term C_{ij} . Both L_{ij} and C_{ij} are equal in LES while these terms are zero in RANS (Argyropoulos and Markatos [86]). There is a lot of study

have been proposed for modelling SGS stress tensor. The popular one is based on the eddy viscosity model. Furthermore, the idea behind this model is delivering energy from resolved to unresolved scale through inertial subrange. Due to the simplicity, Smagorinsky Model (SM) (Smagorinsky [3]) is commonly used in LES. This procedure is adopted from the viscous stress in laminar flows and the SGS stress is approximated by using the rate of strain tensor and depends on velocity gradients. The SGS stress in SM is expressed as:

$$\tau_{SGS,ij} = -2\nu_t \bar{S}_{ij} \quad (3.23)$$

ν_t is eddy viscosity and \bar{S}_{ij} defined as:

$$\bar{S}_{ij} = \frac{1}{2} \left(\frac{\partial \bar{u}_i}{\partial x_j} + \frac{\partial \bar{u}_j}{\partial x_i} \right) \quad (3.24)$$

3.2.2 Subgrid viscosity

The modelling effort in eddy viscosity concept is on determination of eddy viscosity ν_t where eddy viscosity is determined by the characteristic length scale and velocity scale. Representing characteristic length scale in the LES is done by filter size Δ and Smagorinsky constant C_s . Practically, Δ is the size of the grid space in the model, meanwhile C_s is tuned parameter. Thus the length scale is expressed as:

$$l = C_s \Delta \quad (3.25)$$

Following Prandtl's mixing length theory, the velocity scale can be defined as:

$$q = l \bullet |S_{ij}| = C_s \Delta \bullet \sqrt{2\bar{S}_{ij}\bar{S}_{ij}} \quad (3.26)$$

using Equation 3.26, the eddy viscosity is expressed as:

$$\nu_t = l \bullet q = l^2 |\bar{S}_{ij}| = (C_s \Delta)^2 \sqrt{2\bar{S}_{ij}\bar{S}_{ij}} \quad (3.27)$$

Zheng et al. [18] model, which is based on the FVCOM, is a RANS based model. Applying LES concept is commenced by applying the filtering procedure to the momentum and continuity equations. Lesieur [87] explained that the filtering procedure should be commuted and stressed to choose the best filter for solving small scale processes. Technically, the filtering procedure that is conducted through the size of the mesh also known as implicit filtering (Denaro [88]; Sagaut [84]; and Lesieur [87]).

It is very common in three-dimensional models to adopt two different types of eddy coefficients to model the motion in the horizontal and vertical direction due to the difference in the scale. The horizontal eddy coefficient is used for modelling the horizontal mixing

process with respect to the quasi-2D turbulence while the vertical mixing is resolved by the vertical eddy term. Such procedure that is adopting Smagorinsky [3] SGS model modified by Madsen et al. [89] has been adopted to calculate horizontal eddy coefficient by the following equation.

$$\nu_{sgs} = l^2 \cdot \left[\left(\frac{\partial u}{\partial x} \right)^2 + \left(\frac{\partial v}{\partial y} \right)^2 + \frac{1}{2} \left(\frac{\partial u}{\partial y} + \frac{\partial v}{\partial x} \right)^2 \right]^{\frac{1}{2}} \quad (3.28)$$

The formulation is based on the assumption that the turbulence is dissipated where it is produced, i.e. there is no advection of turbulence. Moreover, another assumption in which the turbulence transfer takes place in inertial subrange is used. When the turbulence at a certain location is affected by turbulence production from another point, the Smagorinsky [3] SGS model may not be valid.

Ramachandran et al. [90] stressed two important features of an SGS in coastal models as parametrisation procedure of the SGS fluxes and dissipation mechanism of the resolved scales. Moreover, the turbulence resides entirely on the subgrid scale in RANS concept without none of it resolved by the grid. In contrast, the increasing resolution of grid size in LES guarantees the abilities to solve viscosity and diffusivity terms in the coastal models. Due to its simplicity Smagorinsky [3] SGS model has been adapted for various 3D turbulence simulations, started by Lilly [91]. Lilly [91] tuned SM for homogeneous, isotropic turbulence by dumping the SGS dissipation to obtain the correct magnitude and slope of energy spectra within the initial sub-range. As a result, a well known Smagorinsky constant C_s is derived with the recommend value $C_s = 0.14$. However, this value is not valid for strongly anisotropic turbulence or coarse grid resolution case. By utilising the subgrid constant value as a function of space and time, two different filter lengths are adopted to resolve the large scale turbulence. This method, known as the Dynamic Smagorinsky Model (DSM), is proposed by Germano et al. [16] as the evaluation of constant SM coefficient. The DSM practically exhibits the negative eddy-viscosities which sometimes give rise into numerical instabilities and only transferred the energy from the resolved into unresolved turbulence part i.e. no backscatter energy transfer is allowed.

The dynamic model has shown satisfactory results in the prediction of a large scale flows with complex physics and geometry. For instance, Bou-Zeid et al. [92] overcame the problem of lacking of scale invariance between the SGS and the subtest stresses. Moreover, (Özgökmen et al. [93]; Özgökmen et al. [94]; and Tejada-Martí et al. [95]) confirmed the DSM ability for studying oceanic flows regarding the anisotropy grid issue. It is worth to note that the grid resolution in the DSM model should be placed in the inertial subrange where from computational point of views is highly demanding. Moreover, the subtest filter procedure extends time computation which sometimes very difficult to get the steady

condition.

By adopting similar idea where different characteristic of length scale is used to solve the anisotropy problem, Roman et al. [17] developed an ASM model that move back to the Smagorinsky model using different length-scales. This strategy is derived from the past works of (Kamenkovich [96]; Wajsowicz [97]; and Miles [98]). One of the ASM advantage is the freedom to choose grid resolution independently between the horizontal and vertical directions. Furthermore, ASM does not require the grid resolution to belong in the inertial subrange (Ramachandran et al. [90]).

ASM implementation in the Zheng et al. [18] model is started by modifying the diffusive term of Navier-Stokes equation to express the influence of two-eddy in the flow field. The diffusive term is defined as:

$$D_i = \frac{\partial}{\partial x_i} \nu_h \frac{\partial \bar{u}_i}{\partial x_i} + \frac{\partial}{\partial x_j} \nu_v \frac{\partial \bar{u}_i}{\partial x_j} \quad (3.29)$$

i in equation 3.29 represents the direction in horizontal scale while j describes the direction in the vertical scale. ν_v and ν_h denotes for the vertical and horizontal eddy, respectively. The dimensional eddy viscosity (ν_{ij}) is assumed to be symmetric, so that it reduces the six independent components to three: $\nu_{11} = \nu_{22} = \nu_{33}$, $\nu_{13} = \nu_{23}$ and ν_{33} . Sharing similar idea with SM, characteristic length scale for horizontal l_h and vertical l_v , can then be defined as:

$$l_h = C_h \Delta_h \quad (3.30)$$

$$l_v = C_v \Delta_v \quad (3.31)$$

Δ_h and Δ_v are proportional to the grid size in horizontal and vertical directions.

An improvement from Smagorinsky constant C_s , C_h and C_v can have different value. While this option is a better technique to solve anisotropy issue, the adjustment of these empirical constants produce uncertainty from model results. Petronio et al. [99] showed a procedure to get optimal value for C_h and C_v through the calibration process in elevated grid anisotropy ratio. Figure 3.2 described variation to get optimal value for C_h and C_v .

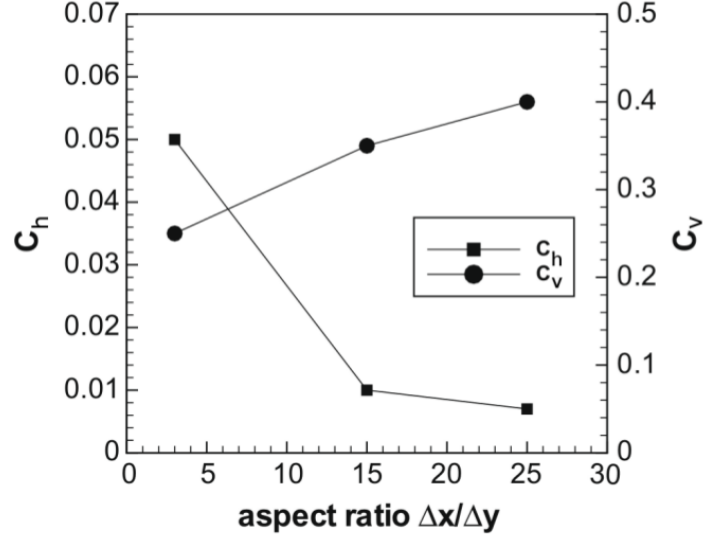


Figure 3.2: Optimal value variation for C_h and C_v (Petronio et al. [99])

To be consistent with length scale, the strain rate tensor is decomposed into \bar{S}_h and \bar{S}_v for determining velocity scale. In horizontal direction, \bar{S}_h is defined as:

$$|\bar{S}_h| = \sqrt{2\bar{S}_{ii}^2 + 2\bar{S}_{jj}^2 + 4\bar{S}_{ij}^2} \quad (3.32)$$

while in the vertical direction, \bar{S}_v is defined as:

$$|\bar{S}_v| = \sqrt{4\bar{S}_{ik}^2 + 2\bar{S}_{kk}^2 + 4\bar{S}_{jk}^2} \quad (3.33)$$

i, j, k stand for x, y, and z direction. Finally, the two-eddy coefficients can be arranged as:

$$\nu_h = (C_h l_h)^2 |\bar{S}_h| = (C_h \Delta_h)^2 \sqrt{2\bar{S}_{ii}^2 + 2\bar{S}_{jj}^2 + 4\bar{S}_{ij}^2} \quad (3.34)$$

$$\nu_v = (C_v l_v)^2 |\bar{S}_v| = (C_v \Delta_v)^2 \sqrt{4\bar{S}_{ik}^2 + 2\bar{S}_{kk}^2 + 4\bar{S}_{jk}^2} \quad (3.35)$$

The ASM sgs model is deployed in the present model to transfer turbulence energy from resolved to unresolved scale. As a consequence of mode split in the model, transferring TKE into unresolved scale is implemented in the similar way with the existing turbulence closure system in the model. The implementation of the ASM in horizontal diffusion can be classified as Horizontal Large Eddy Simulation (HLES) (Liek et al. [11]) or LES with depth averaging velocity.

3.3 Numerical schemes

The implementation of LES in the Zheng et al. [18] model is started by adding two-turbulence eddy viscosity terms in the internal and external modes. These new terms are required to transfer the turbulence energy from the large to the small scale motions. To accommodate the ASM concept in the present model, several new parameters are further defined in the main program. In this process original code is modified to account the shear stress term from the unresolved part.

3.3.1 Numerical algorithm

The complete step of ASM-LES implementation in the model can be seen in the Figure 3.3. Integration is carried out following the internal time step module. In this subroutine the hydrodynamic terms are calculated in both 2D and 3D ways. Moreover, the calculation of the advection and diffusion fluxes initially calculated in the 2D way via *Advave_edge_gcn* subroutine. The horizontal-LES eddy viscosity, *LES_Horz*, is then added in the subroutine to calculate the shear stress. The hydrodynamic variables are passed to the external mode and it is used to update depth, surface elevation and vertically averaged velocity fields from previous cycle.

The calculation of the 3D advection and horizontal diffusion terms are conducted in the *Advection_edge_gcn* subroutine by using the parameters from the external mode. The modified eddy viscosity based on the LES concept is implemented in this subroutine to replace the Smagorinsky viscosity coefficient and to calculate the flux in the x and y directions. The results from this process are the 3D hydrodynamic variables. In the next step, the all terms in the x - and y -momentum equations are solved except the vertical diffusion term. The calculation is carried out in the *Adv_uv_edge_gcn* subroutine by using 3D advection and diffusion fluxes. Following similar procedure in the *Advave_edge_gcn* subroutine, the *LES_Horz* is used to calculate turbulence viscosity and momentum fluxes at each σ level.

The vertical diffusion term is calculated by solving the tri-diagonal equation that is range from $k = 2$ to $KB-2$. KB is defined as the number of total σ -levels. This subroutine requires vertical eddy coefficient that is obtained from the calculation in the *LES_Vert* subroutine.

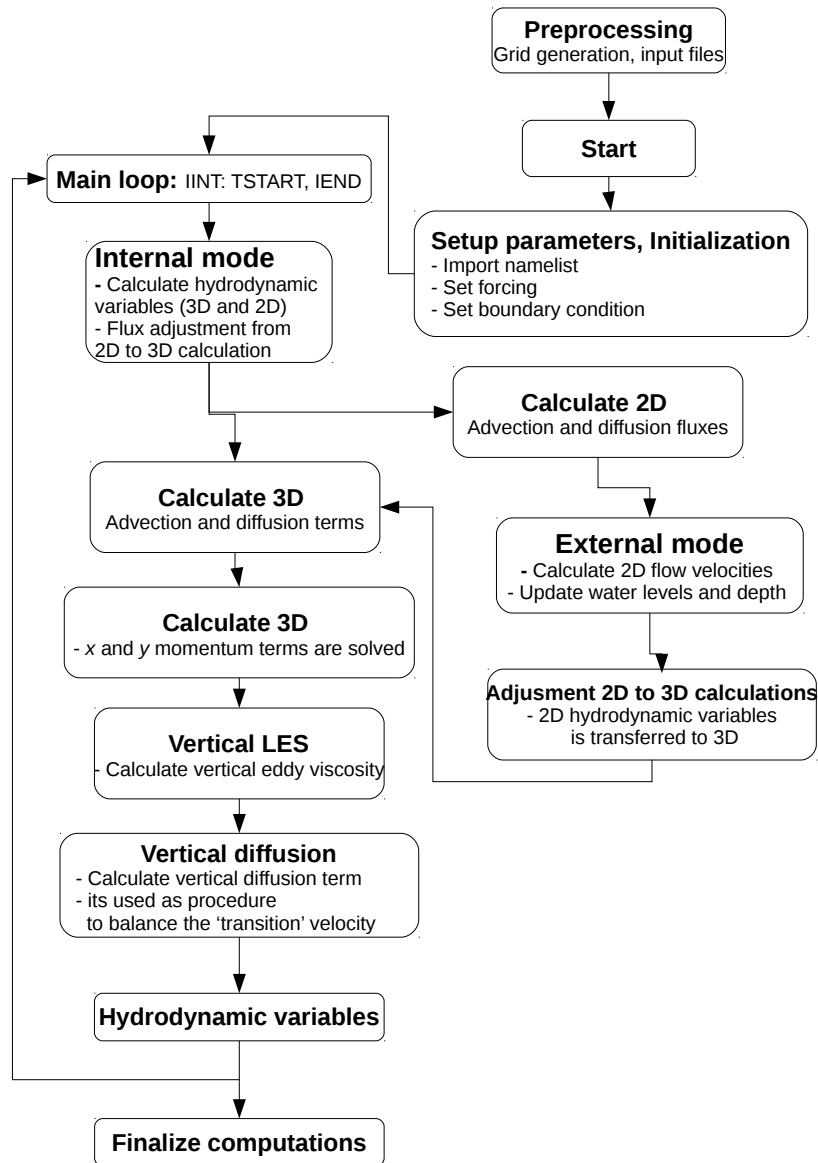


Figure 3.3: The flowchart of ASM-LES in the model.

3.4 Summary

This chapter explains the existing system of Zheng et al. [18] model, development of the new SGS model based on LES concept and the implementation into existing models.

A 3D, prognostic, unstructured-grid, finite volume based ocean model is modified to solve the vortical eddy structures in the main flow. This model uses non-overlapped, tri-

angular grid in the horizontal dimension and σ -coordinate system in the vertical direction. To speed up the computational time, the model adopts time splitting procedure, in which two different time steps can be used during simulation. In this scheme, the calculation is divided as external and internal modes that responsible to solve the governing equations in 2D and 3D, respectively.

In order to implement LES concept into the model, velocities and scalars are decomposed as resolved and unresolved parts. The procedure to separate these quantities is known as explicit filtering. The velocities and scalars larger than mesh size are categorized as resolved part while smaller properties are defined as unresolved part. Another important aspect in the LES implementation is the existence of typically two length scales, horizontal and vertical directions. To tackle this anisotropy problem, the ASM is used as SGS model. One of the ASM advantages is the freedom to choose different mesh size between the horizontal and vertical directions.

The implementation of LES into the model is conducted through modifying the diffusive term of the governing equations. In addition, to accommodate the new terms from LES several new parameters are then defined in the main program. The model integration is conducted inside the internal module. Firstly, 2D advection and diffusion fluxes are calculated together with the horizontal eddy viscosity of LES. Secondly, the variables from previous calculation are then transferred into external mode and used to update depth, surface elevation and vertically averaged velocity. In the next stage, 3D calculation of advection, horizontal diffusion and horizontal eddy are conducted. The results from this process are the 3D hydrodynamic variables. All terms in the x - and y - momentum equations are solved except the vertical diffusion. The vertical diffusion subroutine requires vertical eddy coefficient that is obtained from the calculation of the vertical LES. These terms are used to balance the transition velocity from the previous cycle.

Chapter 4

Model validation

In order to investigate model performance for modelling turbulent flows, a simple test for flow pass a cylinder is performed. Model results are compared with Roulund et al. [1] experiment for rough bed case. Flow dynamics, namely horseshoe vortex, flow separation and vortex-shedding are investigated in this section.

Firstly, the main flow features are presented, covers the effect of cylinder Reynold number on the main flows, the generation and dissipation mechanism of the vortex and previous numerical studies with respect to this case. Then, Roulund et al. [1] experiment is discussed including driving force, instruments and scenarios. In the last section of this chapter, numerical modelling set-up, input parameters and results are discussed. Model validation is conducted by comparing model outputs with Roulund et al. [1] experiment for rough bed case.

4.1 Flow pass a cylinder

Flow pass a cylinder is a classic case in turbulence flow study. It offers a simple geometry, but give rise to the complex processes in the flows for instance, horseshoe vortex, flow separation, vortex-shedding at the wake region and flows acceleration at the sides of the cylinder (Roulund et al. [1]). The flow pass a cylinder is characterised by complex interaction between distinct phenomena, namely boundary layers, separation and reattachment, shear layers and large two or three vortical structures. Generally speaking, it worth to note that this case is very sensitive to experimental condition such as aspect ratio, blockage, input or output boundary conditions and turbulence levels (Fröhlich et al. [100]). In addition, the dynamic changing depends on the cylinder Reynold number (Re) and formulated as

$$Re = \frac{DU}{\nu} \quad (4.1)$$

in which D is cylinder diameter; U is the mean upstream flow velocity; and ν is the kinematic viscosity. An increasing Re number destabilises the wake and shed-off the vortex-shedding. Furthermore, several distinct regimes have been identified as the Re increase. Roshko [101] determined laminar, steady and symmetrical flow at $Re < 40$. A regular and stable vortex street is obtained at $40 < Re < 150$ while the flow is entirely laminar. The transition from laminar to turbulence regime is discovered at $150 < Re < 300$ while $Re > 300$ showed the irregular range. At much higher Re (2×10^5 to 5×10^5), laminar separation is succeeded by transition to turbulence. Following this process, vortex formations develop on the downstream side of the cylinder together with the separation processes at the sides of the cylinder. Comprehensive representation is showed in Figure 4.1 (Sumer et al. [59, p. 2]) for flow around a smooth, circular cylinder in the steady current.



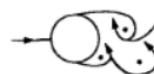
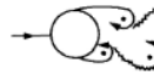





a)		No separation. Creeping flow	$Re < 5$
b)		A fixed pair of symmetric vortices	$5 < Re < 40$
c)		Laminar vortex street	$40 < Re < 200$
d)		Transition to turbulence in the wake	$200 < Re < 300$
e)		Wake completely turbulent. A: Laminar boundary layer separation	$300 < Re < 3 \times 10^5$ Subcritical
f)		A: Laminar boundary layer separation B: Turbulent boundary layer separation; but boundary layer laminar	$3 \times 10^5 < Re < 3.5 \times 10^5$ Critical (Lower transition)
g)		B: Turbulent boundary layer separation; the boundary layer partly laminar partly turbulent	$3.5 \times 10^5 < Re < 1.5 \times 10^6$ Supercritical
h)		C: Boundary layer com- pletely turbulent at one side	$1.5 \times 10^6 < Re < 4 \times 10^6$ Upper transition
i)		C: Boundary layer com- pletely turbulent at two sides	$4 \times 10^6 < Re$ Transcritical

Figure 4.1: Representation of flow regimes around circular cylinder (Sumer et al. [59, p. 2])

4.2 Roulund experiment

The model validation is achieved against Roulund et al. [1] experimental data. In their experiments, the measurement was conducted in a 28 m long and 4 m wide flume with 0.54 m water depth. The bottom of the flume is covered by a single layer of crushed stones with roughness height ($k = 7$ mm). The cylinder diameter was $D = 53.6$ cm with smooth surface and it was sealed along its perimeter at the bottom. Constant of a flow velocity $V = 32.6$ cm s^{-1} is specified from the input boundary.

Flow velocity and turbulence characteristics were measured in the plane of symmetry upstream and downstream of the cylinder by using a two-component DANTEC 'pen-size' Laser-Doppler Anemometer (LDA). Roulund et al. [1] experiments show complex flow fields around cylinder, such as horseshoe vortex, vortex stretching and flow separations. Full information regarding the test conditions can be found in the Table. 4.1.

Table 4.1: Test condition for the rough-bed experiment (modified from Roulund et al. [1])

Water depth h (cm)	54
Mean flow velocity V (cms^{-1})	32.6
Cylinder diameter D (cm)	53.6
$Re_{\delta,V} = \frac{V\delta}{\nu}$	1.8×10^3
$Re_{D,V} = \frac{VD}{\nu}$	1.7×10^3
$Fr = \frac{V}{gh^{0.5}}$	0.14
Bed roughness height k (cm)	0.7
Bed Nikuradse equivalent sand Roughness (k_s) (cm)	1.0

4.3 Model domain

Model domain is developed following Roulund et al. [1] with 50 m long and 4 m wide. A cylinder with diameter (D_c) 0.56 m is constructed 13 m from the inlet. Bottom condition is assumed flat with 0.54 m depth. The domain is illustrated by Figure 4.2.

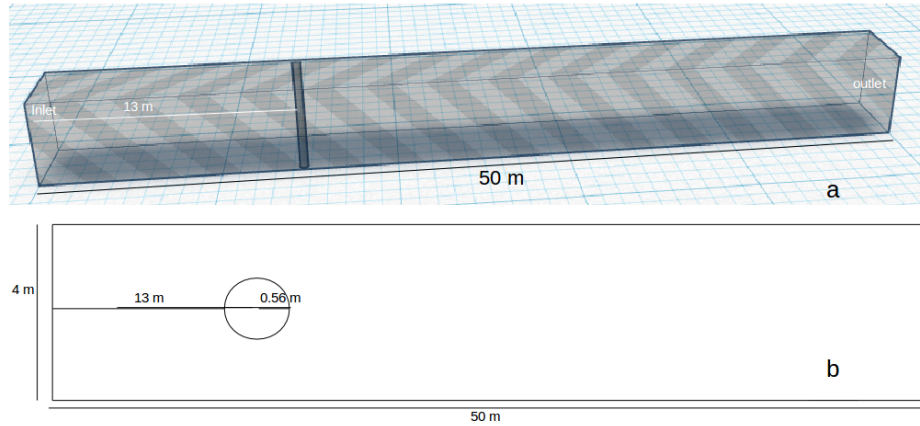


Figure 4.2: Model domain (a) three-dimension and (b) two-dimension.

4.3.1 Model boundary

Four boundary conditions, namely, the inlet, outlet, wall and bottom boundaries are implemented in this case. At the inlet and outlet boundaries, water levels are specified of 0.2 m and -0.2 m. This approach is used to obtain 0.46 m s^{-1} flow passing the inlet to the outlet. Flume sidewall and cylinder are defined as solid boundary with non-slip condition. Bottom condition is described as wall with 0.1 m roughness according to Roulund et al. [1].

4.3.2 Computational mesh

The computational domain is discretised into different size of triangular elements. For capturing flow behaviour, average mesh size is set to 0.02 m near the cylinder. Meanwhile, for the area more than 10 m away from cylinder, mesh size increases to 0.09 m. Total element in this simulation is 74053 triangular meshes. Figure 4.3 shows triangular meshes around a cylinder.

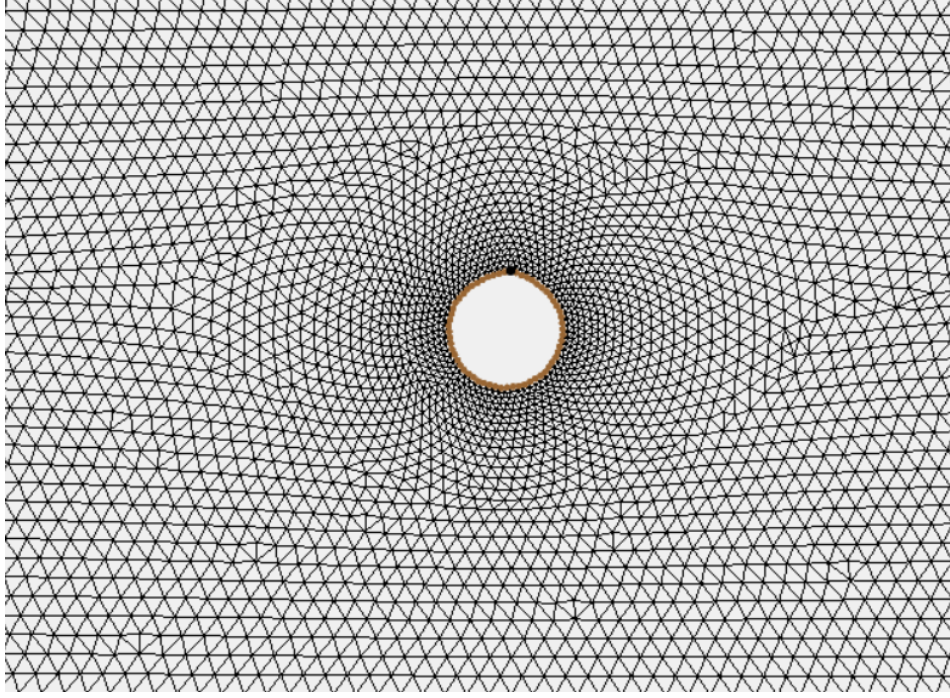


Figure 4.3: Triangular meshes around cylinder.

4.3.3 Numerical parameter

The numerical simulation is performed with 0.0001 s and 0.001 s time step for external and internal modes. In order to fulfil the stability criteria, The Courant number is maintained under 0.8 to satisfy the stability criteria and formulated as (Chen et al. [48]) :

$$\Delta t_E \leq \frac{\Delta L}{\sqrt{gD}} \quad (4.2)$$

where Δt_E is the external time step, ΔL is the shortest distance in a single mesh, and D is the local depth. The internal mode time step is defined by including the maximum phase speed of internal gravity waves C_I as:

$$\Delta t_I \leq \frac{\Delta L}{C_I} \quad (4.3)$$

In order to reach steady state condition, the simulation is run for 30 minutes and the last 120 s data are saved for analysis. Furthermore, the simulation is conducted in supercomputing cluster using 80 cores, over 32 hours.

4.4 Model results

4.4.1 Flow structures

The mean streamwise velocity is obtained from 100 s instantaneous data which is considered long enough to cover all different scales of motion in the channel. Here we defined the first step of 100 s instantaneous data as $t = 0$. It should be noted that the flows were dynamics due to the effects introduced by the SGS, which makes it is difficult to achieve steady state condition.

The time-averaged streamwise velocity is compared with experimental data from Roulund et al. [1] rough bed case for eight depths as shown in Figure 4.4.

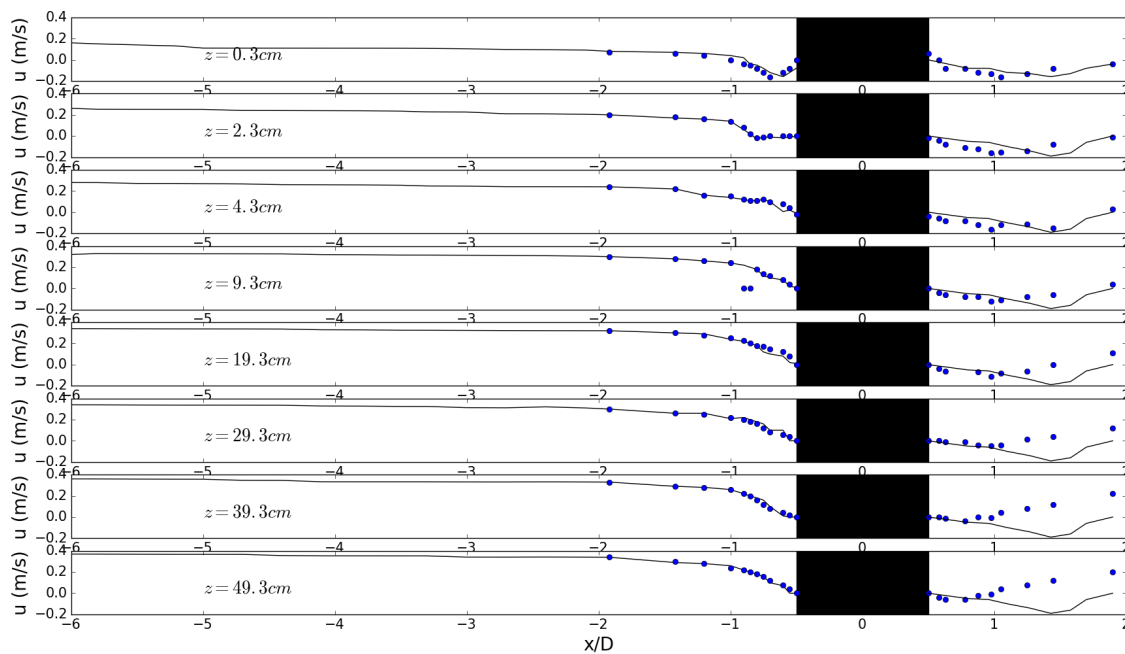


Figure 4.4: The mean streamwise velocity for eight depths from the model (solid line) and Roulund et al. [1] experiment (circle).

At the upstream part of the cylinder, the mean streamwise velocity is gradually decrease from 0.32 ms^{-1} at the inlet to around 0.2 ms^{-1} close to the cylinder. The computed results follow the measured data very well. Similar pattern is captured for eight depths at 0.003 m to 0.49 m from the surface. At the downstream side, the velocity initially decreases reached -0.2 ms^{-1} at $x/D = 1$ away from the cylinder before recovers the magnitude to approximately 0.2 ms^{-1} at 2 away from cylinder.

Comparison with the experimental data shows well agreement, particularly for the

upstream side of the cylinder. More importantly, the model is able to represent flow pattern from the experiment. However, some discrepancies are found at the downstream side where the model somehow under-predicted the velocity magnitude, particularly around $x/D = 1$ away from the cylinder at the lower level close to the bed surface. This difference suggests that the resolved eddy magnitude is over-predicted in the model close to the bed.

Similar with the streamwise velocity, the vertical velocity is compared with the rough case experiment for eight depths as shown by Fig. 4.5.

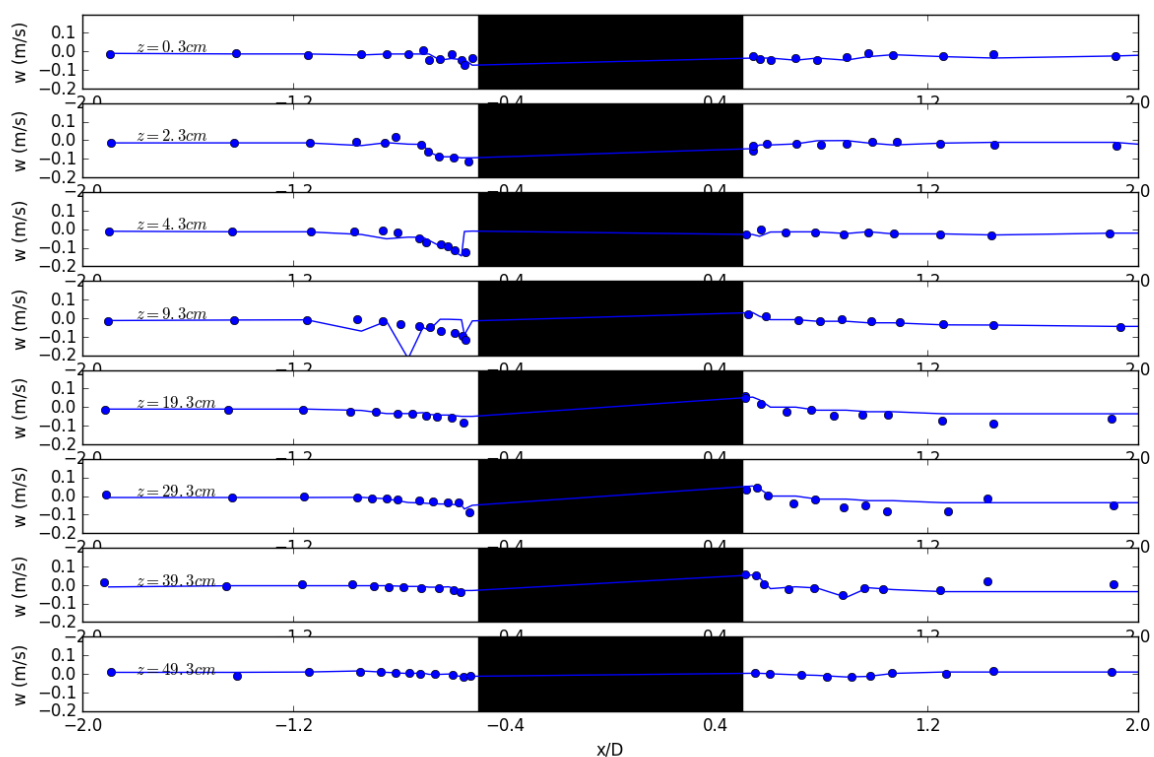


Figure 4.5: The mean vertical velocity for eight depths from the model (solid line) and Roulund et al. [1] experiment (circle).

At $x/D = -2$ upstream side, the velocity magnitude is regularly scale down from -0.01 ms^{-1} to -0.1 ms^{-1} at the side of cylinder. At the downstream part, the magnitude increases from -0.05 ms^{-1} at $x/D = 0.5$ from the cylinder to -0.02 ms^{-1} at $x/D = 2$ away from the cylinder. In contrast to the mean streamwise velocity where minor variations are found at the dowstream part, comparison with the experimental data for the mean vertical velocity shows excellent agreement. The model is able to capture the flow patterns as in the experiment for both upstream and downstream sides. The normalized root mean

square error of streamwise and vertical velocities is formulated as $NRMSE = \frac{RMSE}{u_{max}^* - u_{min}^*}$, in which

$$RMSE = \sqrt{\frac{\sum_{t=1}^T (u_t - u_t^*)^2}{T}} \quad (4.4)$$

where u_t , u_t^* , u_{max}^* and u_{min}^* are predicted velocity, measured velocity, maximum and minimum value of measured velocity, respectively. T is the frequency of the velocity. The calculated NRMSE of streamwise and vertical velocity are 11% and 8%, respectively.

To elaborate the flow dynamics for the whole water column, the velocity along the symmetric vertical cross-section is investigated and qualitatively compared with Roulund et al. [1] data as shown in the Figure 4.6 and 4.7.

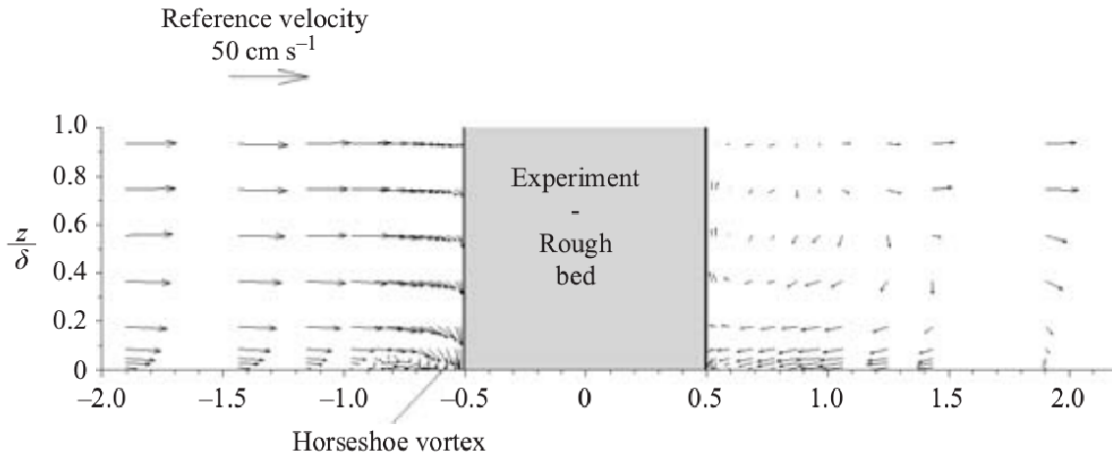


Figure 4.6: The vertical velocity profile from Roulund et al. [1] experiment.

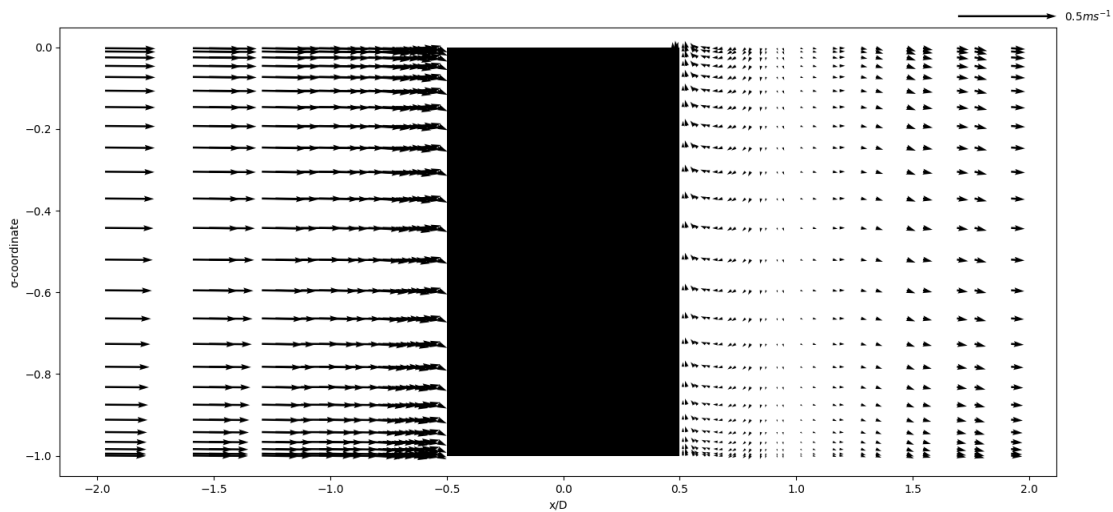


Figure 4.7: The vertical velocity profile at at $-2 \ll x/D \ll 2$ and $y/D = 0$.

Initially, the upstream flow follows logarithmic profile from the inlet until $x/D = -1$ from the cylinder. At a region $-1 \ll x/D \ll -0.5$, the flow starts to reduce the velocity and change its direction (see Fig. 4.7). As highlighted by Roulund et al. [1], this is a clear indication of horseshoe vortex formation in front of the cylinder. When the flow passes the cylinder, a clockwise vortex is formed attached to the cylinder side. According to Roulund et al. [1] this vortex is developed with respect to the roughness bed effect. In their findings, the roughness bed changes the vortex direction from anti-clockwise to be clockwise. Moreover, the existence of this vortex also has been reported by Yin et al. [102] and Aghaee and Hakimzadeh [103]. Despite the vertical profile from the model shows similar behaviour with the experiment, its magnitude is significantly weaker. This condition is caused by under-predicted vertical velocity at the downstream side of cylinder.

To gain more insight into vortex detail, the sequence of velocity vectors and streamline plots are represented in Figure. 4.8 - 4.11 .

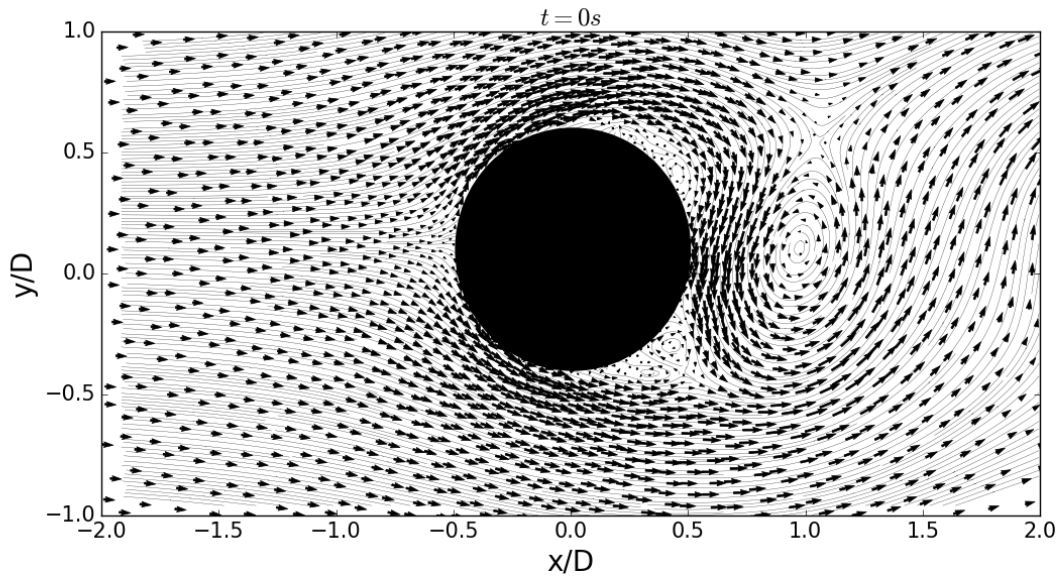


Figure 4.8: The horizontal velocity vectors and streamlines plot for $t = 0$ s at $\sigma/D = -0.50$.

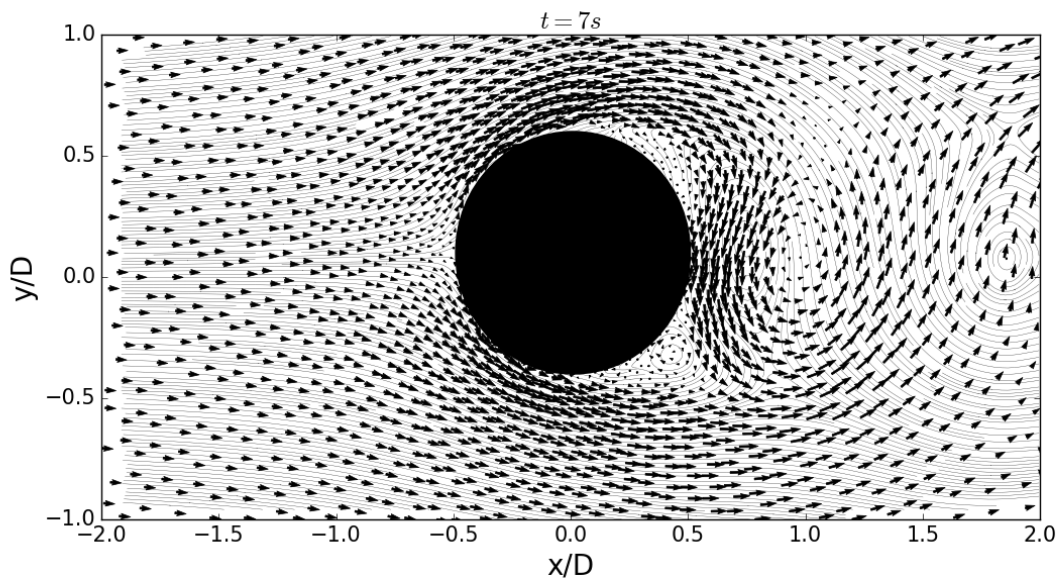


Figure 4.9: The horizontal velocity vectors and streamlines plot for $t = 7$ s at $\sigma/D = -0.50$.

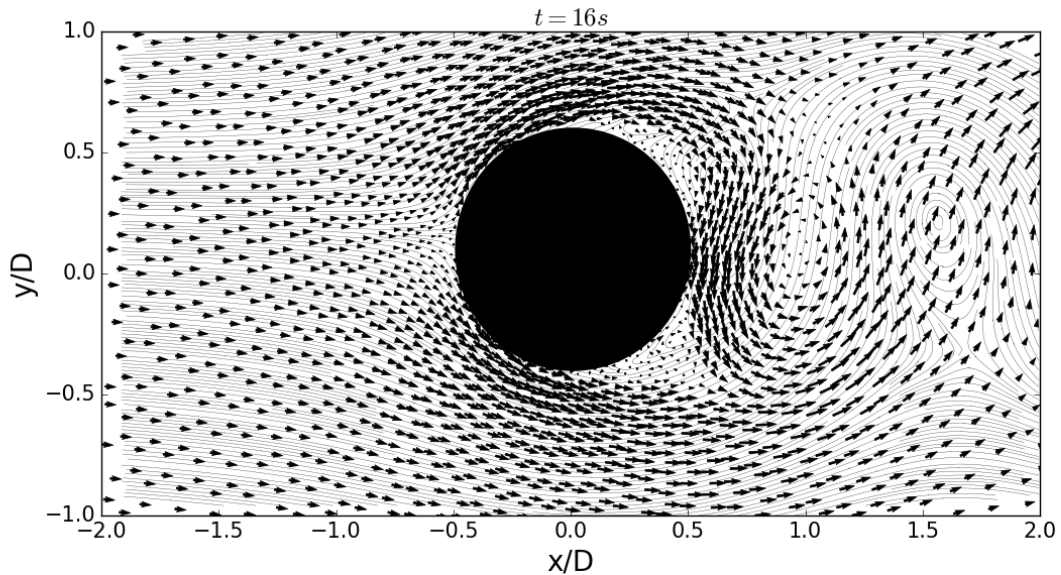


Figure 4.10: The horizontal velocity vectors and streamlines plot for $t = 16$ s at $\sigma/D = -0.50$.

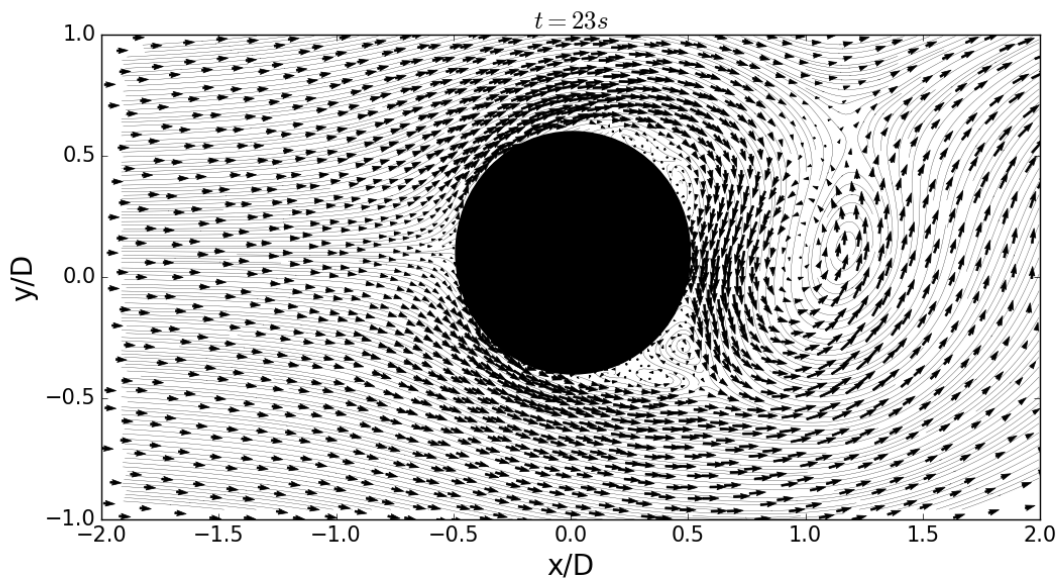


Figure 4.11: The horizontal velocity vectors and streamlines plot for $t = 0$ s at $\sigma/D = -0.50$.

As shown by Figure 4.8-4.11, the eddies detached from the sides of the cylinder. The unsteady behaviour of the vortices in which these eddies grow and move from one point to another is depicted by the model. Generally speaking, the shear layers emerging from the cylinder sides roll up to develop the eddies. According to Sumer et al. [59, p. 2] the eddies started to develop when the cylinder $Re_D > 40$.

The presence of eddy structures has significant role to the main flow dynamics. Fig. 4.12 shows the magnitude of instantaneous velocity at $\sigma = -0.05$, $\sigma = -0.25$, $\sigma = -0.50$ and $\sigma = -1.0$ layers, respectively. The flow patterns are similar for all layers where periodic lee-wake vortices are developed when the flow passes the cylinder. Despite the magnitude continuously decreases from the surface to the bottom, the vortices able to maintain its formation. Doron et al. [21] explained this behaviour as the characteristic of anisotropy turbulence or energy containing eddies.

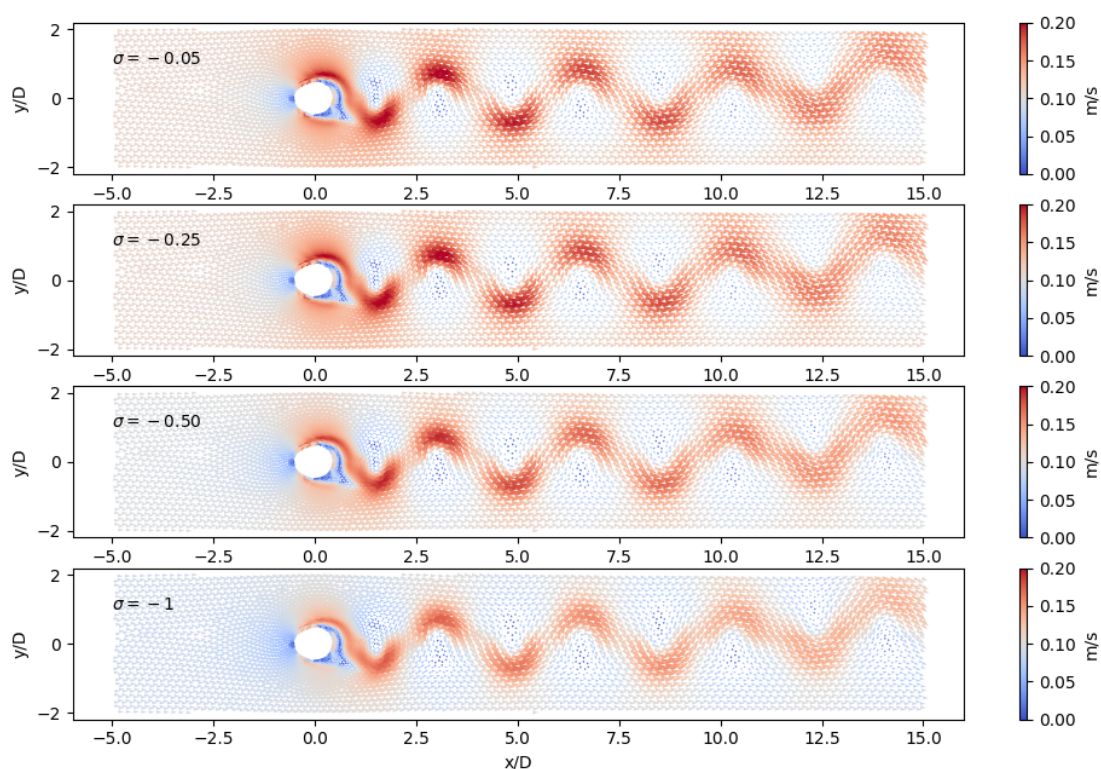


Figure 4.12: Horizontal velocity magnitudes for $\sigma = -0.05$, $\sigma = -0.25$, $\sigma = -0.50$ and $\sigma = -1.0$ layers.

The time evolution of the instantaneous streamwise velocity in 120 s period is used to estimated the shedding frequency. The data are extracted at $x/D = 1$ behind the cylinder. Strong fluctuating velocities can be seen in the Figure 4.13. By counting the peak of streamwise velocity under time-averaged velocity, the shedding frequency can be estimated. In this study, the shedding frequency obtained by the model is 0.10 Hz. The value is still in the range of Sumer et al. [59] diagram of Strouhal (S_t) against R_e number for corresponding input condition. The S_t is defined as $S_t = fD/U$, where D is cylinder

diameter and U is the mean flow velocity that can be used to identify the vortex shedding frequency, f . For $U = 0.32 \text{ m s}^{-1}$, $Re = 1.8 \times 10^3$, the S_t is in the range of 0.2 to 0.35, which leads to f in the range of 0.12 Hz and 0.21 Hz. Similar range of the vortex shedding frequency has been reported by Yin et al. [102] when simulating flow pass cylinder using 2eddy LES and WALE in the TELEMAC model.

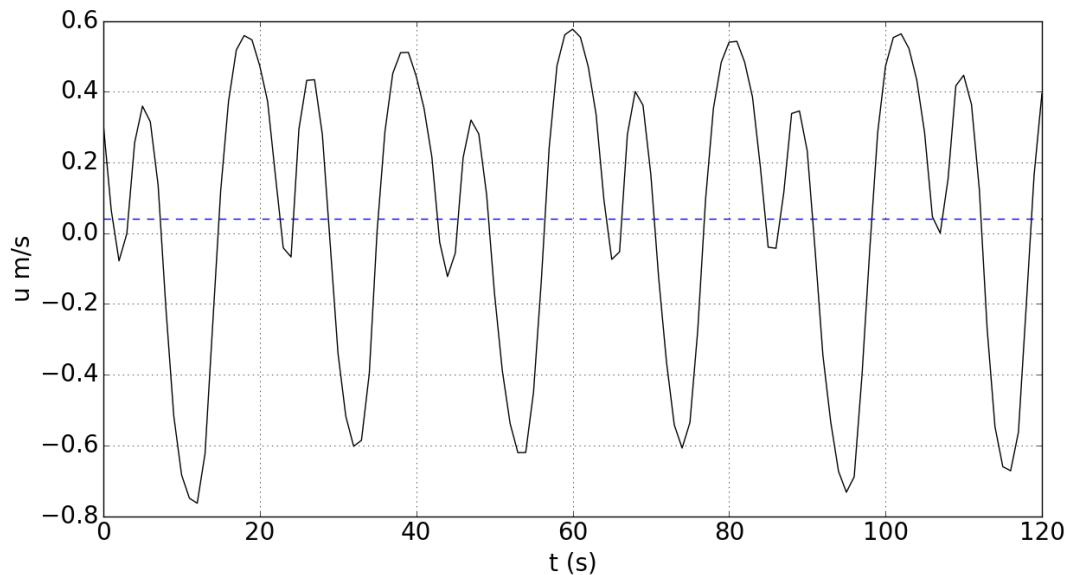


Figure 4.13: Instantaneous streamwise velocity in 120 s period obtained by the model.

4.5 Summary

The model has been tested to simulate flow over a cylinder for rough bed case. The NRMSE values indicated well performance of the model when compared with Roulund's rough bed case experiment. The model agree well with the experimental data for both streamwise and vertical velocities at the upstream side of the cylinder. However, discrepancies found at the downstream side where the model somehow underpredicted the velocity magnitude at $x/D > 1$ away from the cylinder. The horseshoe and clockwise vortices are captured by the model. The latter vortices arise due to the presence of roughness bed condition in the simulation. The model results indicated the unsteady behaviour of the eddies where it periodically grows and moves away from the cylinder. The lee-wake vortices show expected anisotropy feature where the vortex formations are remain stable from surface to the bottom layers. The shedding frequency obtained by the model is 0.10 Hz which is similar with Yin et al. [102] simulations.

Chapter 5

Flow over single groyne

5.1 Introduction

In order to investigate the model performance in resolving prototype scale coherent turbulence structures, a test case for flow over a single groyne is conducted. The case is used to demonstrate model capability for resolving the structure of the turbulent horseshoe (or necklace) type vortices induced by groyne structure at the upstream side, the recirculation region at the downstream side, the wake flow past the structure and the separated shear layer (SSL) arising from the tip of groyne.

Generally speaking, it has been widely known that when the flow approaches the structure, it experiences a strong transverse pressure gradient. This condition causes flow separation along the channel sidewall upstream of the groyne and leads to the formation of a recirculation region at the junction between the upstream face of the groyne and the side wall. At the junction between the downstream side and the side wall, another recirculation region exists (see in Fig. 5.1).

This case is similar to the simulation conducted by Liek et al. [11] using 2D Horizontal LES (2D-HLES) concept. However, the emphasis of Liek et al. [11] was to properly resolve the wake formations that shed from the groyne head without further accessed the main horseshoe vortex (HV) system and vortex tubes interaction inside the recirculation region. In contrast, the main vortical systems in the flow are investigated in this study.

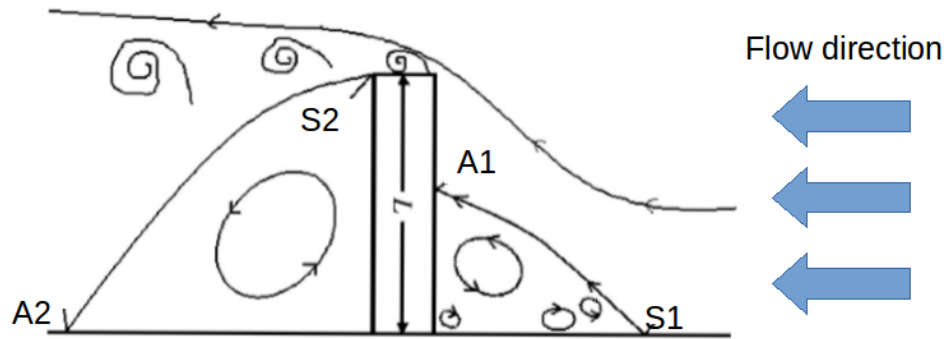


Figure 5.1: Schematic view of the flow over single groyne with both upstream (denoted by index S1 and A1) and downstream separation and reattachment points (S2 and A2). The figure is modified from Paik and Sotiropoulos [104].

5.2 Numerical simulation

Model domain covers about 300 m long and 60 m wide channel with 5 m constant depth where a 20 m long groyne is placed 120 m from the inlet. The 5 m, 2.5 m and 1 m horizontal mesh are generated and in the vertical direction 50 non-equally distributed sigma layers are used. The width of groyne in each simulation is 1 m as suggested by Liek et al. [11] to tackle the possibility that the differences in wide size give rise to the different simulation results. The simulation is very sensitive to the size of grids around the groyne as the mesh size directly affects the scale of the resolved and unresolved eddy motion. Therefore, the study is commenced by testing model sensitivity of three different mesh sizes, 1 m, 2.5 m and 5 m which represent $\Delta/L = 5/20$, $\Delta/L = 2.5/20$ and $\Delta/L = 1/20$, respectively. Figure 5.2 described three different mesh sizes used in the simulation. The total elements for 5 m, 2.5 m and 1 m mesh sizes are 12,345, 24,691, and 61,729 elements, respectively. As can be seen two open boundaries are placed in the East as the inflow and outflow boundary in the West. Constant flow velocity is specified at the inflow with varying surface elevation along the channel. Top and bottom boundary are treated as wall boundary. In this simulation, the fully developed condition is achieved after 01:23:00. The convergence time is defined as the time when the normalised root mean square error is less than 1.0%. More detailed input parameters can be found in Table 5.1.

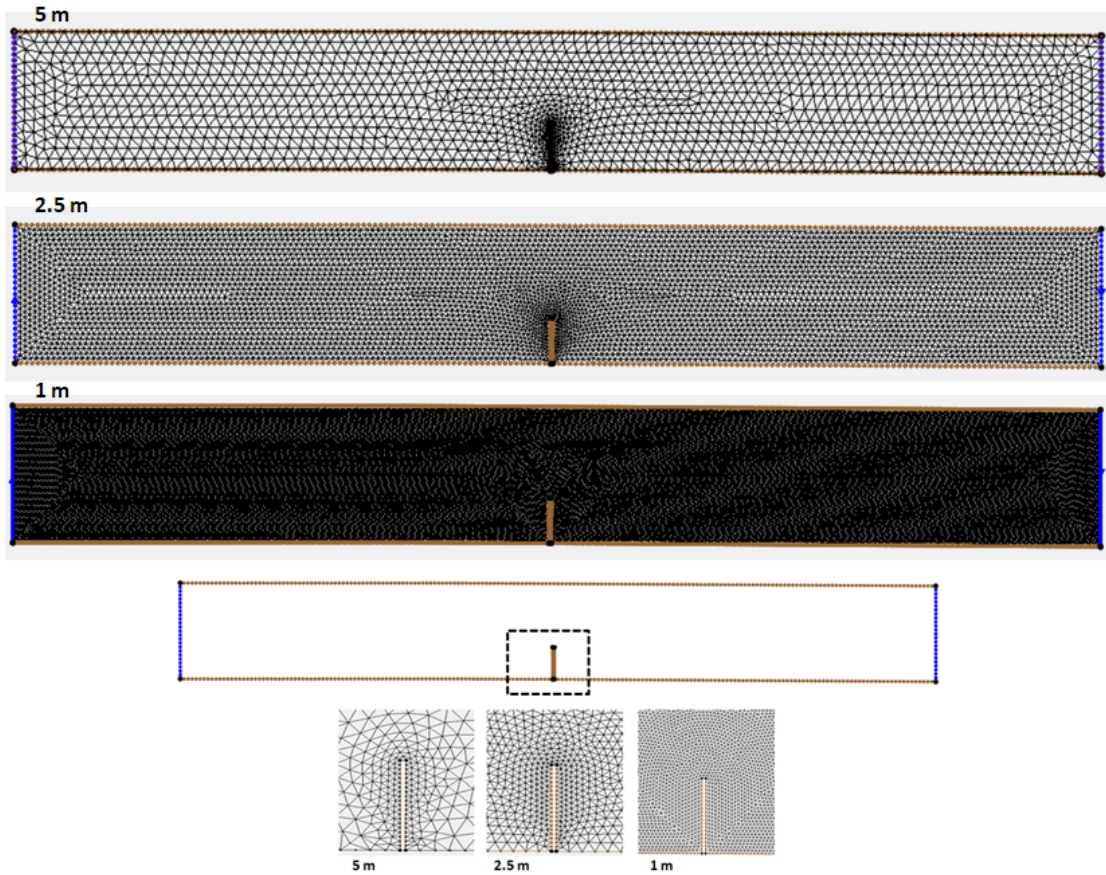


Figure 5.2: Triangular mesh of 5 m, 2.5 m and 1 m for the test-cases

Table 5.1: The input parameters for the flow over single groyne test

Parameters	Value	Units
Water depth h	5	m
Surface elevation at the inlet	0.4	m
Mean flow velocity V	0.4	(m s^{-1})
Bed roughness height k	0.1	cm
Flow simulation	5	hours
Computational time step	0.001	s
Output time step	1	s

5.3 Result and discussion

5.3.1 Mesh sensitivity

To identify whether the large horizontal eddies are well resolved in the simulations, flow velocity fields from three different mesh sizes are studied. Figure 5.3 shows the instantaneous flow velocity of three different mesh sizes at certain time after the fully developed condition is achieved. The plots clearly show that the computation with mesh size of $\Delta/L = 5/20$ and $\Delta/L = 2.5/20$ m do not resolve the vortex structures in the groyne head as well as the eddy formations in the downstream recirculation region. A different result is obtained for $\Delta/L = 1/20$ mesh in which the wake vortices emanating from the SSL is properly reproduced. Therefore, the simulation results for $\Delta/L = 1/20$ mesh are used for further analysis.

As can be seen, the intensified velocity magnitudes are observed around the core of vortex tubes. The small tube-like vortices develop due to the growth of Kelvin-Helmholtz instabilities and are shed from the tip of the groyne (McCoy et al. [105]). More than 0.85 ms^{-1} velocity magnitude is recorded in between these structures, which is more than two times higher than the inflow velocity magnitude. Furthermore, another amplified region is found at the downstream part of groyne corresponds to the descending eddy structure from the SSL.

From this work it is found that the presence of vortical structures evidently increases the velocity magnitude in certain areas. This result agrees with the previous finding from Kato et al. [106] that simulated flow over the breakwater head using LES. In their results the existence of eddy significantly elevated two to three times local flow magnitude. The eddy induced flow amplification indirectly confirms that the implementation of ASM as SGS closure system in the FVCOM works well to reproduce the turbulence coherent structure all different scales.

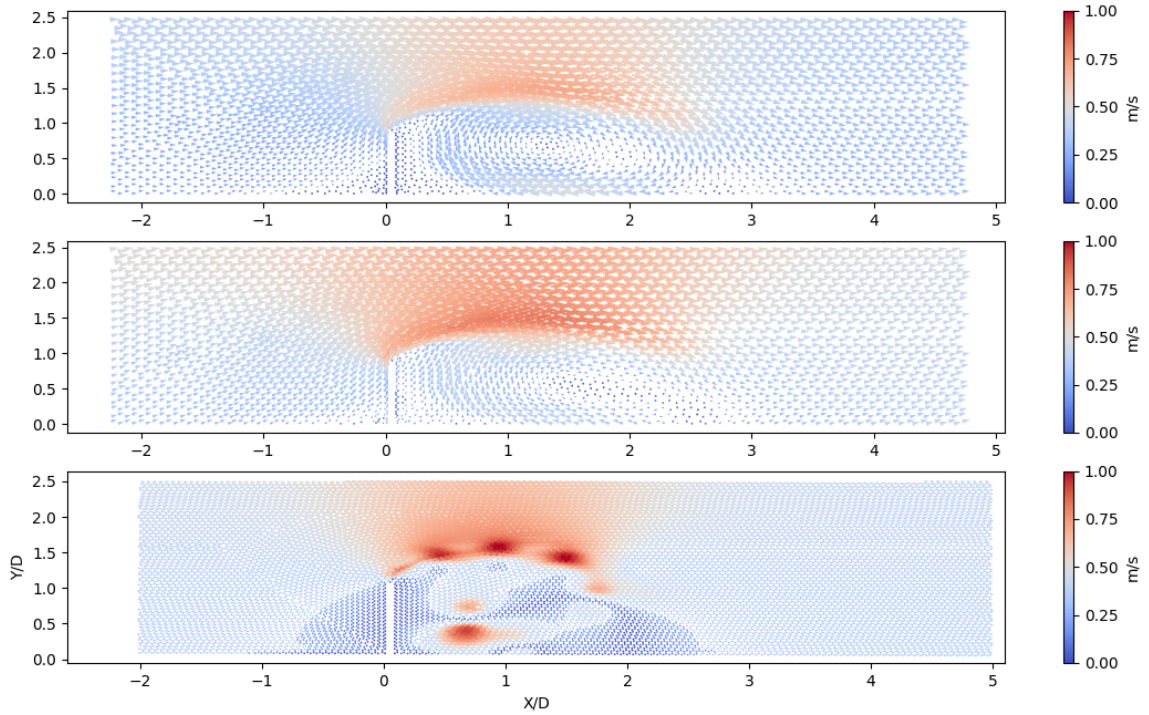


Figure 5.3: The instantaneous velocity magnitudes of 5 m, 2.5 m and 1 m triangular mesh size

In order to check if the calculations are numerically correct, the current magnitude of two monitoring points are extracted and compared with Liek et al. [11] simulation results. The location of the observation points used in this case is shown in the Figure 5.4.

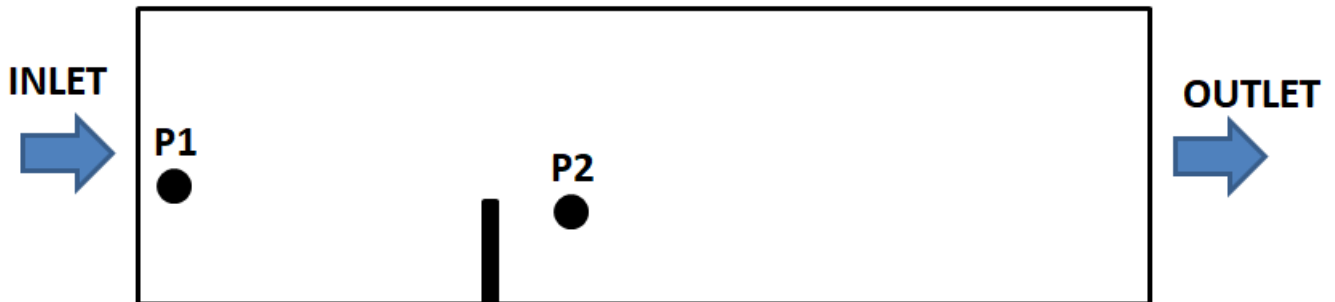


Figure 5.4: Location of the observation points

Three hours current magnitude is averaged every 60 s to make it comparable with the

Liek et al. [11] results. Initially, the current magnitude of the first monitoring point (P1) is unsteady due to the sudden introduction of the velocity to the model. After approximately one hour simulation time, the current magnitude starts to reach the constant value of 0.4 ms^{-1} . Comparison with the Liek et al. [11] simulation results obtains similar trends started with the spin-up time before reaching the steady value as shown in Figure 5.5a. However, small perturbations are recorded after 100 minutes as a result of ASM turbulent closure model in the simulation.

At the downstream side of the groyne (P2), a chaotic pattern of current magnitude is observed. The calculated values are in the range of $0.1 - 0.7 \text{ ms}^{-1}$. Despite the current magnitude ranges are in the same order with the Liek et al. [11] results, the patterns are different as shown in Figure 5.5b. The NRMSE value of the current magnitude is 22%.

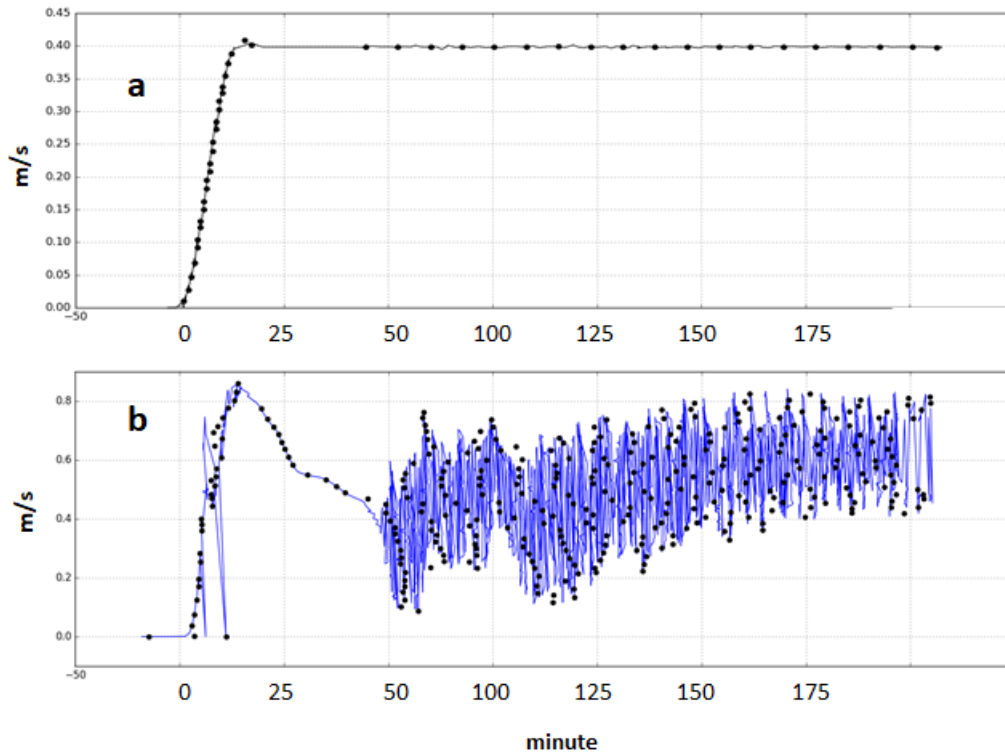


Figure 5.5: The simulated current magnitude of ASM model (line) and Liek et al. [11] model (circle) at the region close to the inlet (a) and downstream side of the groyne (b)

5.3.2 The vortical structures interaction

Before we proceed into detail of flow structures over single groyne, it is worthy to provide a global overview of the flow field as a starting point to understand broader scale phenomena. As mentioned in the introduction, there are two recirculating flow regions on the upstream and downstream side of the groyne. Each region has unique flow structures such as the

HV system at the upstream region, the SSL, vortex tubes/wakes shedding at recirculation region and the large coherent eddy formations that observed in the downstream part.

Figure 5.6 presents the initial stage of coherent structure generation that is started when the detached eddy shed off from the SSL until the structure moves back in the upstream direction. Each plot depicts the instantaneous condition for specific time to describe the main types of interaction between the detached eddy coming from the SSL and the vortex tubes. The later structures are convected over the tip of the obstruction and jittered by the detached eddy near the groyne head. Initially, both the eddy and vortex tubes move inline with the flow direction. However, after the new jittered vortex tube emerges the eddy is then forced to move downward in the upstream direction. During this period, the eddy is still able to maintain its form, reaching the tip of the groyne. A similar result has been reported by Koken and Constantinescu [107] when investigated separated shear layer and wake regions behind a vertical obstruction for high Reynold's number.

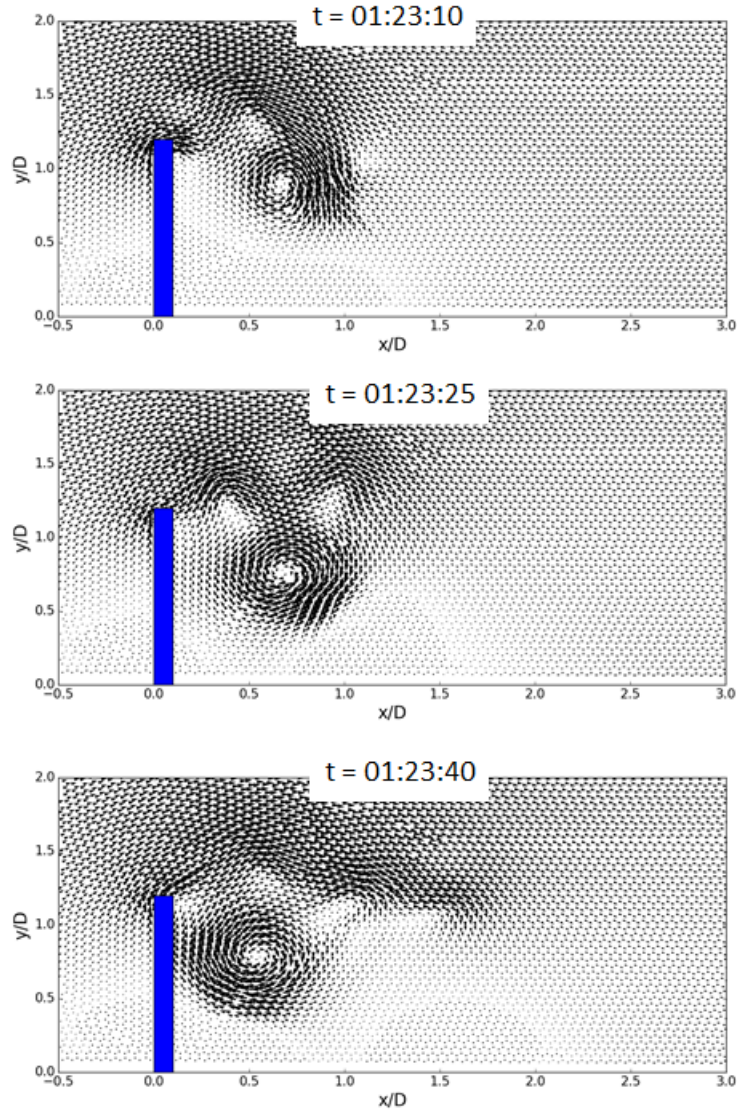


Figure 5.6: The evolution of vortical structures at $t = 01:23:10$ to $t = 01:23:40$.

The second stage is started when the eddy re-enters the SSL from the tip of groyne as shown in the Figure 5.7. Meanwhile, the vortex tube is convected downward at $X/D = 2$ forming new vortical structure near the sidewall. The new slow moving eddy attached to the side wall is fed by the detached eddy before merging to form larger structure. The primary eddy structure occupies more than 80% of the downstream recirculation area and the flow inside the core of this vortex moves in the upstream direction.

The all figures describe the complex vortex structures in the downstream region that is commenced by eddy generation at the tip of groyne, relatively high frequency flows into the shear layer. At the distance around $X/D = 2$ the vortex tubes turn over and generate large coherent structure attached to the side of the wall. From time to time, the vortex

grows and flows in the upstream direction before merging with the new emerge, dynamic eddy from the tip of the groyne.

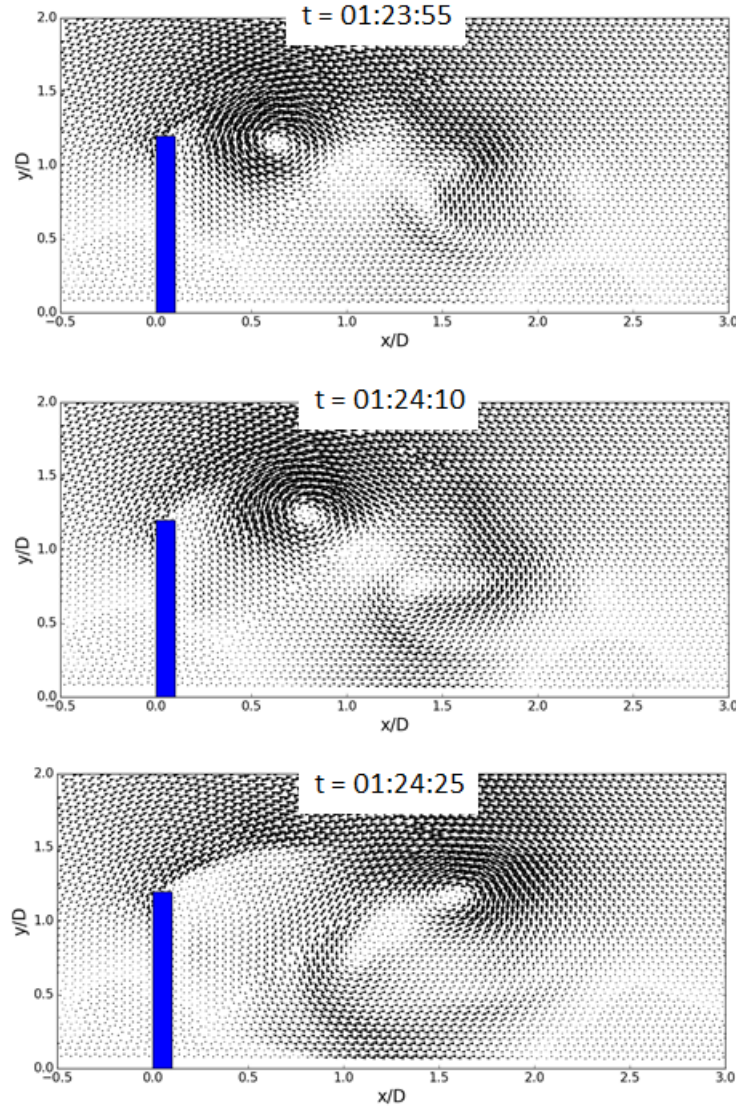


Figure 5.7: The evolution of vortical structures at $t = 01:23:55$ to $t = 01:24:25$.

5.3.3 The shear layer and recirculation region eddies

To illustrate eddy formations in the shear layer and recirculation area, the detailed mean velocity vectors that is generated by averaging the model results for 60 minutes simulation after steady condition and 2D streamlines are presented in the Figure 5.8. The figures distinctly present the existence of primary clockwise eddy inside the recirculation area and secondary anti-clockwise eddy at the downstream part. The primary eddy has length approximately three times of groyne length as a result of its interaction with flows from

the outer layer. The shape of this eddy varies over depth as it is sharper near the bed and larger in the upper regions. Investigation of this structure indicates that the vortex cores are not exactly vertical and the individual eddies do not extend regularly from the top to the bottom layers. As they move downstream, these eddies are stretched and in some points they merge to form a larger vortical structure.

Inside the primary eddy, there are two vortex cores merged at $X/D = 1.5$ (as shown in the right section of Figure 5.8). The first core which generated in the area close to the sidewall represents the interaction between the vortex tubes and outer shear layer. The velocity differences between the recirculating region and the shear layer force the new-developed large coherent eddy moves into the recirculation area. The second vortex core is produced from the interaction between the dynamic eddy attached to the downstream side of the groyne and the main necklace vortex in the shear separated layer.

The vector fields show large circular motions that span from $X/D = 0.5$ to $X/D = 2.5$ downstream the groyne. At the tip of groyne, maximum velocity magnitude is recorded with the direction is being parallel with the main flows. This is because of the strong local effect from the deflected HV system around the groyne head and the contribution of the vortex tubes that shed from the shear layer. McCoy et al. [105] have shown that the role of both vortexes as the driving force of fluid and momentum starting at the free surface into the main necklace of the HV.

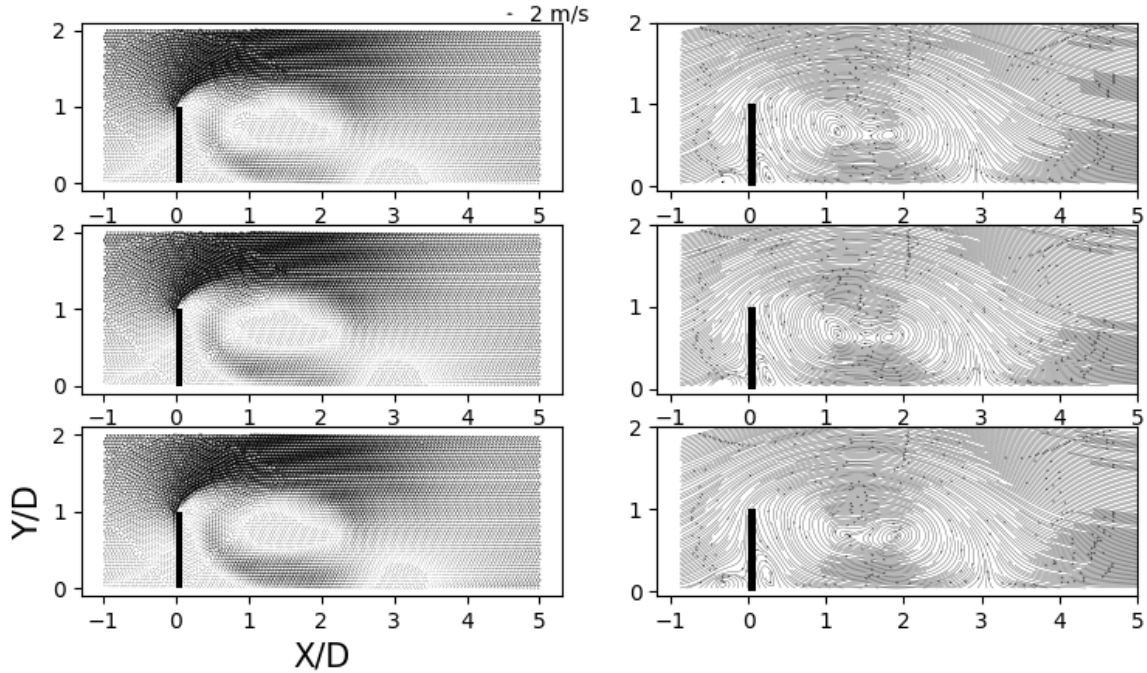


Figure 5.8: Mean flow features at three vertical layers, top) $H = -0.05$ m, middle) $H = -2.60$ m and top) $H = -4.90$ m

5.3.4 The transfers of turbulence energy

In order to understand the transfer of turbulence energy amongst the structures, the instantaneous value of resolved TKE and flow fields were extracted. The resolved TKE is defined as $TKE = \frac{1}{2}(u'^2 + v'^2 + w'^2)$. It can be seen in the Figure 5.9 that the eddies interaction contribute to change the TKE transfer process. The vortex tubes convected from the tip of the groyne can transport both high and low TKE depending on its sequence. For instance, The resolved TKE inside the vortexes indicates a pattern where a series of high and low TKE value emerged parallel with the vortex existence. In addition, the large primary eddy re-enters the recirculation region with upstream direction and merge with the vortex tube from the groyne tip. When these structures interacts, it also combines their energy.

Interestingly, the highest TKE value is found around the largest coherent eddy. In fact, the resolved TKE inside the large eddy are temporally high and sometimes lead to a local increase of the bed shear stress along its path (Koken and Constantinescu [108] and Mostafa et al. [109]). Paik and Sotiropoulos [104] highlighted that the flow inside this region is characterised as quasi-periodic flows. It is primarily dominated by multiple-slowly evolving, large scale eddies. In general, the instantaneous flow fields at the

downstream part indicate dynamic pattern affected by irregular vortex tube formations and large primary eddy.

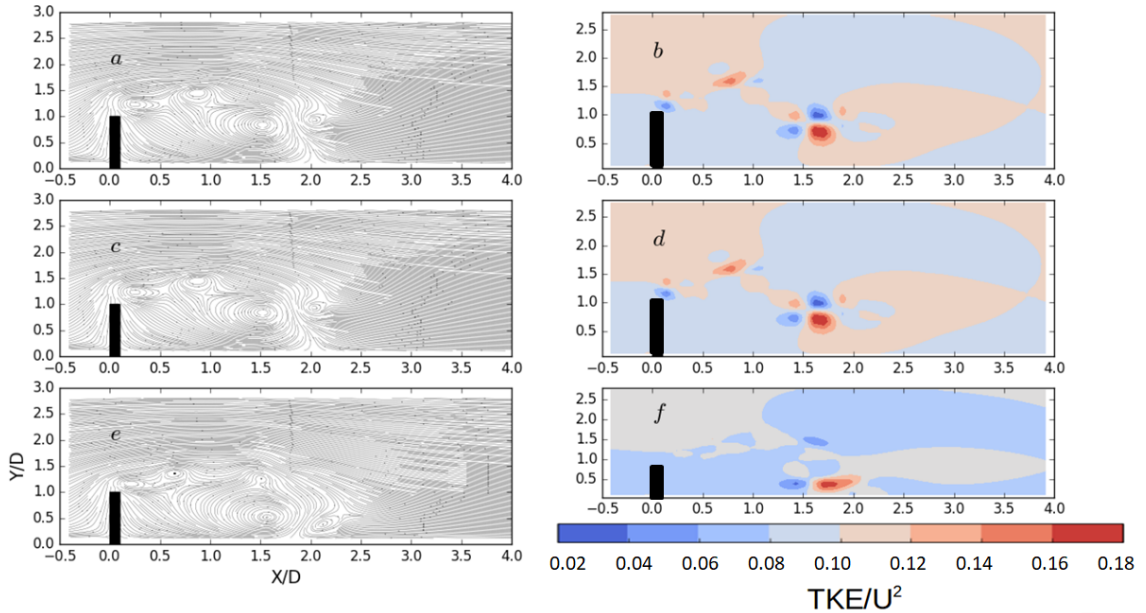


Figure 5.9: The instantaneous 2-D streamlines and resolved TKE for 5, 10 and 14 seconds.

Interesting result regarding turbulence energy distribution is obtained by using spectrum analysis of three observation points. The first location is positioned at the tip of groyne to capture the initial energy spectrum when the flow is deflected by the groyne. The second monitoring point is placed in the intensified velocity area. The reason is to investigate the effect of detached eddy presence in the turbulent dynamics. Furthermore, the location where the detached eddy is convected downward and forced to move in the upstream direction is used as the last monitoring point. The detail of the locations and energy spectrum are presented in Figure 5.10.

The spectrum energy is obtained from the time series value of streamwise velocity fluctuations. As can be seen all energy spectrums exist inside the inertial subrange with gradient -3. The highest energy level at the tip of groyne (#1) is around $10^{-6} E/Hz$ with most of the energy take place inside the high frequency. The interaction between vortex tube and detached eddy at $X/D = 1.2$ and $Y/D = 2$ increase the energy level significantly to about $10^{-2} E/Hz$ (#2). Furthermore, the interaction of the downward detached eddy with the side wall inside the recirculation region elevated the energy spectrum.

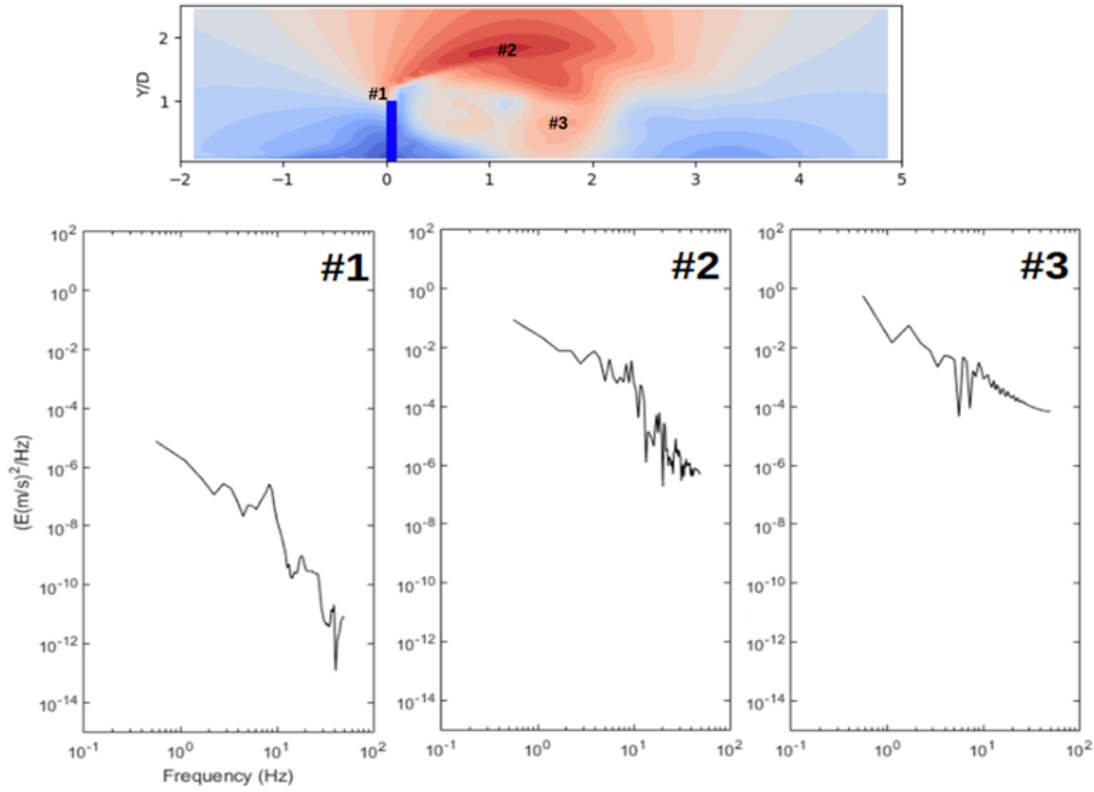


Figure 5.10: The monitoring points (top) in which colour indicating flow magnitude and energy spectrum of streamwise velocity fluctuations (bottom).

5.3.5 The vortical structures roles in the mean flow

To gain more insight of the vortical structures roles in the mean flow, the mean velocity magnitudes at three layers, near surface, middle layer and near bed are discussed and presented in the Figure 5.11. In the upstream part of the groyne, the flow velocity magnitude starts to decrease when approaching the groyne before then intensify around the tip of groyne as a result of groyne local effect with the maximum velocity adjacent to the outer layer of the shear layer. The velocity amplification, then moves along the flow and expands further downstream of the groyne. Experimental findings from Safarzadeh et al. [110] found that the extension of the high velocity field is of $1D$ to $2D$ for straight groyne case in which consistent with this simulation. Interestingly, the maximum velocity amplification, that defined as the ratio between the local maximum velocity magnitude and the velocity of the undisturbed approach flow, occurs adjacent to the outer layer of the shear layer. A similar result has been reported by Molinas et al. [111] that showed the depth averaged velocities around the vertical wall abutments increase 50%.

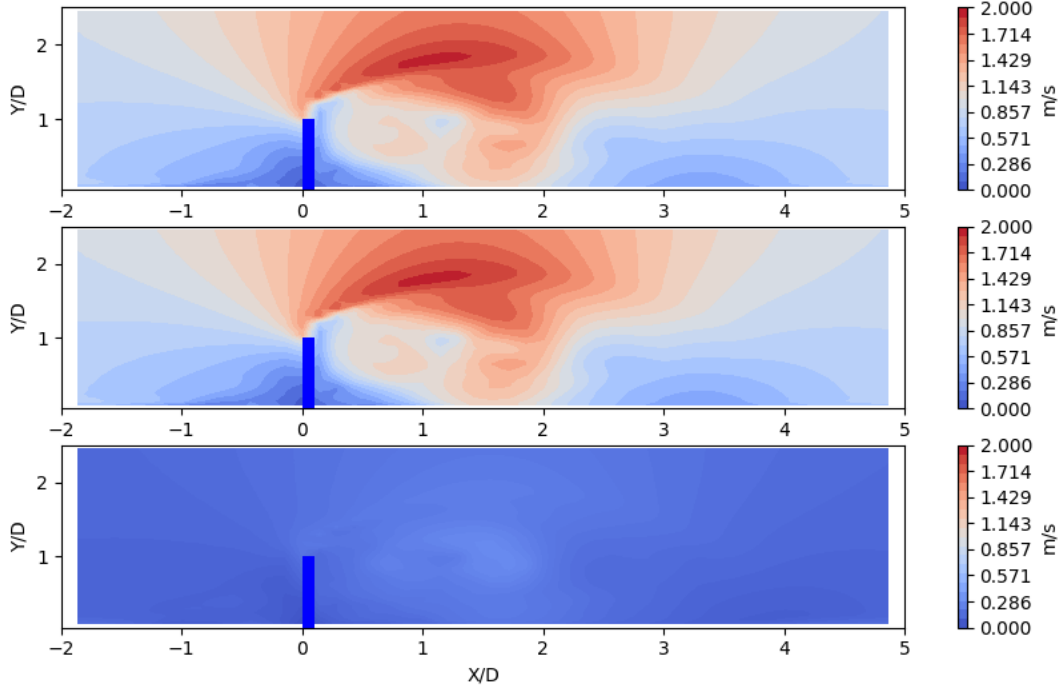


Figure 5.11: Mean flow velocity at three vertical layers, top) $H = -0.05$ m, middle) $H = -2.60$ m and top) $H = -4.90$ m

Two vertical profiles of mean current magnitude at $Y/D = 0.5$ and $Y/D = 1.0$ is used to explain the characteristic of 2DCS in the mean flow as shown in Figure 5.12. In the section A, $Y/D = 1.0$ where the eddy starts to develop, uniform distribution of high current magnitude over the depth is found close to the groyne (see Figure 5.12a). In addition, the current magnitude in this area is 50% to two times higher than the incoming flow magnitude except in the bed region. Attached eddy together with the groyne local effect exist and amplified flow velocity in this area. A similar trend is observed at $Y/D = 0.5$ in which uniform flow structure is found from the surface to the bottom layer as shown in Figure 5.12b. In contrast to the groyne tip profile, where flow amplification is found along the section, high current magnitude starts to develop at $X/D = 2$ as a result of eddy interaction in this region. Overall, the uniformly distributed current magnitude following eddy structure is a strong indication of 2DCS nature that can maintain its structure from the surface to the bottom as previously explained by Doron et al. [21].

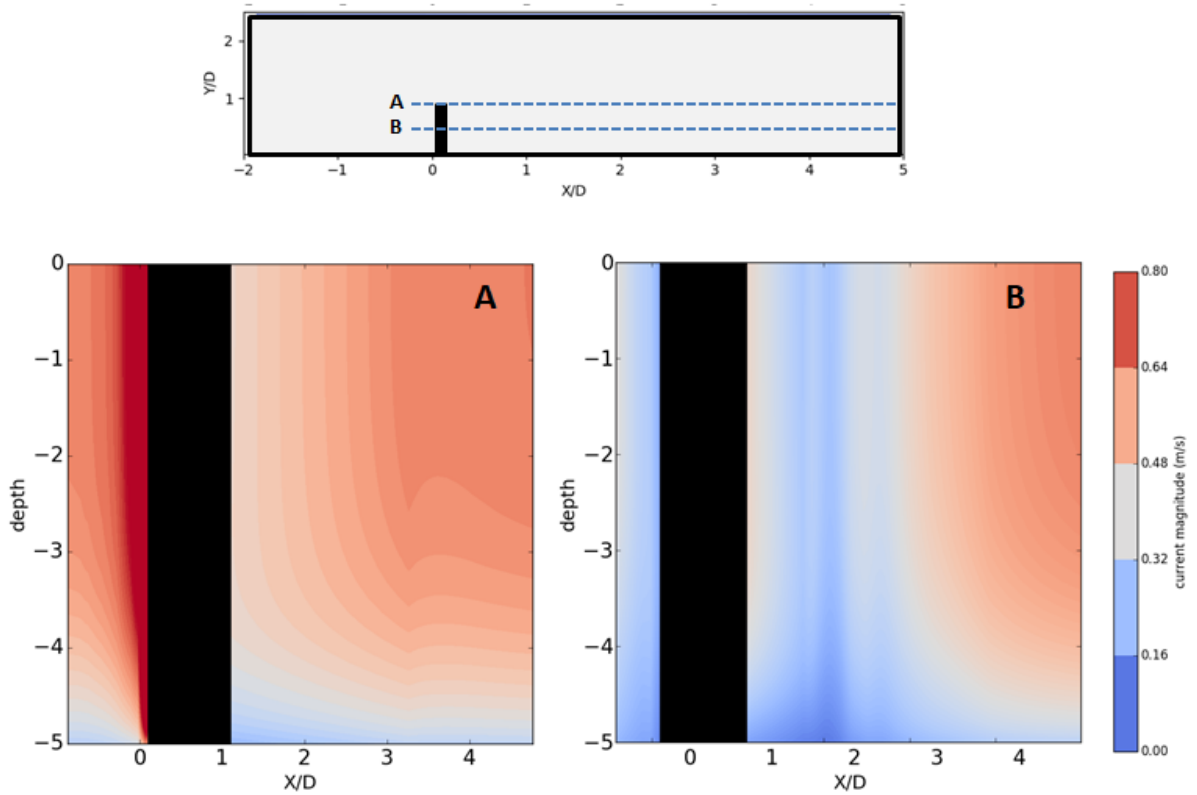


Figure 5.12: Mean current magnitude along the horizontal line at (a) $Y/D = 1.0$ and (b) $Y/D = 0.5$

5.3.6 The HV system

On the upstream side of the groyne, the model predicts the formation of a main corner vortex in the mean flow with the spanwise extent of the recirculation region takes $0.2D$ as shown in the Figure 5.13. The total streamwise length of the separated region is $0.7D$ with the centre of the vortex is positioned at $(x, y) = (-0.33D, 0.06D)$. A similar length scale has been reported by Koken and Constantinescu [108] which obtained $0.77D$ in LES simulation and $0.78D$ in the experiment. The interesting point of this study is the velocity magnitude inside the HV in which show that the vortex moves in the clockwise direction with slower magnitude (section A and B). This condition contrast to the primary vortex inside the recirculation region where the velocity magnitude approximately equal with the main flow region.

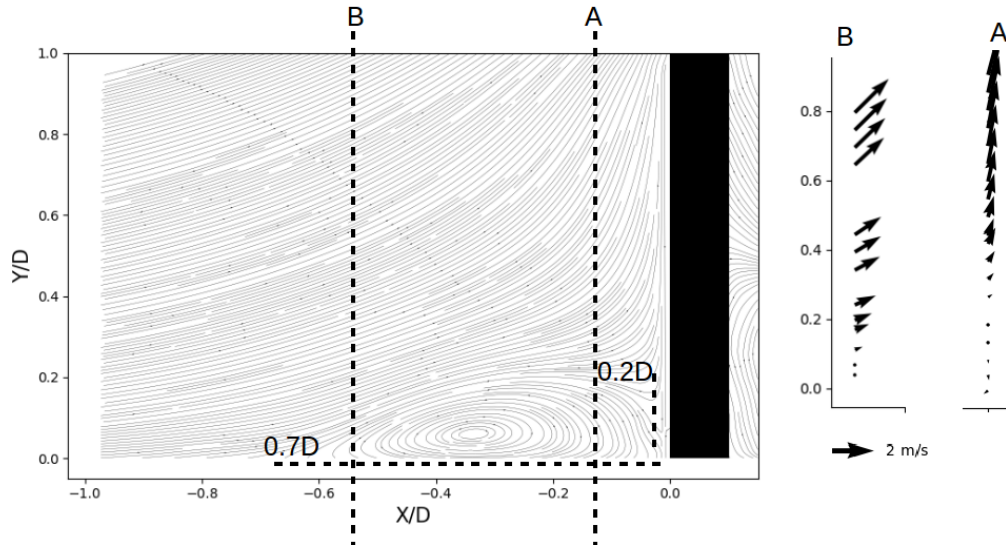


Figure 5.13: Mean flow velocity at the free surface in the upstream groyne region

To address the nature of the HV in the main flow it is necessary to consider the instantaneous HV in the upstream side of the groyne. Figure 5.14 shows the instantaneous HV for three vertical layers, for example, near surface, middle depth and near to the bed. These plots are obtained at certain time after fully developed condition achieved. Interestingly, the shape of the HV vortex changes from slender in the upper and middle layers to more compact at the close bed region as response to its position along the axis. At the bed, the vortex merges with migrating vortex and intensified the magnitude parallel with the entrainment small-scale turbulence from the bed. Attached to the groyne, the wall attached vortex (WAV) is present at the bottom layer. As it approaches the bed, this vortex starts bending in the spanwise direction before merging with the HV vortex. The interaction between the WAV and HV provides additional momentum to the flow inside the HV (Koken and Constantinescu [108]).

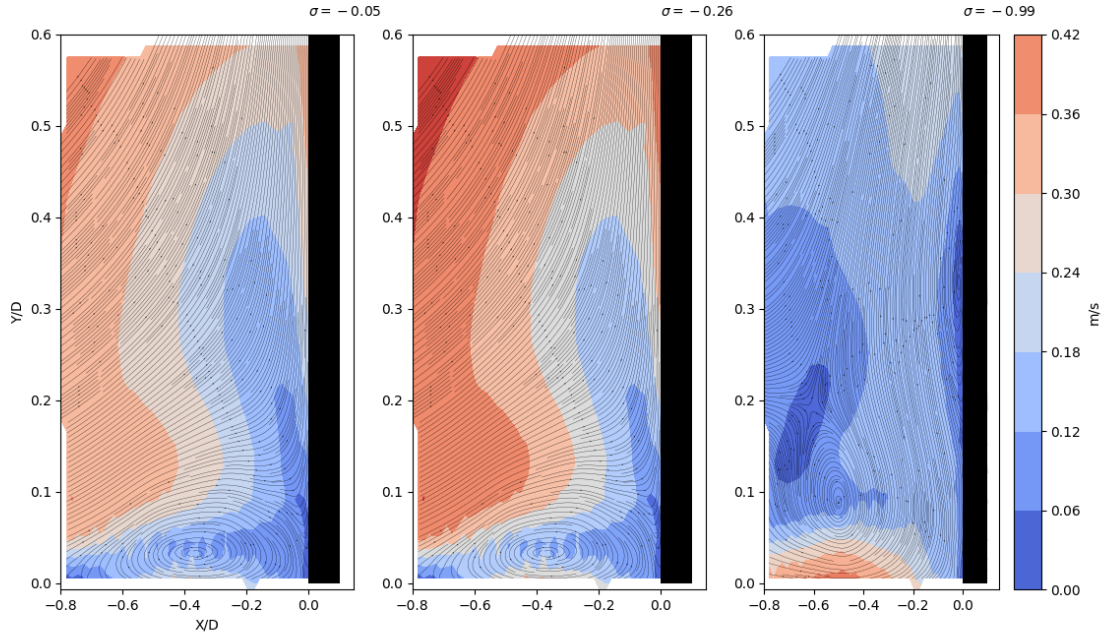


Figure 5.14: The instantaneous velocity and 2D streamlines at three sigma layers, $\sigma = -0.05$, $\sigma = -0.26$ and $\sigma = -0.99$

To examine the HV structure and its intensity along its main axis in more quantitative way, the resolved TKE at surface, middle and bottom layers are plotted in the Figure 5.14. Despite the 2-D streamlines properly show the presence of HV in the vertical direction, it has limited ability for determining the vortex size and position. Hence, scalar quantity such as TKE is more appropriate to represent high intensity in the HV system.

To be consistent with the LES concept only TKE from the large scale turbulent is observed in this study. Another reason is to reduce the influence of isotropic turbulence that is produced from the SGS. The present simulation results, distinctly show high TKE inside the HV system where the highest intensity is found around core of the HV vortex. Outside the HV, the resolved TKE structures follow the primary necklace vortex. This result is consistent with the simulation from Koken and Constantinescu [108]. In their simulation the structure extends from the main core to the SSL region. A contrast to the upper and middle layer with only single peak of TKE, two peaks are identified at the bottom layer describing the merging process between HV and WAV. Moreover, the bimodal nature of the flow inside the HV system also contributes to this condition as observed by Devenport and Simpson [112].

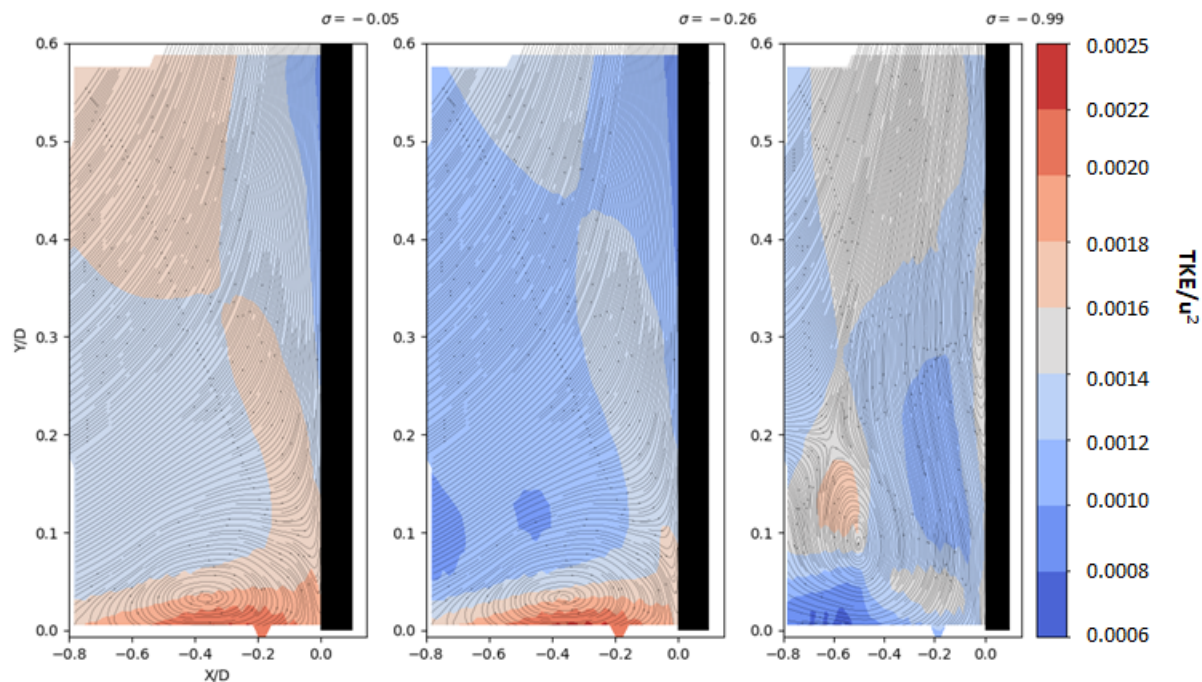


Figure 5.15: Mean 2D streamlines and resolved TKE at three sigma layers, $\sigma = -0.05$, $\sigma = -0.26$ and $\sigma = -0.99$

5.4 Summary

The present numerical investigation of the flow over single groyne provided depth understanding of the flow physics and dynamics of the large coherent structures. The ASM-LES concept showed good performance to resolve the flow structures. The generation of vortex tubes from the tip of the groyne that induces velocity amplification inside the shear layer is captured by using $\Delta/L = 1/20$ mesh size in the simulation. Comparison with results from coarser mesh size $\Delta/L = 5/20$ and $\Delta/L = 2.5/20$ confirms that the main coherent structure is in the scale of $\Delta/L = 1/20$.

The jittering process at the separated shear layer was caused by the convection of highly coherent structures from the boundary layer separating on the side wall, upstream of the groyne. A main finding of this case is that the generation of the vortex tubes from the tip of groyne strongly changes the orientation of the detached eddy. At some point this eddy is forced back flow in the upstream direction before re-entering the recirculation area with another vortex tube. The interaction between detached eddy and the side wall developed main circulatory motion in the recirculation region. At this point the existence of the eddy is not only on the instantaneous flow condition, but also in the mean flow.

The investigation of the primary eddy inside the recirculation region showed varying shapes over depth. It is sharper near the bed and larger as reach the surface layer.

Interestingly, the core of this vortex is not exactly oriented in the vertical direction. This contrast with the vortex tube in which the core moves in the vertical direction. Another important result is that there are two vortex cores developed inside the primary eddy resulting slow moving zone in the recirculation region.

Simulation results showed that the eddy interaction undoubtedly affected the transfer of resolved TKE. The interaction between large primary eddy re-enter the circular motion with the convected vortex tube produces a pair of low and high TKE regions. More importantly, the highest TKE value is found in the largest coherent structures and due to its temporal evolution sometimes lead to increase the bed shear stress along the path. The spectrum analysis confirms similar finding with the resolved TKE analysis. In the region where two or more vortical structures interact, higher energy level can be observed.

The HV structures reproduced by the model have similar dimension with the experimental result. The shape of the HV structure depends on its position along the axis. It is slender at the upper layer and more compact as reach the bed. The interaction with the WAV at the bottom layer provides additional momentum to the HV system. Consistent with other structures high resolved TKE is found inside the core of HV while in the outer region the TKE structure follows the path of primary necklace vortex.

The role of the vortical structures in the mean flow can be observed in the recirculation region. Two coherent structures exist in the mean flow affecting the circulatory motion at the downstream side of the groyne. Contrastingly, the vortex tubes that induce flow amplification is removed due to the averaging procedure in the mean flow.

Chapter 6

Flow over a series of groyne

6.1 Introduction

The model is applied to study the sediment transport process between the main channel and the groyne fields. First of all, the detail of the flow patterns near groynes is investigated by resolving the large coherent structures. The model results are then analysed and validated by using experimental data from Yossef [19]. At the second stage, one-way coupling with the sediment module is conducted through offline procedure to minimise the computational time. Both suspended and bedload sediment modules are used to describe fine sand transport inside the embayment and main channel.

To that end, the case was conducted with the following objectives:

- to investigate the dynamics of the flow and its associated coherent structures near groynes
- to study the effect of the resolved structures in the groyne fields
- to investigate the role of vortical structures in sediment transport inside groyne fields.

Firstly, section 6.2 presents the simulation design following experimental set-up from Yossef [19]. In the section 6.3 numerical results are discussed starting by analysing the mean flow, the HV system, the role of vortical structures inside embayment, turbulent energy and sediment transport. Furthermore, the morphological changes for relatively short time length are discussed in this chapter.

6.2 Numerical Simulation

The simulation is conducted in a 5 m wide and 30 m long channel with a series of groynes placed 12 m from the inlet. Each structure has equal distance of 4.5 m. The domain

is made with the same configuration as a physical model of Yossef and de Vriend [2] for the emerge groyne condition. Fig.6.1 shows a schematic illustration of a model set-up with particular emphasis on the fourth groyne fields where data from the experiment are compared with the numerical result.

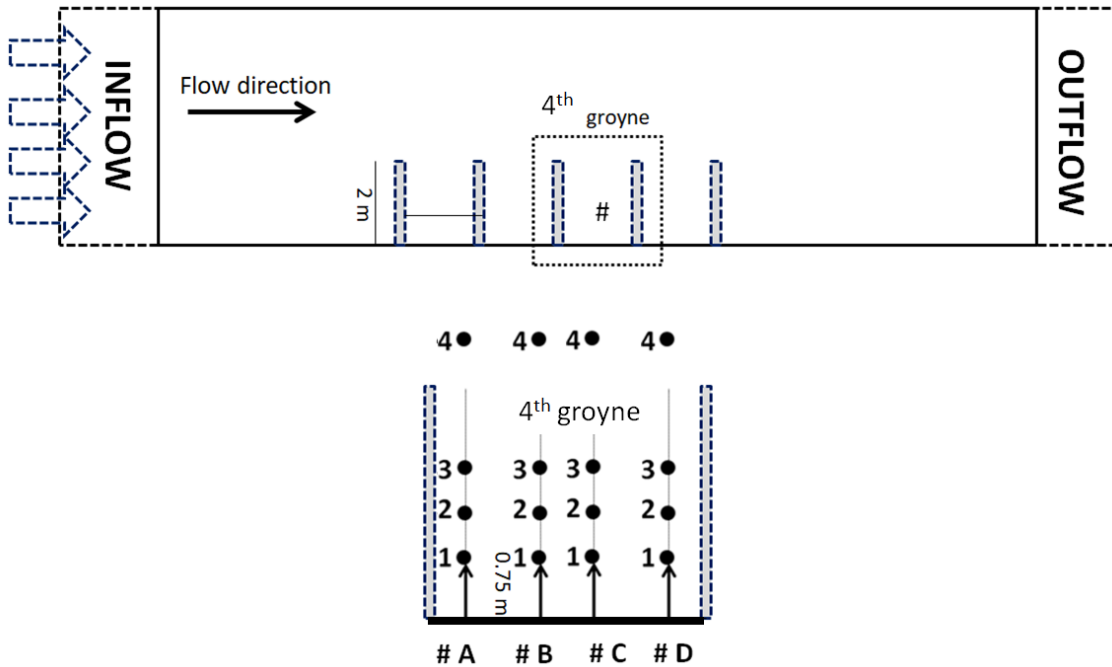


Figure 6.1: Schematic illustration of numerical simulation: # indicated four cross-section measurement points of laboratory test (modified from Yossef [19, p. 31])

The model bed is fixed and flat in the main channel. A constant water transport and specified surface elevation are imposed at the inflow and outflow boundary. The horizontal mesh resolution is uniform for the whole region with value 0.05 m ($\Delta/L = 0.025$) and 50 non-equally distributed layers are used in the vertical directions. Simulation of fine sand ($D_{50} = 0.164$ mm) is conducted for both suspended and bedload transports. More detail conditions are described in the Table 6.1

Table 6.1: Conditions for flow over a series of groyne

Parameters	Value	Units
Water depth h	0.25	m
Mean flow velocity V	0.3	(ms^{-1})
Bed roughness height k	0.7	cm
Bed Nikuradse equivalent sand Roughness (k_s)	1.0	cm
Flow simulation	5	hours
Computational time step	0.0001	s
Output time step	1	s
Density of sediment	2650	kg/m^3
D_{50}	0.164	mm
Sediment settling velocity, w_s	0.019	ms^{-1}

6.3 Result and discussions

6.3.1 Mean flow data analysis

As the flow reaches the first groyne, the shear boundary layer separates as a result of adverse pressure gradient generating main vortical system in the flows, such as the HV system, recirculating flow upstream of groyne and vortex tubes inside the separated shear layer (Koken and Constantinescu [107]). In this study, the length of the groyne (D) is used as the length scale. By using this scale, the total water depth is $h = 0.125D$.

The mean velocity streamlines for four vertical layers are observed to describe the main vortical structure in the base flow. Mean velocity fields were averaged after steady condition achieved at 01:10:00 simulation time to ensure convergence of the velocity statistics. Figure 6.2-6.5 represent the 2-D velocity streamlines and magnitude for four depths. It is observed that the primary eddies were resolved in the horizontal plane. The secondary eddies at the groyne fields 1 and 2 only resolved at the surface layers ($h = 0.03$ and $0.06D$) and it's presence disappear at the deeper layers. This contrast with the secondary eddies at the groyne fields 3 and 4 in which somehow able to maintain its forms. In general, the circulation patterns in the groyne fields show similar behaviour with the experiments from Uijttewaal et al. [113], Uijttewaal [114], Yossef [19] and Kang et al. [115].

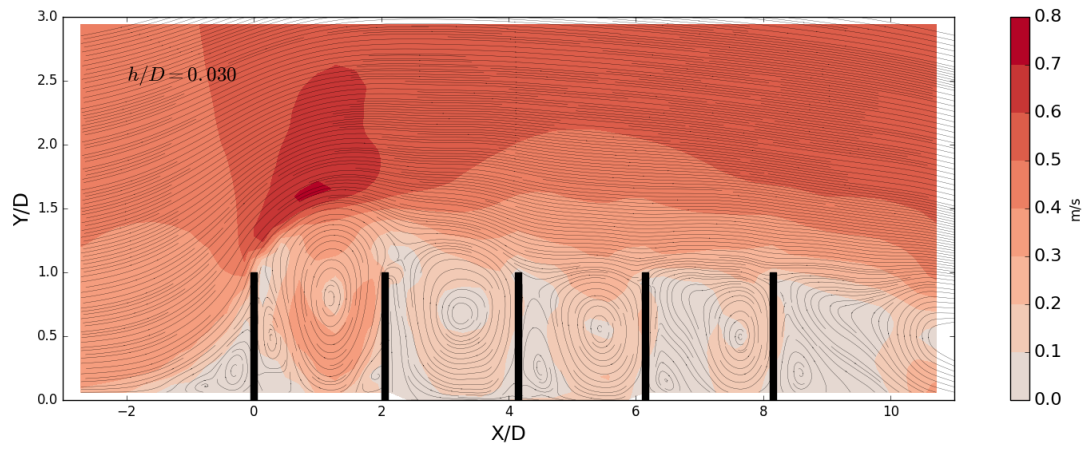


Figure 6.2: Visualization of flow structure using 2-D mean velocity streamlines near free surface $h/D = 0.03$.

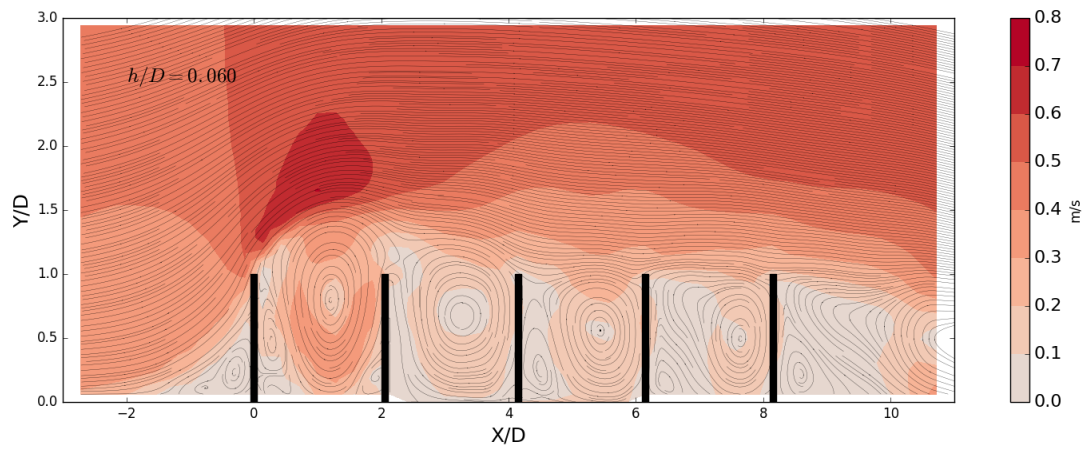


Figure 6.3: Visualization of flow structure using 2-D mean velocity streamlines at $h/D = 0.06$.

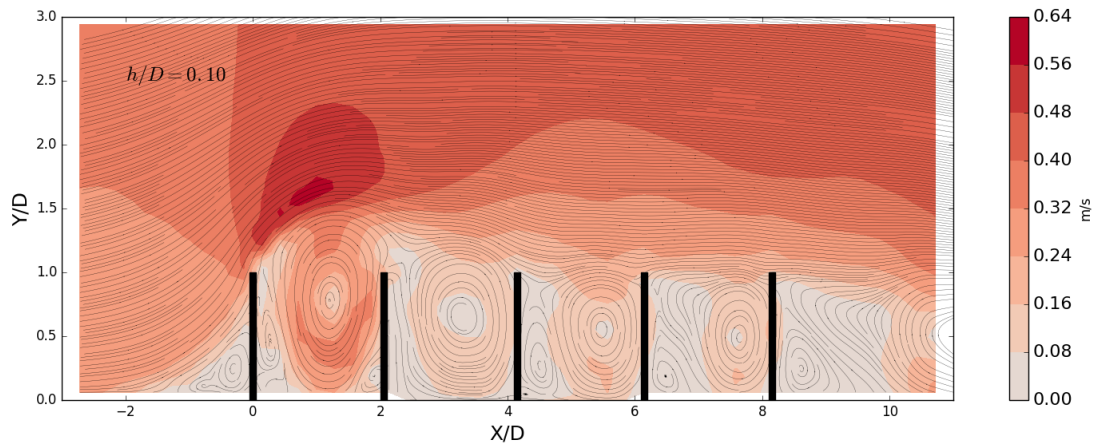


Figure 6.4: Visualization of flow structure using 2-D mean velocity streamlines at $h/D = 0.10$.

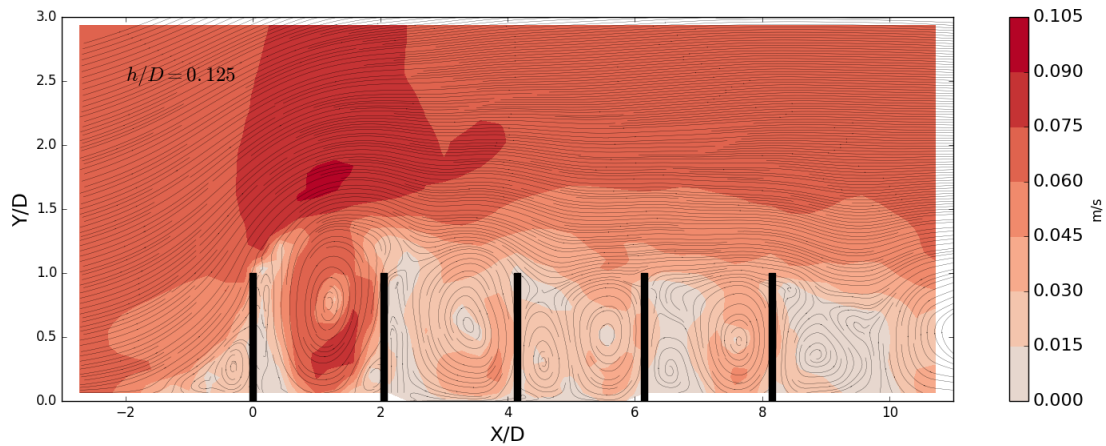


Figure 6.5: Visualization of flow structure using 2-D mean velocity streamlines at $h/D = 0.125$.

The velocity magnitude contours indicate that the velocity fields is greatly affected by the groyne length. The surface velocity profile shows the typical flow patterns of impermeable groyne where the contraction from the groyne length intensified the velocity at the tip of the groyne (e.g. Figure 6.2 and 6.3). In the main channel, the velocity has averaged value of 0.4 ms^{-1} . This value is one to two times higher than in the groyne fields. Similar finding has been reported by Mostafa et al. [109] which investigated the flow around the river's floodplain. In their experiments the relative longitudinal velocity in the opposite region rise to 75, 125 and 175 % with respect to the groyne length.

6.3.2 The HV system

The flow structures at the upstream side of groyne describes the formation of complex HV system span from the surface until the bottom layer. Paik and Sotiropoulos [104] described this structure as a complex system of multiple, large-scale necklace vortices with high turbulence kinetic energy. As explained in the left side of Figure 6.6 the transverse roll-up of the incoming flow forms two coherent structures that wrap around the structure. The HV system is composed of a primary necklace vortex directly attached to the obstruction and an elongated vortex upstream of it. The main vortex is initially parallel to the upstream side of groyne and then its size grows as reach the bottom layer. The presence of HV at the bottom corner of groyne induces large-scale aperiodic oscillation contributing to the high turbulence levels inside HV core. McCoy et al. [116] found that the TKE is significantly amplified within region occupied by the main necklace vortex. It is evident that the HV system is not single structures, but formed by a set of unsteady, multiple necklace-like vortexes. Similar findings have been reported by Paik and Sotiropoulos [104] and Devenport and Simpson [112] in the upstream junction region of a wall-mounted, wing-like obstacle and the wall.

The presence of the structures inside the HV system is also captured in the instantaneous condition. Animation shows that the interaction among these structures takes place in $X/D = -0.6$. Despite the interaction affected the size of the eddies, the shape is remain unchanged during the process.

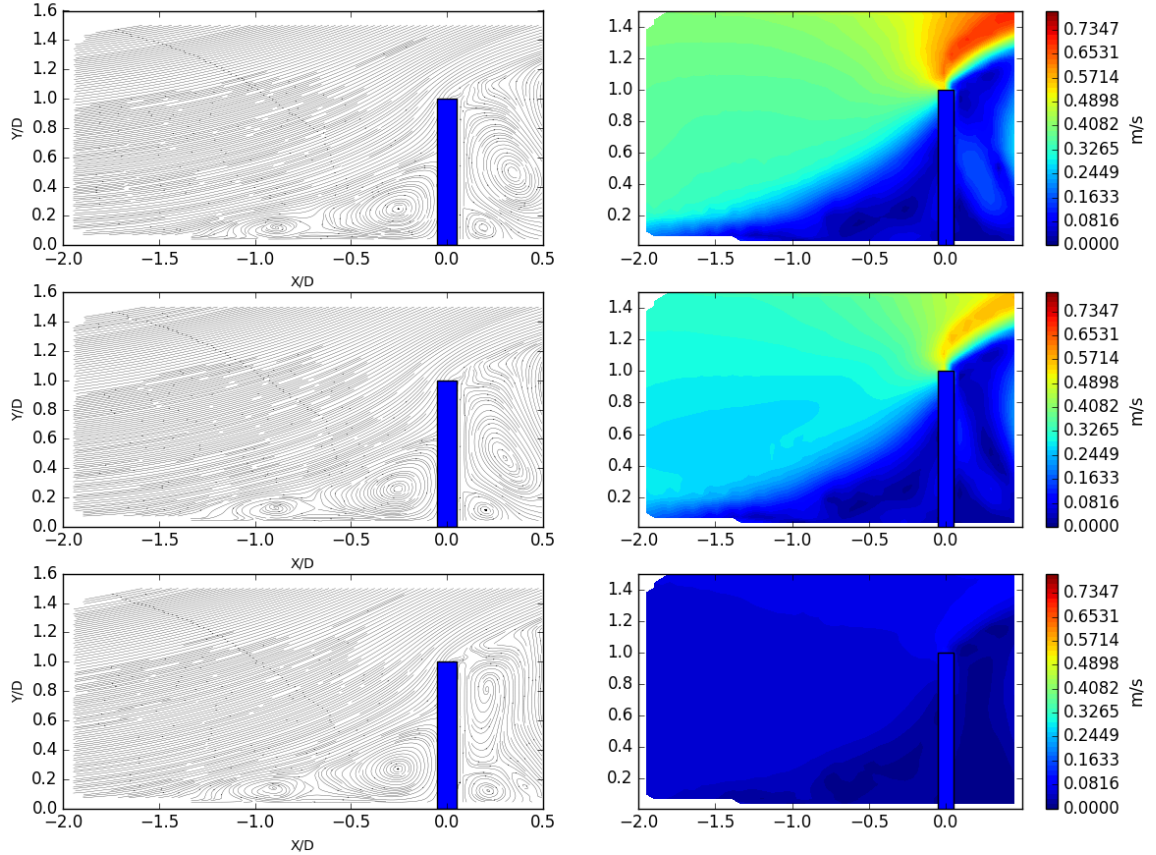


Figure 6.6: The mean velocity streamlines (**left**) and velocity magnitude (**right**) of $h/D = -0.05$, $h/D = -0.26$ and $h/D = -0.9$.

6.3.3 The role of large coherent structures in groyne field

As observed in the Figure 6.7 the mixing layer starts at the tip of groyne and grows in the downstream direction. To gain more insight related the LSCS inside the groyne field and its interaction with the main flow, we analyse the mean flow structures from the fourth groyne field and compare with experimental data from Yossef [19]. Figure 6.7 illustrates the circulation pattern inside groyne field as previously reported by Uijttewaal et al. [113] and Yossef and de Vriend [2]. Three eddies, namely clockwise-primary, anti-clockwise secondary and clockwise dynamic eddy are described in the plot.

According to Uijttewaal et al. [113] a primary eddy that develops in the downstream part of the groyne field can cover approximately two thirds of groyne field space. It has 30 to 40% of the main channel velocity. In this study, the velocity at the primary eddy

has an average value of 0.15 ms^{-1} which equals to 37% of velocity in the main channel. A secondary eddy is fed by the primary eddy and moves in the opposite direction with smaller velocity. Our result obtains velocity value of $0 - 0.18 \text{ ms}^{-1}$ for the secondary eddy. A dynamic eddy shed regularly from the tip of the upstream groyne and translate following the flows. This eddy can merge with the primary eddy and upgrade its size before disappearing. During the interaction with the migrating eddy, the size can grow to two times of its regular size as shown in the Figure 6.7

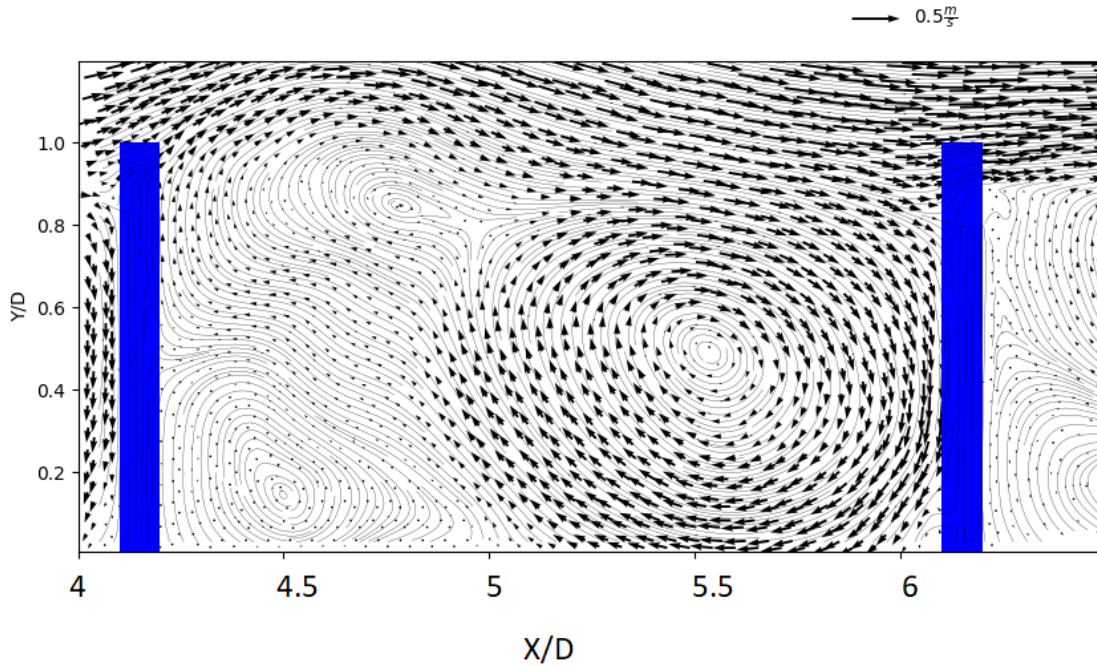


Figure 6.7: Flow pattern in the fourth groyne field

Yossef [19] showed that the velocity fluctuations represent shallow turbulent flows at the region close to the upstream groyne. Here we compare the velocities from the model with the experimental data from Yossef [19] at point A2 attached to the upstream groyne (see Figure 6.1).

Figure 6.8 presents the comparison between the model results and experiment. The data are obtained from last 80 seconds simulation while experimental data are collected over 600 seconds with a sampling rate of 10 Hz. The data show that the velocity fluctuations in stream-wise direction are two times higher than in the transverse direction. Moreover, oscillations with a period of 8-10 seconds were recorded. Model results show very good agreement with the experiment, particularly for the stream-wise velocity while in the transverse direction, model under-predicted the velocity and unable to capture the high-frequency velocity.

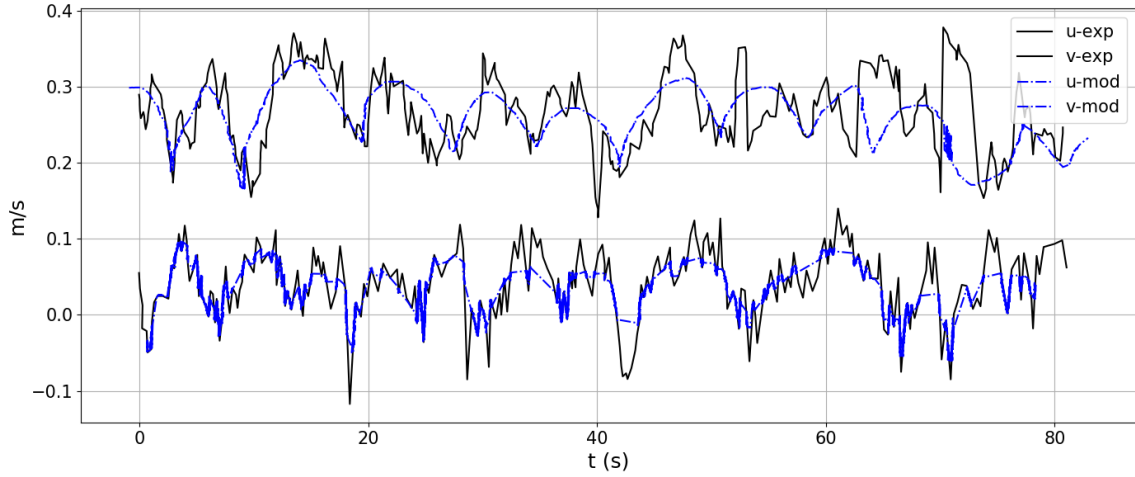


Figure 6.8: Stream-wise and span-wise velocities from the model (dashed blue line) and experiment (black line) at point A2 (see Figure 6.1)

6.3.4 Turbulent energy

To examine the different turbulent scales in the velocity data in the groyne field, the autocorrelation functions and energy spectra are used. First, we use stream-wise velocity that has been normalised by its variants in order to obtain autocorrelation value and time lags. Then, the spectra energy is calculated by using stream-wise velocity fluctuations to represent the distribution of turbulent energy over difference frequency.

Figure 6.9 reveals the autocorrelation function of the stream-wise velocity. The large turbulence structures are identified through the modulation characteristic which extend over large time lags. It has strong correlation with the length-scale turbulence structures. In the groyne field at A1 and D1 (see Figure 6.1), the autocorrelation value produces negative and positive value over large time lags. This is the indication of the large turbulence structures in the groyne field which mainly produced by primary eddy. Close to the detachment point (Point A2) strong modulation exist with shorter time lags. Here we can identify the contribution of dynamic eddies at the upstream and downstream side of the groyne. Point 3 and point 4 show weak modulation as in this region, primarily affected by the small scale turbulence structures. Generally speaking, the characteristics for section A and D are similar corresponding to the same turbulence structure in these two transects.

Despite autocorrelation function show identical shape, the energy distribution over various frequencies is different depend on the turbulence sources. At section D where the primary eddy generated and interacts with migrating eddy, the energy distribution is more prevalent compare to the section A. Figure 6.10 describes the energy density of

observation points. A single peak can be recognised inside the groyne field for each Point A1 and D1 as a consequence of primary eddy domination. The peak exists at the high frequency and more fluctuations are found at the lower frequency in section D1. This can be interpreted as the generation of the eddy over the length scale of section D to section A.

The energy spectra at the mixing layer (Point A2) produces more peak due to the presence of secondary and dynamic eddy. These eddies that shed regularly produced a significant amount of turbulent energy due to its dynamics in the groyne field. The similar finding can be seen from the autocorrelation function presented in the Figure 6.9. For the region outside the groyne field (Point 3 and 4) the contribution of migrating eddy is less significant. However, these points are subject to the mixing layer upstream of the groyne. The energy spectrum is mainly produced from the small scale turbulent correspond to the significant amount of energy in the low-frequency.

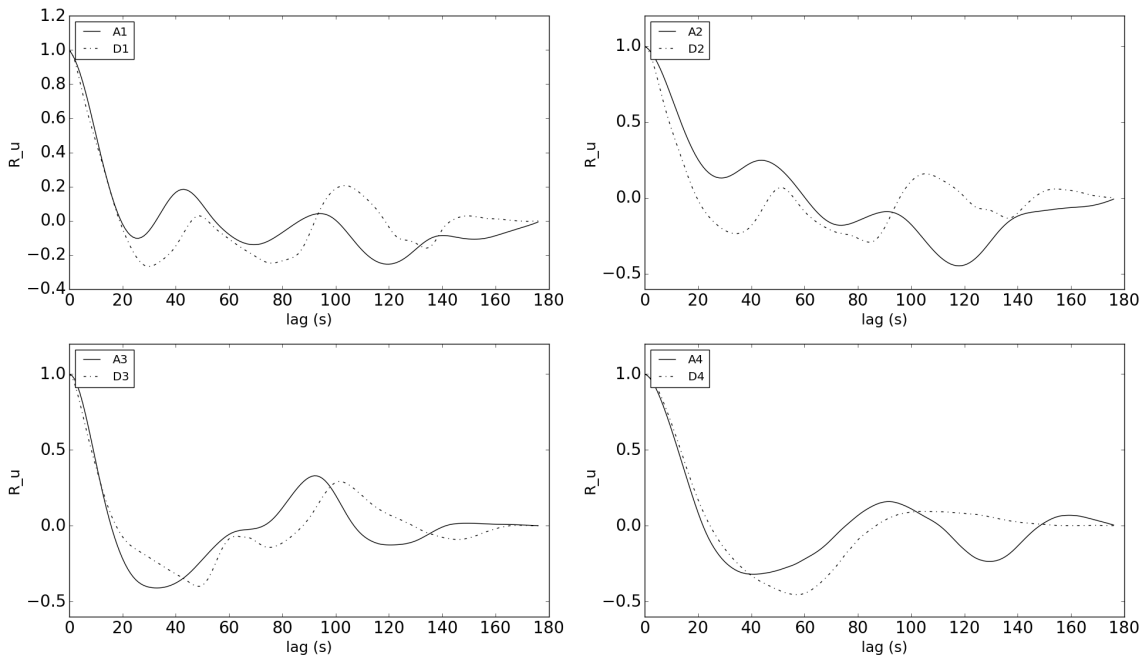


Figure 6.9: Autocorrelation functions of stream-wise velocity fluctuations at sections A and D. Point 1 and 2 are located inside the groyne field.

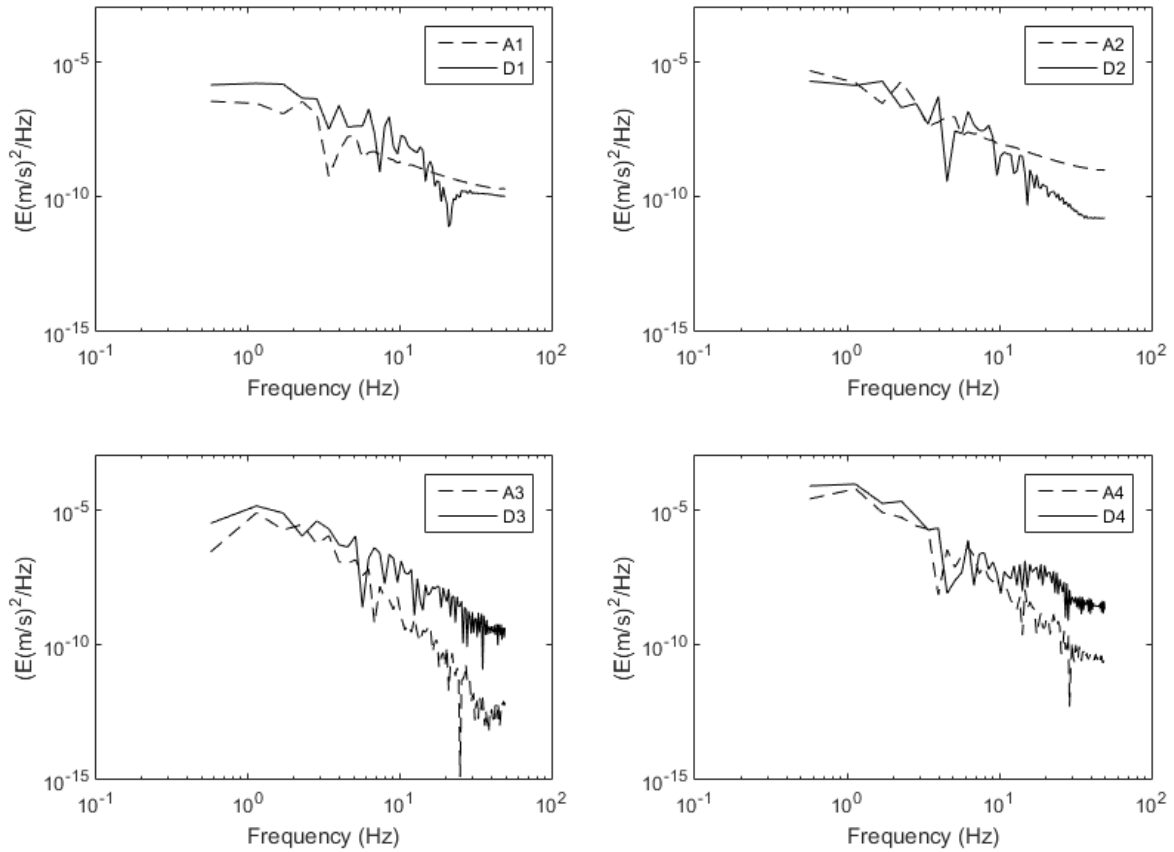


Figure 6.10: Energy density spectra of stream-wise velocity fluctuations at sections A and D. Point 1 and 2 inside the groyne field

6.3.5 Sediment Transport

The sediment is transported from the main channel into groyne field following the primary circulation cell. In the region where the velocity is low, the sediment has more chance to settle. Figure 6.11 shows the time-averaged of suspended sediment concentration for three vertical layers where high deposited sediment is generally found inside the groyne fields. The deposition region, which is formed in the groyne field engages with the flow pattern corresponding to the vortical eddy structures.

Its found that the first groyne field has more deposited particles than other regions, which is caused by strong flow deflection from the first groyne. Approximately more than 0.4 g/L particles are deposited at the downstream part of the first groyne. This value is 0.1 g/L higher than the other groyne fields. Interestingly, for all four groyne fields the high deposited sediment takes place around the primary eddies. It has been discussed in the previous section that the eddy has varied shape over the depth but consistently

maintain the energy. The combination of the high-containing energy, primary eddy, with the quasi-periodic flows inside groyne fields produces high deposition regions. As the sediment reaches the bed, more particles are concentrated. This condition is caused by high bed shear stress, which entrained substantial amount of sediment from the bed into suspension. As a consequence, the concentration patterns in the middle and near bed layers indicate more dynamic condition than the surface layer.

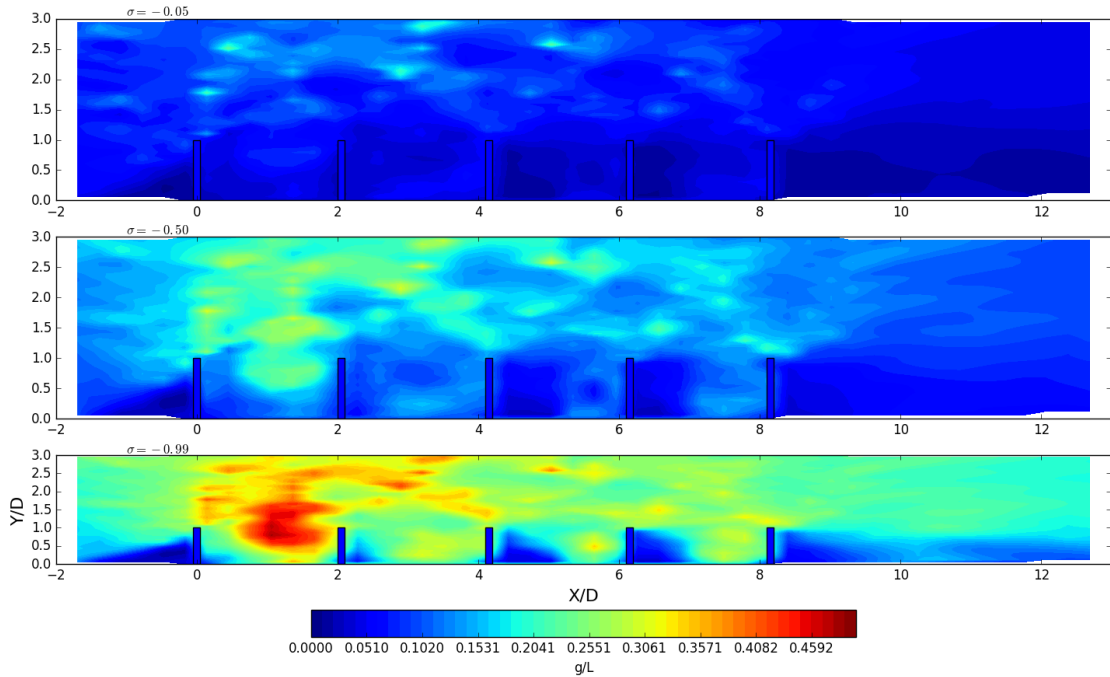


Figure 6.11: Mean distribution value of suspended sediment concentration in $\sigma = -0.05$, $\sigma = -0.50$ and $\sigma = -0.99$

While the suspended transport is more affected by the primary circulation, the bedload transport rate shows dominant influence from the vortex tubes as shown by Figure 6.12. It is because the core of vortex tubes that shed from the groyne evolved in the vertical direction. As a consequence, additional horizontal vorticity is induced in the near-bed region and greatly affected the sediment movement (Koken and Constantinescu [107]). This is evidenced by high value of rate transport inline with the vortex tubes direction. Following the flow obstruction by groyne tip, deposition takes place until $X/D = 2$ where highest concentration occurs inside the core. Approximately, bedload rate transport more than $0.001 \times 10^{-2} \text{ kgms}^{-1}$ is found in this area. In fact, the value is two times higher compared to the main channel.

Interesting finding from this study is that the sediment distributions inside groyne

field resemble the flow fields, resulting high concentrated regions in the downstream part of groynes. It shows the dominant roles of eddy structures. A pairs of bimodal, relatively high deposition and erosion zones are identified next to the primary and secondary vortex. As a result the sediment particles are transported through re-circulatory motion and settle on the side wall.

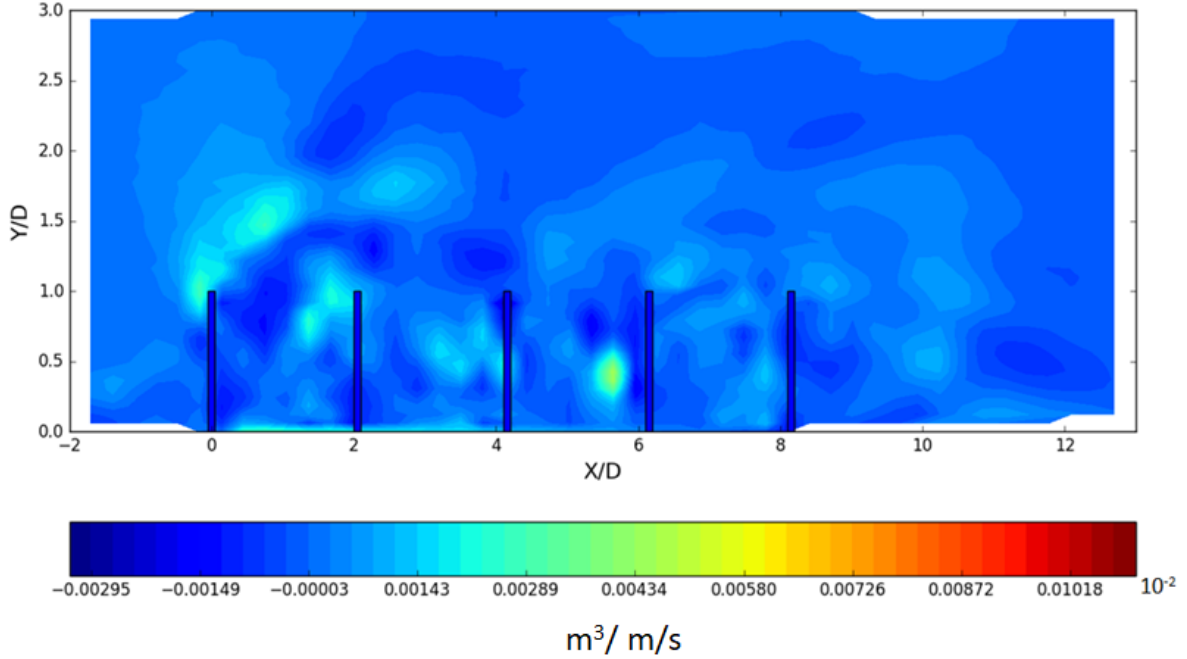


Figure 6.12: Bedload transport rate

The general pattern of suspended and bedload transport show strong domination of LSCS structures. However, the primary vortex tubes somehow affect less suspended transport at the tip of first groyne. This is partly due to the loss of energy at the water column with respect to the merging process with the downfall vortex from the separation layer. Despite the weak influence from the vortex tubes, this study found that the contribution of high turbulent eddy is more prevalent in the suspended rather than the bedload transport in this particular test.

The assessment of the fourth groyne field is made to see the exchange process of sediment leaving/entering the field. Four cross-sections are presented in the Figure 6.13a, namely section A, B, C and D, which are positioned at $X/D = 4.35$, $X/D = 5.00$, $X/D = 5.50$ and $X/D = 6.00$, respectively. The length in the transverse direction is $3.0 X/D$. The sediment transport rate presented in those figures are obtained from the last 30 minutes simulation after fully developed condition achieved. The data are both averaged over time and depth to properly represent the transport mechanism inside the groyne field.

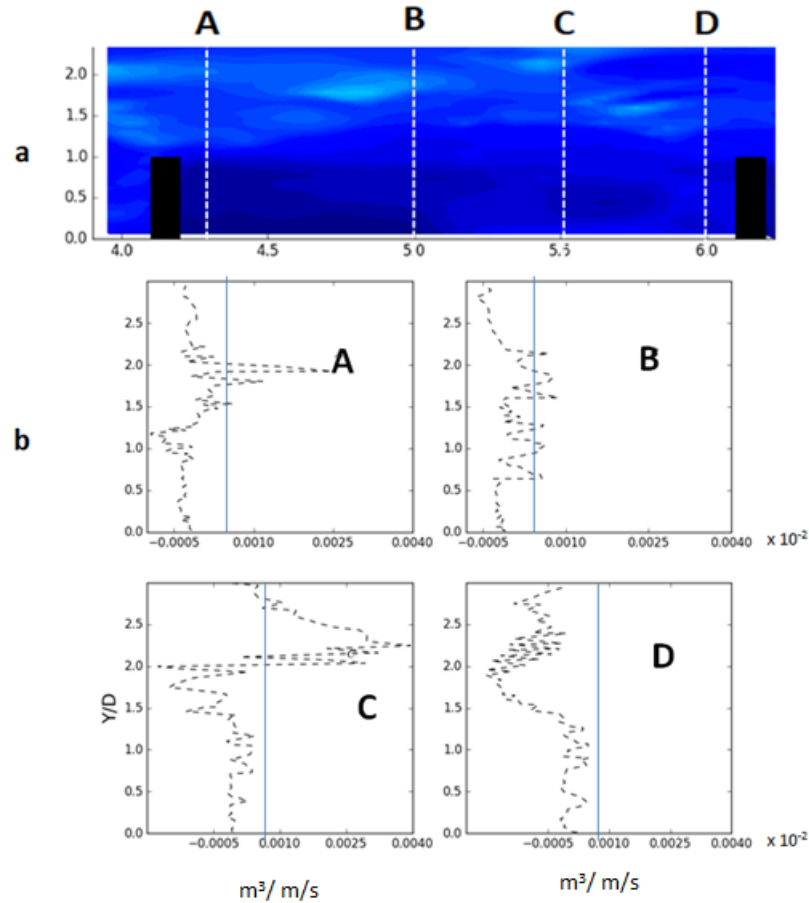


Figure 6.13: **a** Cross-section lines, **b** The bedload transport rate in the transverse direction of A, B, C and D sections

The plots in Figure 6.13b shows the distribution of bedload transport rate in the main channel and groyne field. As illustrated by the mean velocity streamline (see Figure 6.2) the primary eddy plays important role in the transport of suspended materials. McCoy et al. [105] explained that the flow convected into embayment region from the downstream can substantially accelerate both the removal or entrance of sediment. In this study the patch of primary eddy is closely associated with the high deposited region. Furthermore the core is observed as the region with highest deposited particles.

The amount is difference between embayments in which the largest value takes place inside the first groyne field due to the fact that more turbulence are found in the first groyne field than other regions. The sediment inside the groyne fields ($Y/D < 1$) are almost similar to all sections indicated equilibrium condition. Meanwhile, the value in the outer layer is more fluctuated, particularly at $1 < Y/D < 2$. The bedload transport calculates approximately $-0.005 \times 10^{-2} \text{ m}^3/\text{ms}$ for each section inside groyne field. The transport rate in the section A represent part of the import process from the main channel

affected by dynamic eddy around the tip of groyne. As a consequence, large sediment deposition is found around $Y/D = 1.5$. Contrastingly, at the section B and C where there are no direct transport from the main channel, equal distribution can be seen. In addition, another sediment entrance is represented by section D in which particles move through primary eddy. When this structure decreases its velocity, the deposition region started to form.

The corresponding suspended sediments along these four transects show more pronounced pattern than the bedload transport as shown in the Figure 6.14b. The rate of transport at the section A highlight the high value inside the groyne field. Similarly, sediment entrainment in the section D is evidenced by producing higher concentrations than the main channel. Overall, both bedload and suspended sediment are transported following primary circulation pattern inside groyne field where the existence of vortical structures significantly affected the local transport process.

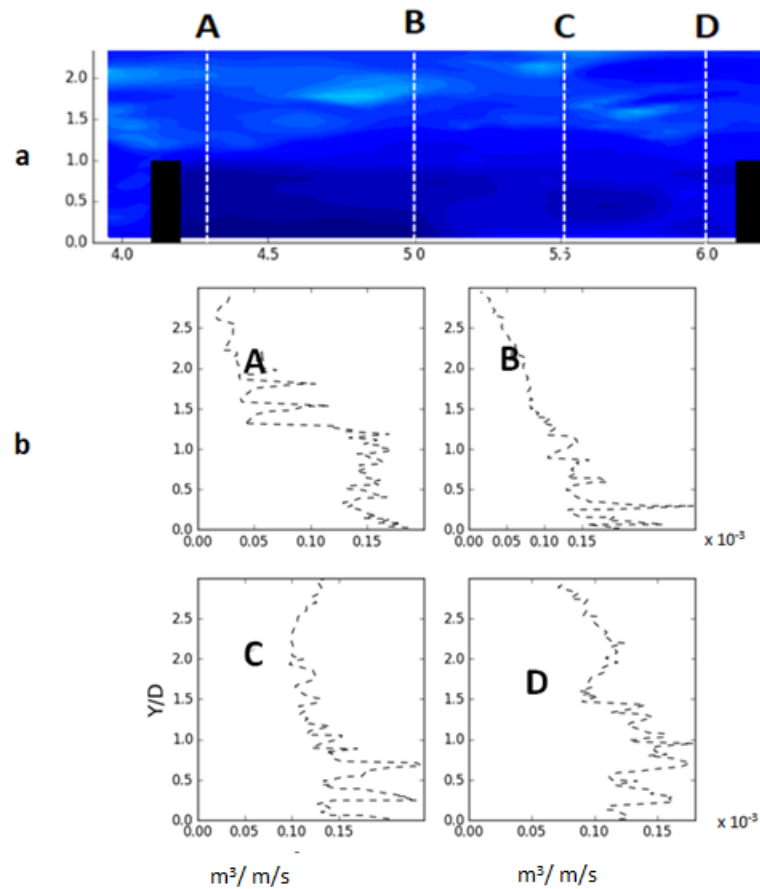


Figure 6.14: **a** Cross-section lines, **b** The suspended transport rate in the transverse direction of A, B, C and D sections

Another primary goals in this simulation is to investigate the temporal development in

morphology pattern. It should be noted that during the simulation, morphological factor of 10 is used to speed up the deposition/erosion process in the model. Figure 6.15 shows that strongest erosion part is found close to the tip of first groyne extends parallel with the main circulation. The distributions are mainly affected by strong-deflected flows transport in which vortex tubes dominated the flow fields. Interestingly the corresponding vortices only exist at the first groyne and then dissipated at $X/D = 3$.

After 50 hours simulation time, the largest erosion of -0.16 m is found at the tip of the first groyne while at most part of domain deposition of 0.039 m is obtained. In all groyne fields the existence of primary eddies tend to accelerate the flows and eroded the bed materials. This condition can be seen in the downstream part of the groyne fields where the vortical structures develop. Overall, the morphological features are similar in all fours groyne fields indicating that the flows are fully developed and the sediment transport process also reached equilibrium stage.

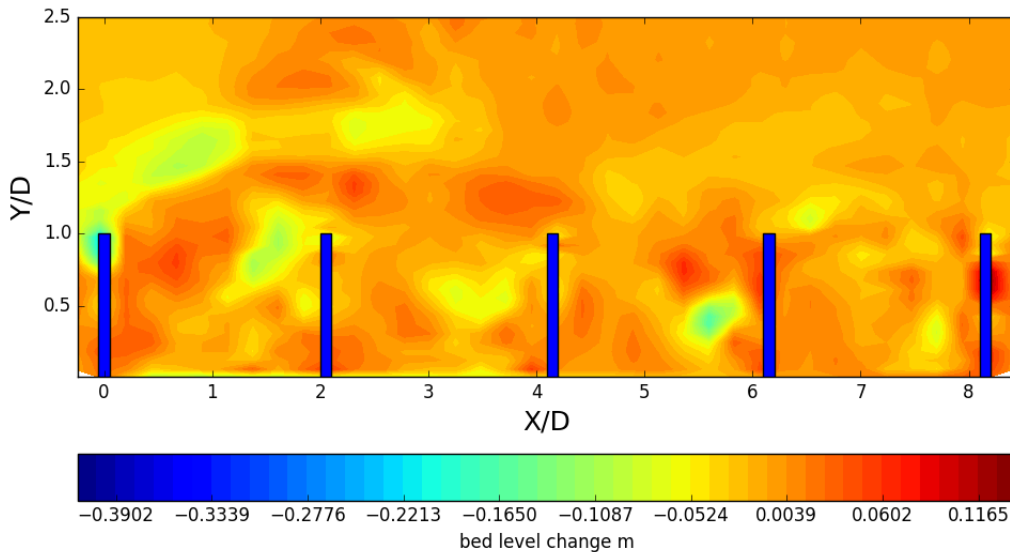


Figure 6.15: Bed levels change after 50 hours simulation

6.4 Summary

In this chapter the results of flow over a series of groyne simulation were discussed. The large vortical structures induced by groynes are properly resolved by the model. The primary and secondary eddies were observed for all groyne fields indicating typical flow patterns of impermeable groyne. As the flow reaches the structure the contraction intensified velocity magnitude two times higher than the incoming flow.

The transverse roll-up of the incoming flow at the upstream side of first groyne forms two coherent structures. It is identified as the formation of complex HV that composed of a primary necklace and elongated vortex. These structures induce large aperiodic oscillation at the bottom corner of groyne. An important finding from this study confirms that the HV system is not single structure but formed by multiple-like necklace vortexes.

Observation at the embayment revealed that the complex structures are mainly resolved by the model. The existence of primary, secondary and dynamic eddies were captured during simulation. The interaction amongst these eddies produces main circulatory motion inside the groyne field. The velocity magnitude of the primary eddy that occupies more than two third of the space is agree with the theoretical finding. The velocity fluctuations in the region close to the upstream groyne represent shallow turbulent flows with an oscillation period of 8-10 seconds.

In order to examine the turbulence energy level induced by the structures, analysis of turbulence spectrum energy is provided. Firstly, the autocorrelation function is used to identify the characteristic of modulation over large time lags. By using this technique, the development of the length-scale turbulence is preserved. Inside the groyne field the autocorrelation value produced negative and positive values over large time lags. The contribution of primary, secondary and dynamic eddies were captured for all transects with different time lags. The spectrum energy distribution showed the distinct shape with respect to its turbulence sources. At the region where the primary eddy interacts with the migrating eddy, a relatively high energy spectrum is observed. The later procedure generally confirms generation of turbulence energy inside groyne fields.

One of the main goals of this case is to study the role of vortical structures in the sediment transport. Therefore, one-way coupling procedure is conducted to simulate fine sand sediment. The simulation is run for 5 hours composed of suspended and bedload transport. The sediment is imported from the channel following the primary circulation pattern. It entrances the embayment through main eddy at the downstream part of the groyne. For the suspended particles, the existence of vortical structures strongly affected its distribution. Mean value analysis showed that the formation of high deposited region closely related to the primary eddy inside the embayments. Another important result of this simulation is that the flow obstruction generated erosion close to the tip of groyne extends parallel with the main circulation obtained after 50 hours simulation.

Chapter 7

Conclusions and recommendations for future research

7.1 Conclusions

From the hydrodynamic and sediment simulations described in the previous sections a number of conclusions and recommendations can be drawn for both the modelling approach and the physical phenomena.

- The flow over a cylinder test shows satisfactory results from the model compared to the experimental data based on the NRMSE value. More importantly, complex flow structures are captured by using different filter size for horizontal and vertical directions.
- It is feasible to apply the new FVCOM-LES to a real-life case as demonstrated by the single groyne case. Comparing with the unresolved eddy simulation with coarse mesh sizes provides indirect evidence that the resolved eddy increases velocity magnitude near the groyne tip. The contribution of vortical structure interactions for transferring TKE is recorded by the model for the HV system, separated shear layer and recirculation region. Energy spectrum from three monitoring points support this finding in which higher energy level is obtained at the recirculation and intensified region.
- The developed model is further applied to a laboratory experiment of flow over a series of groyne, in which velocity data and processed turbulence energy spectrum are used to validate the model at the Chapter 6. The flow represents shallow turbulent flows with oscillation periods of 8-10 seconds. Large turbulence structures are identified through strong modulation inside the groyne field. This condition also supported by a single peak of energy from the spectrum analysis for points A1 and

D1.

- The one-way coupling with the sediment module described that the pattern of suspended and bedload transports follows the circulatory motion induced by vortical structures. It is evidenced that the particles entrance groyne field through downstream primary eddy. Model results explained that the suspended transport are strongly affected by the coherent structure rather than the bedload.
- Relatively short temporal development in morphology is spotted from simulation. Strongest erosion takes place near the tip of first groyne resulted by strong-deflected flow transport, which vortex tubes dominated the flow fields.

Based on the simulation results, the answer to the research questions are arranged as follow:

- **RQ1:** To what extends the existence of 2-D eddy influenced the mean flow dynamics around groyne structure?

By using small enough mesh size and time step to guarantee the accuracy, the eddy structure can be resolved in this study. When applied in the prototype real-scale simulation, flow over single groyne, the complex flow structures are resolved by using $\Delta/L = 1/20$ mesh size. The simulation results reveal strong amplified region around the core of vortex tube as a result of the growth of Kelvin-Helmholtz instabilities. Two times higher velocity magnitude is recorded in this area. Furthermore, the extension of the amplified area is of $1D$ to $2D$ downstream of the groyne. This result is similar with the experimental findings from Safarzadeh and Brevis [117]. Another test, flow over a series of groyne in the laboratory scale indicates similar result with the single groyne case. Strong deflected flow indicating as groyne local effect at the first groyne tip increases the velocity magnitude to about 125% of incoming flow magnitude.

- **RQ2:** How far is the eddy interaction affected the turbulent kinetic energy?

The eddy interaction contributes to increase the turbulent energy level. Such results are described when compared the energy spectrum at the tip of groyne, amplification zone and the separation area for the flow over single groyne. When the eddy interaction exists, it produces more energy. Meanwhile, strong turbulence modulations over time lags inside the groyne field for flow over a series of groyne indicate large turbulent structure.

7.2 Suggestion for future research

Following the aforementioned conclusions, a number of recommendation can be given to further studies on this subject.

- Despite the C_h and C_v , the horizontal and vertical eddy constants, from Petronio et al. [99] procedure showed good results for all three cases, further calibration is required to test its behaviour in the more complex cases, for instance when the tidal exists.
- In the future, the effect of the sub-grid scale model of wave-induced currents around coastal structures need to be investigated for the real-life scenarios.
- Careful attention is required to use valid time computational step. In all cases we limited the Courant number to 0.8 for the barotropic mode.
- To take advantage from the adopted LES concept in the present model, the development of a new sediment module based on the particle tracking method is strongly suggested as future research.

Bibliography

- [1] Andreas Roulund, B Mutlu Sumer, Jørgen Fredsøe, and Jess Michelsen. Numerical and experimental investigation of flow and scour around a circular pile. *Journal of Fluid Mechanics*, 534:351–401, 2005.
- [2] Mohamed FM Yossef and Huib J de Vriend. Flow details near river groynes: experimental investigation. *Journal of Hydraulic Engineering*, 137(5):504–516, 2010.
- [3] Joseph Smagorinsky. General circulation experiments with the primitive equations: I. the basic experiment. *Monthly weather review*, 91(3):99–164, 1963.
- [4] Tai-Wen Hsu, Chih-Min Hsieh, and Robert R Hwang. Using rans to simulate vortex generation and dissipation around impermeable submerged double breakwaters. *Coastal Engineering*, 51(7):557–579, 2004.
- [5] R Grant Ingram and Vincent H Chu. Flow around islands in rupert bay: An investigation of the bottom friction effect. *Journal of Geophysical Research: Oceans*, 92(C13):14521–14533, 1987.
- [6] Daoyi Chen and Gerhard H Jirka. Experimental study of plane turbulent wakes in a shallow water layer. *Fluid dynamics research*, 16(1):11, 1995.
- [7] Carl Fr v Carmer, Andreas C Rummel, and Gerhard H Jirka. Combined planar measurements of flow velocity and mass concentration in shallow turbulent flow part 2: Application of coupled piv-pca to turbulent shallow wake flows. In *Hydraulic Measurements and Experimental Methods 2002*, pages 1–10, 2002.
- [8] Jeremy G Venditti, Richard J Hardy, Michael Church, and James L Best. What is a coherent flow structure in geophysical flow? *Coherent flow structures at Earth's surface*, pages 1–16, 2013.
- [9] Georgios A Leftheriotis, Athanassios A Dimas, et al. Large-eddy simulation of oscillatory flow, sediment transport and morphodynamics over ripples. In *The 27th International Ocean and Polar Engineering Conference*. International Society of Off-shore and Polar Engineers, 2017.

- [10] RA Kostaschuk and MA Church. Macroturbulence generated by dunes: Fraser river, canada. *Sedimentary Geology*, 85(1-4):25–37, 1993.
- [11] GA Liek, JA Roelvink, and RE Uittenbogaard. The influence of large horizontal eddies on the depth, shape and extent of scour holes. *SASME Book of Abstracts*, 2000.
- [12] Carolanne VM Vouriot, Athanasios Angeloudis, Stephan C Kramer, and Matthew D Piggott. Fate of large-scale vortices in idealized tidal lagoons. *Environmental Fluid Mechanics*, 19(2):329–348, 2019.
- [13] JW Kim, HK Ha, and SB Woo. Dynamics of sediment disturbance by periodic artificial discharges from the world’s largest tidal power plant. *Estuarine, Coastal and Shelf Science*, 190:69–79, 2017.
- [14] C Hinterberger, J Fröhlich, and W Rodi. Three-dimensional and depth-averaged large-eddy simulations of some shallow water flows. *Journal of Hydraulic Engineering*, 133(8):857–872, 2007.
- [15] Daniele Carati and W Cabot. Anisotropic eddy viscosity models. 1996.
- [16] Massimo Germano, Ugo Piomelli, Parviz Moin, and William H Cabot. A dynamic subgrid-scale eddy viscosity model. *Physics of Fluids A: Fluid Dynamics*, 3(7):1760–1765, 1991.
- [17] Federico Roman, Goran Stipcich, Vincenzo Armenio, Roberto Inghilesi, and Stefano Corsini. Large eddy simulation of mixing in coastal areas. *International Journal of Heat and Fluid Flow*, 31(3):327–341, 2010.
- [18] Peng Zheng, Ming Li, Joep van der Zanden, Judith Wolf, Xueen Chen, Caixia Wang, et al. A 3d unstructured grid nearshore hydrodynamic model based on the vortex force formalism. *Ocean Modelling*, 116:48–69, 2017.
- [19] Mohamed Fathy Mohamed Yossef. *Morphodynamics of rivers with groynes*. Delft University Press Delft, Netherlands, 2005.
- [20] Gerhard H Jirka. Large scale flow structures and mixing processes in shallow flows. *Journal of Hydraulic Research*, 39(6):567–573, 2001.
- [21] P Doron, L Bertuccioli, J Katz, and TR Osborn. Turbulence characteristics and dissipation estimates in the coastal ocean bottom boundary layer from piv data. *Journal of Physical Oceanography*, 31(8):2108–2134, 2001.

- [22] Hans Burchard, Peter D Craig, Johannes R Gemmrich, Hans van Haren, Pierre-Philippe Mathieu, HE Markus Meier, W Alex M Nimmo Smith, Hartmut Prandke, Tom P Rippeth, Eric D Skyllingstad, et al. Observational and numerical modeling methods for quantifying coastal ocean turbulence and mixing. *Progress in oceanography*, 76(4):399–442, 2008.
- [23] Michael S Longuet-Higgins and RW Stewart. Radiation stresses in water waves; a physical discussion, with applications. In *Deep Sea Research and Oceanographic Abstracts*, volume 11, pages 529–562. Elsevier, 1964.
- [24] Ib A Svendsen. Mass flux and undertow in a surf zone. *Coastal Engineering*, 8(4):347–365, 1984.
- [25] Leo C Van Rijn. Unified view of sediment transport by currents and waves. i: Initiation of motion, bed roughness, and bed-load transport. *Journal of hydraulic engineering*, 133(6):649–667, 2007.
- [26] Rolf Deigaard et al. *Mechanics of coastal sediment transport*, volume 3. World scientific publishing company, 1992.
- [27] Leo C van Rijn. Unified view of sediment transport by currents and waves. ii: Suspended transport. *Journal of Hydraulic Engineering*, 133(6):668–689, 2007.
- [28] Jørgen Fredsøe, Ken H Andersen, and B Mutlu Sumer. Wave plus current over a ripple-covered bed. *Coastal Engineering*, 38(4):177–221, 1999.
- [29] Dimokratis GE Grigoriadis, Athanassios A Dimas, and Elias Balaras. Large-eddy simulation of wave turbulent boundary layer over rippled bed. *Coastal engineering*, 60:174–189, 2012.
- [30] Joep Van Der Zanden, D Hurther, I Cáceres, T O’Donoghue, Jan S Ribberink, et al. Suspended sediment transport around a large-scale laboratory breaker bar. *Coastal engineering*, 125:51–69, 2017.
- [31] Peter Nielsen. Field measurements of time-averaged suspended sediment concentrations under waves. *Coastal Engineering*, 8(1):51–72, 1984.
- [32] Kazuo Nadaoka, Seizo Ueno, and Tatsuyuki Igarashi. Sediment suspension due to large scale eddies in the surf zone. In *Coastal Engineering 1988*, pages 1646–1660. 1989.
- [33] Troels Aagaard and Stine G Jensen. Sediment concentration and vertical mixing under breaking waves. *Marine Geology*, 336:146–159, 2013.

- [34] Daniel T Cox, Nobuhisa Kobayashi, and Akio Okayasu. Bottom shear stress in the surf zone. *Journal of Geophysical Research: Oceans*, 101(C6):14337–14348, 1996.
- [35] B Mutlu Sumer, H Anil Ari Guner, Nilas Mandrup Hansen, David R Fuhrman, and Jørgen Fredsøe. Laboratory observations of flow and sediment transport induced by plunging regular waves. *Journal of Geophysical Research: Oceans*, 118(11):6161–6182, 2013.
- [36] Joep van der Zanden. *Sand transport processes in the surf and swash zones*. University of Twente, 2016.
- [37] Leo C Van Rijn, Jan S Ribberink, Jebbe Van Der Werf, and Dirk JR Walstra. Coastal sediment dynamics: recent advances and future research needs. *Journal of hydraulic research*, 51(5):475–493, 2013.
- [38] NRRC Booij, Roeland C Ris, and Leo H Holthuijsen. A third-generation wave model for coastal regions: 1. model description and validation. *Journal of geophysical research: Oceans*, 104(C4):7649–7666, 1999.
- [39] Darrell Strauss, H Mirferendes, and Rodger Tomlinson. Comparison of two wave models for gold coast, australia. *Journal of Coastal Research*, pages 312–316, 2007.
- [40] Knut Klingbeil, Laurent Debreu, Florian Lemarié, and Hans Burchard. The numerics of hydrostatic structured-grid coastal ocean models: state of the art and future perspectives. 2017.
- [41] Norman A Phillips. A coordinate system having some special advantages for numerical forecasting. *Journal of Meteorology*, 14(2):184–185, 1957.
- [42] Alan F Blumberg and George L Mellor. *A numerical calculation of the circulation in the Gulf of Mexico*. Dynalysis of Princeton, 1981.
- [43] Changsheng Chen, Hedong Liu, and Robert C Beardsley. An unstructured grid, finite-volume, three-dimensional, primitive equations ocean model: application to coastal ocean and estuaries. *Journal of atmospheric and oceanic technology*, 20(1):159–186, 2003.
- [44] Pascal Lazure and Franck Dumas. An external–internal mode coupling for a 3d hydrodynamical model for applications at regional scale (mars). *Advances in water resources*, 31(2):233–250, 2008.
- [45] Alan F Blumberg and George L Mellor. A description of a three-dimensional coastal ocean circulation model. *Three-dimensional coastal ocean models*, 4:1–16, 1987.

- [46] Alexander F Shchepetkin and James C McWilliams. The regional oceanic modeling system (roms): a split-explicit, free-surface, topography-following-coordinate oceanic model. *Ocean modelling*, 9(4):347–404, 2005.
- [47] Hans Burchard and Ole Petersen. Models of turbulence in the marine environment—a comparative study of two-equation turbulence models. *Journal of Marine Systems*, 21(1-4):29–53, 1999.
- [48] Changsheng Chen, Robert C Beardsley, and Geoffrey Cowles. An unstructured grid, finite-volume coastal ocean model: Fvcom user manual. *SMAST/UMASSD*, pages 6–8, 2006.
- [49] John C Warner, Christopher R Sherwood, Richard P Signell, Courtney K Harris, and Hernan G Arango. Development of a three-dimensional, regional, coupled wave, current, and sediment-transport model. *Computers & Geosciences*, 34(10):1284–1306, 2008.
- [50] Tian-Jian Hsu and Philip L-F Liu. Toward modeling turbulent suspension of sand in the nearshore. *Journal of Geophysical Research: Oceans*, 109(C6), 2004.
- [51] Akio Okayasu, Keiichiro Fujii, and Masahiko Isobe. Effect of external turbulence on sediment pickup rate. *Coastal Engineering Proceedings*, 1(32):14, 2011.
- [52] Mantripathi Prabath Ravindra Jayaratne and Tomoya Shibayama. Suspended sediment concentration on beaches under three different mechanisms. *Coastal engineering journal*, 49(4):357–392, 2007.
- [53] Nobuhisa Kobayashi and Bradley D Johnson. Sand suspension, storage, advection, and settling in surf and swash zones. *Journal of Geophysical Research: Oceans*, 106(C5):9363–9376, 2001.
- [54] Paulo Alves da Silva, André Temperville, and Fernando Seabra Santos. Sand transport under combined current and wave conditions: A semi-unsteady, practical model. *Coastal Engineering*, 53(11):897–913, 2006.
- [55] Benoit Camenen and Magnus Larson. A total load formula for the nearshore. In *Coastal Sediments’ 07*, pages 56–67. 2007.
- [56] Jabbe J van der Werf, JS Doucette, Thomas O’Donoghue, and Jan S Ribberink. Detailed measurements of velocities and suspended sand concentrations over full-scale ripples in regular oscillatory flow. *Journal of Geophysical Research: Earth Surface*, 112(F2), 2007.

- [57] Leo C van Rijn. Unified view of sediment transport by currents and waves. iii: Graded beds. *Journal of Hydraulic Engineering*, 133(7):761–775, 2007.
- [58] Stephen B Pope and Stephen B Pope. *Turbulent flows*. Cambridge university press, 2000.
- [59] B Mutlu Sumer et al. *Hydrodynamics around cylindrical structures*, volume 26. World scientific, 2006.
- [60] CF Von Carmer. *Turbulent shallow wake flows: Momentum and mass transport due to large-scale coherent vortical structures*. PhD thesis, Ph. D. thesis, Univ. of Karlsruhe, Germany, 2005.
- [61] CFv Carmer, V Weitbrecht, and GH Jirka. On the genesis and fate of large coherent vortical structures in turbulent shallow wake flows. In *Proc. 3rd International Symposium on Environmental Hydraulics, Tempe, USA*, 2001.
- [62] J Jeong, FF Grinstein, and Fazle Hussain. Evolution of coherent structures in a numerically simulated plane wake. *Applied scientific research*, 53(3-4):227–236, 1994.
- [63] Min S Chong, Anthony E Perry, and Brian J Cantwell. A general classification of three-dimensional flow fields. *Physics of Fluids A: Fluid Dynamics*, 2(5):765–777, 1990.
- [64] A Tuck and J Soria. Separation control on a naca 0015 airfoil using a 2d micro znmf jet. *Aircraft Engineering and Aerospace Technology*, 80(2):175–180, 2008.
- [65] Andrey Nikolaevich Kolmogorov. The local structure of turbulence in incompressible viscous fluid for very large reynolds numbers. In *Dokl. Akad. Nauk SSSR*, volume 30, pages 299–303, 1941.
- [66] Anthony Galea. Large-eddy simulation for wind and tidally driven sea circulation in coastal semi-closed areas. 2014.
- [67] Wolfgang Rodi, George Constantinescu, and Thorsten Stoesser. *Large-eddy simulation in hydraulics*. Crc Press, 2013.
- [68] Jorge Bardina, J Ferziger, and W Reynolds. Improved subgrid-scale models for large-eddy simulation. In *13th Fluid and PlasmaDynamics Conference*, page 1357, 1980.
- [69] S Stolz and Nikolaus A Adams. An approximate deconvolution procedure for large-eddy simulation. *Physics of Fluids*, 11(7):1699–1701, 1999.

- [70] Jochen Fröhlich and Dominic Von Terzi. Hybrid les/rans methods for the simulation of turbulent flows. *Progress in Aerospace Sciences*, 44(5):349–377, 2008.
- [71] LA Morales Marin. *Numerical Modelling of Hydrodynamics and Sedimentation in Upland Lakes and Implications for Sediment Focusing*. PhD thesis, UCL (University College London), 2013.
- [72] Ranjan Ariathurai and Kandiah Arulanandan. Erosion rates of cohesive soils. *Journal of the hydraulics division*, 104(2):279–283, 1978.
- [73] Phillip Colella and Paul R Woodward. The piecewise parabolic method (ppm) for gas-dynamical simulations. *Journal of computational physics*, 54(1):174–201, 1984.
- [74] Xu-Dong Liu, Stanley Osher, and Tony Chan. Weighted essentially non-oscillatory schemes. *Journal of computational physics*, 115(1):200–212, 1994.
- [75] Eugen Meyer-Peter and R Müller. Formulas for bed-load transport. In *IAHSR 2nd meeting, Stockholm, appendix 2*. IAHR, 1948.
- [76] Richard L Soulsby and Jesper S Damgaard. Bedload sediment transport in coastal waters. *Coastal Engineering*, 52(8):673–689, 2005.
- [77] Richard Soulsby. *Dynamics of marine sands: a manual for practical applications*. Thomas Telford, 1997.
- [78] Ole Secher Madsen. Spectral wave-current bottom boundary layer flows. In *Coastal Engineering 1994*, pages 384–398. 1995.
- [79] Richard Styles and Scott M Glenn. Modeling bottom roughness in the presence of wave-generated ripples. *Journal of Geophysical Research: Oceans*, 107(C8):24–1, 2002.
- [80] Patricia L Wiberg and Courtney K Harris. Ripple geometry in wave-dominated environments. *Journal of Geophysical Research: Oceans*, 99(C1):775–789, 1994.
- [81] Hans-Jakob Kaltenbach. Cell aspect ratio dependence of anisotropy measures for resolved and subgrid scale stresses. *Journal of Computational Physics*, 136(2):399–410, 1997.
- [82] Alberto Scotti, Charles Meneveau, and Douglas K Lilly. Generalized smagorinsky model for anisotropic grids. *Physics of Fluids A: Fluid Dynamics*, 5(9):2306–2308, 1993.
- [83] S Zahrai, FH Bark, and RI Karlsson. On anisotropic subgrid modeling. *European journal of mechanics. B, Fluids*, 14(4):459–486, 1995.

- [84] Pierre Sagaut. *Large eddy simulation for incompressible flows: an introduction*. Springer Science & Business Media, 2006.
- [85] Robert A Clark, Joel H Ferziger, and William Craig Reynolds. Evaluation of subgrid-scale models using an accurately simulated turbulent flow. *Journal of fluid mechanics*, 91(1):1–16, 1979.
- [86] CD Argyropoulos and NC Markatos. Recent advances on the numerical modelling of turbulent flows. *Applied Mathematical Modelling*, 39(2):693–732, 2015.
- [87] Marcel Lesieur. *Turbulence in fluids: stochastic and numerical modelling*. Nijhoff Boston, MA, 1987.
- [88] Filippo Maria Denaro. What does finite volume-based implicit filtering really resolve in large-eddy simulations? *Journal of Computational Physics*, 230(10):3849–3883, 2011.
- [89] PA Madsen, M Rugbjerg, and IR Warren. Subgrid modelling in depth integrated flows. In *Coastal Engineering 1988*, pages 505–511. 1989.
- [90] Sanjiv Ramachandran, Amit Tandon, and Amala Mahadevan. Effect of subgrid-scale mixing on the evolution of forced submesoscale instabilities. *Ocean Modelling*, 66:45–63, 2013.
- [91] K Lilly. The representation of small-scale turbulence in numerical simulation experiments. 1966.
- [92] Elie Bou-Zeid, Charles Meneveau, and Marc Parlange. A scale-dependent lagrangian dynamic model for large eddy simulation of complex turbulent flows. *Physics of fluids*, 17(2):025105, 2005.
- [93] Tamay M Özgökmen, Traian Iliescu, and Paul F Fischer. Reynolds number dependence of mixing in a lock-exchange system from direct numerical and large eddy simulations. *Ocean Modelling*, 30(2-3):190–206, 2009.
- [94] Tamay M Özgökmen, Andrew C Poje, Paul F Fischer, and Angelique C Haza. Large eddy simulations of mixed layer instabilities and sampling strategies. *Ocean Modelling*, 39(3-4):311–331, 2011.
- [95] Andrés E Tejada-Martí, Chester E Grosch, Ann E Gargett, Jeff A Polton, Jerome A Smith, JA MacKinnon, et al. A hybrid spectral/finite-difference large-eddy simulator of turbulent processes in the upper ocean. *Ocean Modelling*, 30(2-3):115–142, 2009.

- [96] Vladimir Moiseevich Kamenkovich. *Fundamental of Ocean Dynamics*, volume 16. Elsevier, 2011.
- [97] Roxana C Wajswicz. A consistent formulation of the anisotropic stress tensor for use in models of the large-scale ocean circulation. *Journal of Computational Physics*, 105(2):333–338, 1993.
- [98] John Miles. On transversely isotropic eddy viscosity. *Journal of physical oceanography*, 24(5):1077–1079, 1994.
- [99] A Petronio, F Roman, C Nasello, and V Armenio. Large eddy simulation model for wind-driven sea circulation in coastal areas. *Nonlinear Processes in Geophysics*, 20(6):1095–1112, 2013.
- [100] J Fröhlich, W Rodi, Ph Kessler, S Parpais, JP Bertoglio, and D Laurence. Large eddy simulation of flow around circular cylinders on structured and unstructured grids. In *Numerical flow simulation I*, pages 319–338. Springer, 1998.
- [101] Anatol Roshko. On the development of turbulent wakes from vortex streets. 1954.
- [102] Yue Yin, Elizabeth Christie, Ming Li, Charles Moulinec, and David Emerson. 3d morphological impact modelling of offshore wind farms using les and hpc. *Coastal Engineering Proceedings*, 1(34):48, 2014.
- [103] Y Aghaee and H Hakimzadeh. Three dimensional numerical modeling of flow around bridge piers using les and rans. In *International conference on fluvial hydraulics, river flow*, pages 211–218, 2010.
- [104] Joongcheol Paik and Fotis Sotiropoulos. Coherent structure dynamics upstream of a long rectangular block at the side of a large aspect ratio channel. *Physics of fluids*, 17(11):115104, 2005.
- [105] Andrew McCoy, George Constantinescu, and Larry Weber. Exchange processes in a channel with two vertical emerged obstructions. *Flow, turbulence and combustion*, 77(1-4):97–126, 2006.
- [106] Masaya Kato, Yuhki Okumura, Yasunori Watanabe, and Hiroshi Saeki. Large-eddy simulation of local flows around the head of a breakwater. In *Ocean Wave Measurement and Analysis (2001)*, pages 1126–1135. 2002.
- [107] Mete Koken and George Constantinescu. An investigation of the dynamics of coherent structures in a turbulent channel flow with a vertical sidewall obstruction. *Physics of Fluids*, 21(8):085104, 2009.

- [108] Mete Koken and George Constantinescu. An investigation of the flow and scour mechanisms around isolated spur dikes in a shallow open channel: 1. conditions corresponding to the initiation of the erosion and deposition process. *Water Resources Research*, 44(8), 2008.
- [109] Mona M Mostafa, Hassan S Ahmed, Ashraf A Ahmed, Gamal A Abdel-Raheem, and Nashat A Ali. Experimental study of flow characteristics around floodplain single groyne. *Journal of Hydro-environment Research*, 22:1–13, 2019.
- [110] Akbar Safarzadeh, Seyed Ali Akbar Salehi Neyshabouri, and Amir Reza Zarrati. Experimental investigation on 3d turbulent flow around straight and t-shaped groynes in a flat bed channel. *Journal of Hydraulic Engineering*, 142(8):04016021, 2016.
- [111] Albert Molinas, Khaled Kheireldin, and Baosheng Wu. Shear stress around vertical wall abutments. *Journal of Hydraulic Engineering*, 124(8):822–830, 1998.
- [112] William J Devenport and Roger L Simpson. Time-depeident and time-averaged turbulence structure near the nose of a wing-body junction. *Journal of Fluid Mechanics*, 210:23–55, 1990.
- [113] WSJ Uijttewaal, D v Lehmann, and A van Mazijk. Exchange processes between a river and its groyne fields: Model experiments. *Journal of Hydraulic Engineering*, 127(11):928–936, 2001.
- [114] Wim S Uijttewaal. Effects of groyne layout on the flow in groyne fields: Laboratory experiments. *Journal of Hydraulic Engineering*, 131(9):782–791, 2005.
- [115] Joongu Kang, Hongkoo Yeo, and Changsung Kim. An experimental study on a characteristics of flow around groyne area by install conditions. *Engineering*, 4(10):636, 2012.
- [116] Andrew McCoy, George Constantinescu, and Larry Weber. A numerical investigation of coherent structures and mass exchange processes in channel flow with two lateral submerged groynes. *Water resources research*, 43(5), 2007.
- [117] Akbar Safarzadeh and Wernher Brevis. Assessment of 3d-rans models for the simulation of topographically forced shallow flows. *Journal of Hydrology and Hydromechanics*, 64(1):83–90, 2016.